UNIVERSITY OF CALIFORNIA
Los Angeles

Simulations of Super Alfvénic Laser Ablation Experiments in the Large Plasma Device

A dissertation submitted in partial satisfaction of the
requirements for the degree Doctor of Philosophy
in Physics

by

Stephen Eric Clark

2016

ABSTRACT OF THE DISSERTATION

Simulations of Super Alfvénic Laser Ablation Experiments
in the Large Plasma Device

by

Stephen Eric Clark

Doctor of Philosophy in Physics

University of California, Los Angeles, 2016

Professor Christoph Niemann, Chair

Hybrid plasma simulations, consisting of kinetic ions treated using standard Particle-In-Cell (PIC) techniques and an inertialess charge-neutralizing electron fluid, have been used to investigate the properties of collisionless shocks for a number of years. They agree well with sparse data obtained by flying through Earth's bow shock and have been used to model high energy explosions in the ionosphere. In this doctoral dissertation hybrid plasma simulation is used on much smaller scales to model collisionless shocks in a controlled laboratory setting. Initially a two-dimensional hybrid code from Los Alamos National Laboratory was used to find the best experimental parameters for shock formation, and interpret experimental data. It was demonstrated using the hybrid code that the experimental parameters needed to generate a shock in the laboratory are relaxed compared to previous work that was done[1]. It was also shown that stronger shocks can be generated when running into a density gradient. Laboratory experiments at the University of California at Los Angeles using the high energy kJ-class Nd:Glass 1053 nm Raptor laser, and later the low energy yet high repetition rate 25 J Nd:Glass 1053 nm

Peening laser have been performed in the Large Plasma Device (LAPD), which have provided some much needed data to benchmark the hybrid simulation method. The LAPD provides a repeatable, quiescent, ambient magnetized plasma to surround the exploding laser produced plasma that is ablated from a High Density Polyethylene (HDPE) target. The plasma density peaks in the machine at $n_i \sim \mathcal{O}(10^{13}\ \mathrm{cm}^{-3})$, which is sufficiently dense to strongly couple energy and momentum from a laser ablated carbon plasma ejected from the HDPE target into the magnetized ambient plasma. It has been demonstrated that a sub-critical shock is formed in the LAPD using the high energy Raptor laser[2], though the data from this experiment is scant. Hybrid simulation was used as an analysis tool for the shock experiments, but there remained the lingering question as to whether the assumptions made in the model sufficiently capture the relevant ion time scale physics and reproduce the magnetic field structure appropriately. A three-dimensional massively parallel hybrid code package was developed, called fHybrid3D, which was used to reexamine the 2013 data with more realistic laser ablation geometry. The data obtained in the 2015 Peening campaign proved to be useful, even though it did not generate a shock, in that it provided some volumetric data to compare to the 3D hybrid simulation. In addition to the larger magnetic field data sets, an emissive probe designed at UCLA[3] was fielded that could measure plasma potential. This is an important measurement, as previously only magnetic fields were measured on the ablation blow-off axis during the high energy laser experiments. This allows the laboratory experiment to directly validate the use of a simple isotropic electron pressure model close to the target. Though through scaling arguments the Larmor fields are strongest and provide the bulk of the ambient ion acceleration, correctly modeling the radial electric fields in the realm of sub-critical shocks is important for getting the coupling right as at lower Mach numbers. The data collected that is compared to simulation output that was converted to electrostatic potential ϕ suggests that the electron pressure model is sufficient for modeling perpendicular shocks in the laboratory.

The dissertation of Stephen Eric Clark is approved.

Walter Gekelman

George Morales

Chris Russell

Dan Winske

Christoph Niemann, Committee Chair

University of California, Los Angeles

2016

DEDICATION

I would like to dedicate this dissertation to my wife Elizabeth for sticking with me throughout the years and pushing me to strive for more. I would not have accomplished everything I have today without her love and support. We are a pair that will not be broken up even during the most stressful of times. Graduate school was a challenge for both of us and I am happy that we can move on to the next phase of our lives together.

I would also like to dedicate this dissertation to my step-mother Anne Schetter-Clark, who passed away young during my tenure at UCLA. She helped raise me from a young age and gave me guidance throughout the years which led to my ultimate admittance to graduate school at UCLA. Her fight against cancer over the last few years was difficult to bear for the entire family. She was a bright shining star that everybody in her life was attracted to, and we all aspire to be like how she lived her life, with compassion and motivation unparalleled.

Contents

List of Figures

List of Tables

ACKNOWLEDGEMENTS

I would like to acknowledge Dr. Christoph Niemann, as he has helped guide me through the gauntlet of graduate school. I would also like to acknowledge the rest of the students and members of the Phoenix Laser laboratory, which made the experiments possible.

I would also like to thank Dr. Dan Winske for taking an interest in my education and volunteering to be an outside member of my committee. I have learned a tremendous amount about plasma simulation and collisionless shocks from our conversations.

I would like to thank the rest of my committee members for spending the time reviewing this dissertation and providing feedback.

Finally, I would also thank the staff and students of the UCLA Basic Plasma Science Facility (BaPSF) for their support and help running diagnostics on the LAPD.

This work was supported by the Defense Threat Reduction Agency (DTRA) under contract number HDTRA1-12-1-0024, by the DOE Office of Science Early Career Research Program (DE-FOA-0000395), and by NSF award No. 1414591. This work used the Extreme Science and Engineering Discovery Environment (XSEDE), which is supported by National Science Foundation grant number ACI-1053575.

Curriculum Vitae

Academic History

2006	B.S. Physics with a specialization in computational physics
	University of California at San Diego
2011	M.S. Electrical Engineering (Applied Physics)
	University of California at San Diego
2012	M.S. Physics
	University of California at Los Angeles
2012 - 2016	Ph.D. Candidate in Physics
	University of California at Los Angeles

Selected Publications

Clark, S. E. *et al.*, "Enhanced collisionless shock formation in a magnetized plasma containing a density gradient", *Physical Review E* **90**, 041101(R) (2014).

Clark, S. E. *et al.*, "Hybrid simulation of shock formation for super-Alfvénic expansion of laser ablated debris through an ambient magnetized plasma", *Physics of Plasmas* **20**, 082129 (2013).

Clark, S. E. *et al.*, "Magnetic field measurements in low density plasmas using paramagnetic Faraday rotator glass", *Review of Scientific Instruments* **83**, 10D503 (2012).

Clark, S. E., M. Rosenberg, and K. Quest, "Simulation of two-stream instability in opposite polarity dusty plasma", *Journal of Plasma Physics* **78**(3), pp. 211-224 (2012).

Chapter 1

Introduction

Collisionless shocks are naturally occurring phenomena which are prevalent in space and astrophysical environments. They occur at the edges of supernova remnants[4], are formed in high altitude ionospheric explosions[5], are formed in front of comets[6], and are formed around Earth as the bow shock[7, 8]. Shocks have been generated in magnetic pinch experiments many years ago[9], though in recent years there has been renewed interest in studying astrophysical-like shocks generated in the laboratory. Currently several different methods are being employed to investigate the formation of shocks, including the collision of two plasma jets[10], and the interaction of two laser-produced plasmas[11]. In these cases the photographic evidence for the formation of a shock and the time scale for formation are suggestive but not conclusive. Novel studies are being carried out with experiments on super-Alfvénic laser-ablated debris expansions in a magnetized background plasma, using the Raptor laser in the Phoenix laser laboratory[12] with the Large Plasma Device (LAPD)[13, 14].

Laboratory experiments with rapidly exploding laser-produced plasmas can be designed to investigate the coupling of energy and momentum between a super-Alfvénic expanding debris cloud and a magnetized ambient plasma in the context of ionospheric and

astrophysical collisionless shocks. Scaled laboratory experiments can potentially provide new insight into shock physics that can only be limitedly studied in space, including the formation of a shock and the transport of debris ions across the shock ramp. For example, data recorded during high altitude nuclear tests in Earth's magnetosphere has revealed debris ions at altitudes many times higher than the blast-radius[5], an observation that is still not fully understood.

Laboratory shock-experiments are unique in that the ratio between the size of the exploding debris cloud and the debris ion Larmor radius is of order unity and thus quite similar to that in high-altitude tests but significantly smaller than in space and astrophysical explosions. Details of the coupling physics will thus critically affect shock formation, providing a test-bed where the physics of debris-ambient coupling can be studied in great detail.

Scaling the physics of astrophysical magnetized collisionless shocks to the laboratory has been a challenge, and previous laser experiments typically failed to provide sufficiently large and sufficiently magnetized, homogeneous, and accessible ambient plasmas, or to create fast enough and sufficiently large debris clouds[15, 16]. Some of the most relevant data was obtained in experiments that combined laser-produced explosions with preformed theta pinches[17]. Several authors have previously investigated the design space for scaled laboratory experiments, where a laser generated diamagnetic bubble is used as a piston to drive shock waves in an ambient plasma, using basic analytical scaling relations[18, 17, 19]. A new class of laser-experiments employs the Raptor kilojoule-class laser and the LArge Plasma Device (LAPD) at UCLA[13], uniquely combining an energetic super-Alfvénic debris cloud with a large (17m x 0.5 m), highly magnetized, current-free, quiescent, well-characterized, and highly-accessible ambient plasma[12]. Previously, experiments had been performed on the LAPD to diagnose the structure of an ablated laser-produced plasma into an ambient plasma using a 1 J laser, however in this case a shock was not formed[20].

Computer simulations of plasmas with hybrid codes, consisting of kinetic ions treated using standard Particle-In-Cell (PIC) techniques and an inertialess charge-neutralizing electron fluid, have been used extensively to investigate the coupling physics in the context of high-Mach number plasma interactions[21], astrophysical and high altitude nuclear explosions[22, 23, 24], and the structure of collisionless shocks in space[25, 26]. On a much smaller scale, they have also been used to model shock heating[27] and sub-Alfvénic expansions[28] in laboratory experiments, as well as shocks produced by small asteroids in the solar wind.[29]

Figure 1.1 shows images of physical situations that are relevant to the research being performed at UCLA and could potentially be elucidated via laboratory study of collisionless shocks.

The first purpose of this dissertation, discussed further in Chapter 3, is to extend this earlier work by using detailed two-dimensional (2D) hybrid simulations to guide scaled laboratory experiments and identify measurable quantities that could ultimately be used to infer details of the debris ambient coupling prior to the experiments (see Fig. 3.5). Early simulation work was used to predict experiments and determine the best parameters for shock formation in the LAPD. This simulation work demonstrates that the parameter space is relaxed compared to previous analysis using the hybrid model[1]. It is also demonstrated in Chapter 3 that shock formation is improved when a density gradient is encountered during the shock formation process.

Since the time that the initial analysis was done to help guide the experiments, a couple of datasets have been obtained from the LAPD. Simultaneously, an extension to the 2D hybrid code (fHybrid3D) was developed to be able to run full three-dimensional (3D) hybrid simulations using supercomputers housed at the San Diego Supercomputer Center (SDSC). The SDSC has two machines that were used, Gordon and Comet, that were funded by the NSF XSEDE program[30]. Details on the algorithm are available in Appendix A.

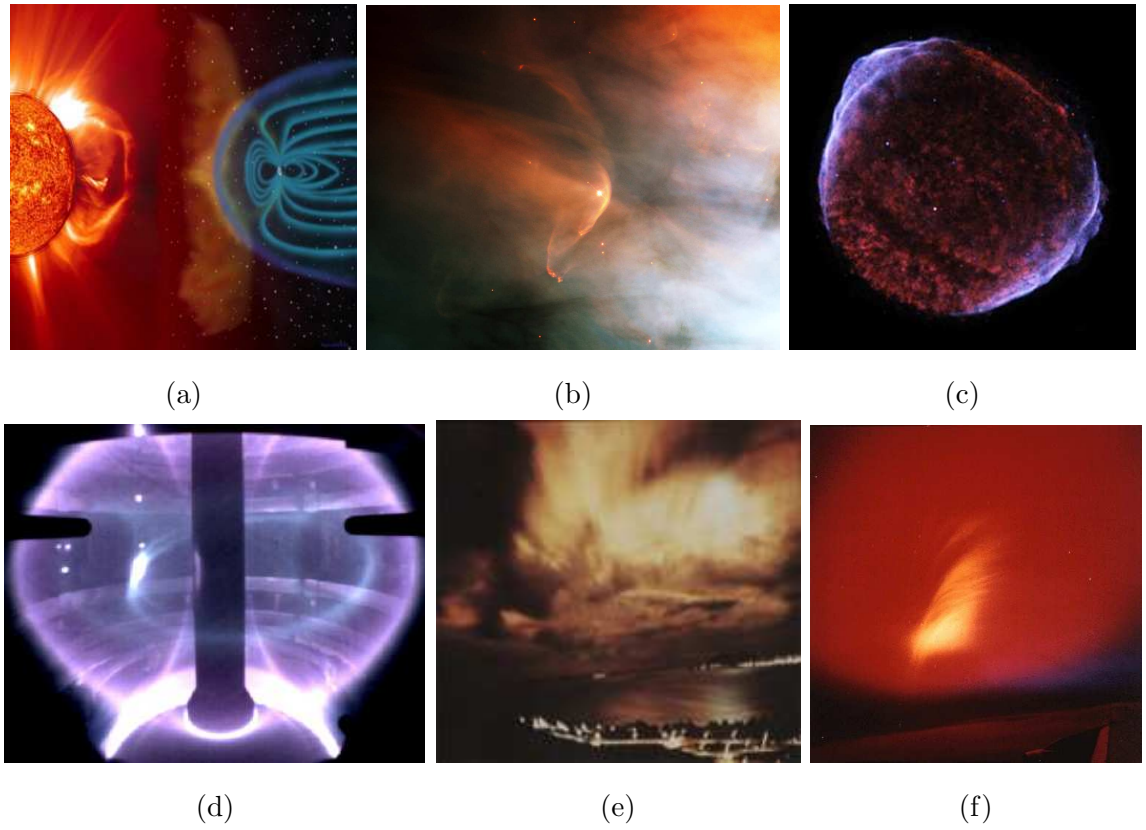

Figure 1.1: Shows (a) a cartoon of the Earth's magnetosphere superimposed over a coronal mass ejection from the Sun, (b) a bow shock around LL Orionis imaged by Hubble in 1995, (c) a supernova remnant SN 1006 imaged by Chandra in 2008, (d) an image of a fuel pellet experiment performed on MAST, (e) an image of the High Altitude Nuclear Explosion (HANE) Starfish Prime, which exploded over Johnson Island at 400 km in 1962, and (f) an aircraft based image of the Starfish Prime fireball stretching through Earth's magnetosphere.

Chapter 4 of this dissertation compares output from fHybrid3D to experimental magnetic flux probe[31] data obtained from the LAPD shock campaign that was run during the summer of 2013. This experimental campaign using the high-energy Raptor Laser, discussed in section 2.2, generated magnetized collisionless shocks in LAPD for the first time[2]. It is shown that 3D simulations using a new set of initial conditions (see Fig. 4.2) reproduce key features of the experiment and corroborate the previous analysis determining that a perpendicular shock wave formed within the high density core of the LAPD plasma. The 3D simulations are then compared to 2D simulations using similar initial conditions (see Fig. 4.8), and key differences such as the magnetic field compression and speed of the outgoing shock-wave are explored to demonstrate the differences in geometry.

Chapter 5 compares high repetition rate data form the LAPD experiment in the summer of 2015, where the Peening laser at lower energy was used to drive compressions in the ambient LAPD plasma. These compressions are not shocks, but since the repetition rate is higher there is much more data that can be compared to simulations. A new emissive probe[3] was also fielded in the experiment so that plasma potential can be measured. The combination of plasma potential and magnetic flux probe data in larger areas give a picture of the physical $\mathbf{E}$ and $\mathbf{B}$ fields that radiate out from the ablation. This data can be used to benchmark and validate the hybrid model, in which the electrons are treated as an inertialess, charge-neutralizing fluid.

The simulations presented in chapters 4 and 5 come from a massively parallel hybrid code newly developed at UCLA from an existing algorithm that was developed by Dan Winske at Los Alamos National Laboratory (LANL).[32] This tool can be used to help guide and validate future experiments, including those of parallel shocks that are to be performed in the upcoming years at the LAPD, using the Phoenix Laser facility. The simulations specifically model the laser-ablation experiments at the LAPD, but are equally relevant to potential shock experiments elsewhere, including future experiments at

megajoule-class laser facilities.[33] It will be shown that simulation data can be matched very closely to simulation data using initial conditions that have a reasonable amount of energy coupled into the debris plasma.

Chapter 2

Theory and Experimental Setup

2.1 Collisionless Shock Theory

Collisional shocks are a phenomenon that most people have heard while attending an air show. The sonic boom is a classic example of a collisional shock in which a flying vehicle is traveling faster than the speed of sound. The sound waves cannot outrun the disturbance to dissipate gas density that builds up in front of the obstacle. This leads to a sharp transitional period in the aircraft's frame of reference that has a width on the scale of the collisional mean-free-path of the gas particles that constitute the medium (air). Typical acoustic waves rely on inter-particle collisions to transfer energy and momentum from one particle to another. This can be thought of as the classical model of an ideal gas, where the particles can be imagined as ping pong balls flying around bouncing into one another. If there is a large amount of balls in one area, or a higher density, then the balls will tend to fly outward away from the high density region. The speed of these waves depends on the temperature of the gas, that is how fast they are flying relative to

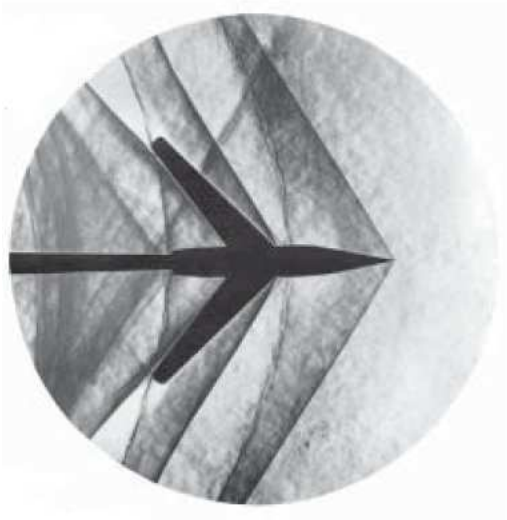

Figure 2.1: Image of a collisional shock experiment showing density build-up in from of an obstacle placed into a supersonic flow. Courtesy of NASA.

one another. Higher temperature will result in a larger sound speed, given by:

$$c_{ideal} = \sqrt{\frac{\gamma k_b T}{m}}\,, \tag{2.1}$$

where γ is the adiabatic index, k_b is the Boltzmann constant, T is the temperature of the gas, and m is the mass of a single constituent in the ideal gas. In an ideal gas, the particle mean free path for a test particle in a gas with density n can be written as:

$$\lambda_{mfp} = 1/n\sigma\,, \tag{2.2}$$

where σ is the collisional cross section of the gas constituents. This is the average distance a given particle can travel before colliding with another particle in the gas. This is the smallest length scale in a collisional system in which the only forces acting on a given particle come from the micro-physics of binary collisions.

Figure 2.1 shows an experimental image of gas density that build up in the supersonic flow that collides with an obstacle. The shock front comes off of the front of the obstacle at an angle, which determines the boundary between the shock upstream region and downstream region. The upstream region has no information regarding the obstacle

that radiates from it, so it cannot possibly organize into a system that flows around the object. Across the transition, there is a jump in density and gas temperature, and a drop in gas bulk flow to be sub-sonic. The shock transforms the energy that is concentrated mainly in a single direction, and redirects it into multiple directions, which effectively thermalizes the gas. The high density that is built up around the object reduces the collisional mean-free-path, which leads to a narrow region where collisions happen more regularly to redirect the ram pressure of the flowing gas around the object. This region will be on the order of the collisional mean-free-path.

2.1.1 Plasmas and Quasi-Perpendicular Collisionless Shocks

Collisionless shocks share some properties of collisional shocks, but have some astounding differences. The first thing to consider is a gas that is ionized, that is there exist electrons that have enough energy to not be bound to it nuclear counterpart. In the simplest case of hydrogen the ionized gas, or plasma, consists of free protons and electrons that exist in a quasi-neutral equilibrium. Since plasmas consist of charged particles, the dynamics of the system are then determined by the micro-physics of Coulomb interactions between particles. The Coulomb potential is a long range force that falls off like $1/r^2$, so the dynamics of the system can be quite complicated. Fortunately, under certain circumstances the plasma self organizes to counteract, or shield long range electric fields. This allows us to make assumptions regarding the plasma such that the particles are not very correlated. The strong Coulomb interactions will only occur over a distance less than a Debye length, which is given in CGS units by:

$$\lambda_D^2 = \frac{k_b T_e}{4\pi n_e e^2}\,, \tag{2.3}$$

where T_e is the electron temperature, n_e is the electron density, and e is the elementary charge. A few basic parameters that need to be satisfied to use traditional plasma theory include the system size being much larger than the Debye length ($\lambda_D \ll L$), and the

number of particles in a Debye sphere to be very large ($N_D = 4\pi n\lambda_D^3/3 \ggg 1$). This leads to collective plasma motion, or the continuum approximation. In the case where the dynamics of the system are dominated by collective plasma fields, and the binary coulomb collisions can be neglected, the plasma obeys the Vlasov equation:

$$\frac{\partial f_s}{\partial t} + \mathbf{v}\cdot\nabla f_s + \frac{Z_s e}{m_s}\big(\mathbf{E} + \frac{1}{c}(\mathbf{v}\times\mathbf{B})\big)\cdot\nabla_{\mathbf{v}} f_s = 0\,, \tag{2.4}$$

where $\mathbf{E}$ and $\mathbf{B}$ are the electric and magnetic field vectors respectively, s denotes the plasma species, $f_s(\mathbf{r},\mathbf{v},t)$ is the distribution function for species s, which depends on position $\mathbf{r}$, velocity $\mathbf{v}$, and time t. These coordinates determine a position in 6-D phase space at a time t. The Vlasov equation can be thought of as a conservation law of phase space density. The Vlasov equation is the starting point for kinetic plasma theory in the field of collisionless plasma physics. In addition to the Vlasov equation, one needs Maxwell's equations, given by:

$$\begin{aligned} \nabla\cdot\mathbf{E} &= 4\pi\rho \qquad & \nabla\cdot\mathbf{B} &= 0 \\ \nabla\times\mathbf{E} &= -\tfrac{1}{c}\tfrac{\partial\mathbf{B}}{\partial t} & \nabla\times\mathbf{B} &= \tfrac{4\pi}{c}\mathbf{J} + \tfrac{1}{c}\tfrac{\partial\mathbf{E}}{\partial t}\,, \end{aligned} \tag{2.5}$$

where ρ is the charge density, and $\mathbf{J}$ is the total current density vector. Coupling the Vlasov equation for each species with Maxwell's equations determines a system of equations that effectively describes the behavior of collisionless plasmas.

Using kinetic plasma theory, one can predict collective plasma behavior that satisfy the aforementioned plasma conditions. One such problem is that of collisionless shocks, where shocks form in plasmas that are similar to that of a hydrodynamic shock, in that there exists jumps in macroscopic quantities in the plasma, such as density, magnetic field strength, and temperatures from an upstream region to a downstream region. The major difference between a collisional shock and a collisionless shock is the interaction length. Since in a collisionless shock, information regarding particle positions is transmitted to other particles via electric and magnetic fields, inter-particle collisions are not necessary to form a shock-wave. In a collisionless plasma, the length scale over which the plasma state changes from upstream to downstream is that of an ion inertial length (c/ω_{pi}). In

the case of a collisionless plasma, the ion inertial length is much less than that of the collisional mean-free-path ($c/\omega_{pi} \ll \lambda_{mfp}$). The electric and magnetic fields mediate the particle interactions which thermalize the high Mach number ($\mathcal{M}$) flows, where the Mach number is the ratio of the upstream flow velocity to the group velocity of the wave mode that propagates in the shock frame.

In the case of a quasi-perpendicular, magnetized collisionless shock, which this dissertation will focus on, the shock is oriented such that there exists an ambient magnetic field oriented transverse to the flow direction of the upstream plasma. The waves that propagate across the magnetic field are called fast magnetosonic waves, which have the following dispersion relationship:

$$\frac{\omega^2}{k^2} = c^2 \frac{C_s^2 + v_A^2}{c^2 + v_A^2}\,, \tag{2.6}$$

where ω is the wave frequency, k is the wavenumber, c is the speed of light, $C_s^2 = \gamma Z_i k_b T_e/m_i$ is the sound speed in the plasma, and $v_A^2 = B^2/4\pi n_i m_i$ is the Alfvén speed. In the plasmas we typically deal with, we assume that $v_A \gg C_s$. In the case where $v_A \gg C_s$ and $v_A \ll c$, the group and phase velocities are approximated by $v_g = v_p \approx v_A$. This leads to the Mach number of interest being the Alfvénic Mach number denoted by $\mathcal{M}_A$.

2.1.2 Rankine-Hugoniot Jump Conditions for a Perpendicular Shock

If we consider a planar, perpendicular shock with an infinite transverse existence, then in the MHD limit the shock width becomes infinitesimal. The upstream and downstream regions are uniform and using conservation of mass, energy, and electromagnetic boundary conditions, one can determine the compression ratio of the density and magnetic field across the shock (i.e. the Rankine-Hugoniot (RH) jump conditions). In this

case, the compression ratio r can be expressed as Equation (5.13) in Burgess[34]:

$$(r-1)\{r^2\frac{2-\gamma}{\mathcal{M}_A^2}+r\big(\frac{\gamma}{\mathcal{M}_A^2}+\frac{2}{\mathcal{M}_{C_s}^2}+\gamma-1\big)-(\gamma+1)\}=0\,, \tag{2.7}$$

where $\mathcal{M}_{C_s}$ = is the sonic Mach number. In this dissertation, we will assume that the Alfvén speed is much larger than the ion sound speed ($v_A \gg C_s$). Using some typical LAPD experimental parameters of $T_e \sim 10$ eV, $\gamma = 5/3$, $B_0 = 200$ G, $n_i \sim 10^{13}$ cm^{-3}, in an ionized hydrogen ambient plasma one can calculate the sound speed and Alfvén speed to be $C_s \sim 4 \times 10^6$ cm/s, and $v_A \sim 14 \times 10^6$ cm/s. Given these parameters, the term including the sonic Mach number will be less that one tenth that of the term including the Alfvénic Mach number. As the ambient density increases, the ion sound speed becomes more important, but for the purposes of analysis in this dissertation, the compression ratios calculated will assume that the sound speed is much less than that of the Alfvén speed ($C_s \ll v_A$). Setting $\gamma = 5/3$ in Equation (2.7), and dropping the term with the sonic Mach number, the equation can be solved using the quadratic formula. Dropping the negative root, the solution can be expressed as:

$$r=-(\frac{5}{2}+\mathcal{M}_A^2)+\sqrt{(\frac{5}{2}+\mathcal{M}_A^2)^2+8\mathcal{M}_A^2}\,. \tag{2.8}$$

If we take the limit of this as the Mach number gets large we find that the maximum compression ratio that can be attained is:

$$\lim_{\mathcal{M}_A\to\infty} r(\mathcal{M}_A)=4\,. \tag{2.9}$$

Throughout this dissertation the Rankine-Hugoniot (RH) jump conditions will be used as a way of determining if a given simulation has generated a shock-wave. The density and magnetic fields in a shock simulation should change by roughly the RH jump conditions across the shock front.

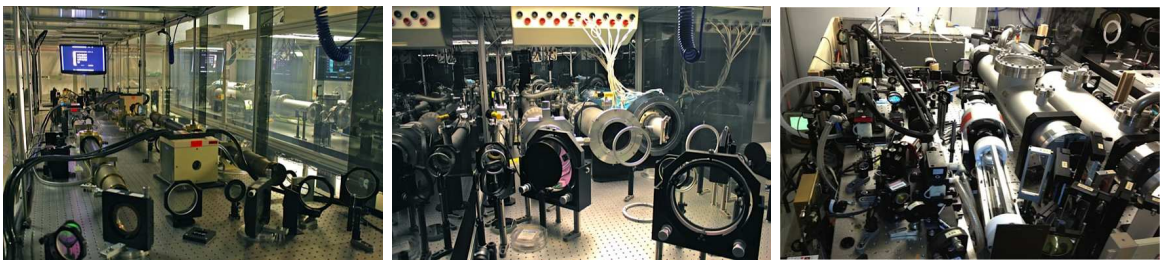

(a) (b) (c)

Figure 2.2: Shows (a) the 20 J 1064 nm Nd:Glass Phoenix Laser, (b) the kJ-class 1053 Nd:Glass Raptor laser, and (c) the 25 J 1053 nm high repetition rate Peening laser.

2.2 Experimental Facilities

There exist two conjoined laboratories that facilitate high energy density laser plasma experiments at UCLA, the Phoenix Laser Laboratory and the Large Plasma Device. The Phoenix Laser Laboratory consists of three lasers used for target ablation and diagnostics. The laboratory has multiple beam paths, and the ability to fire multiple lasers at prescribed time offsets. This allows an ablation beam to be fired, then a diagnostic beam can be fired for Thomson scattering measurements some time after the initial ablation beam is fired.

Figure 2.2 shows the lasers that currently operate in the Phoenix laser laboratory. Figure 2.2a shows the Phoenix laser, which is a 20 J 1064 nm Nd:Glass laser, that is frequency doubled into green for Thomson scattering. This laser as well as the Thomson scattering diagnostic will not be discussed further in this dissertation. Figure 2.2b shows the high energy kJ-class 1053 nm Nd:Glass laser used to ablate polyethylene targets in the 2013 shock campaign discussed in chapter 4. It has a 20 ns pulse width and delivers on target intensities on the order of 10^{13} W/cm^2. It can only be fired once every 45 minutes, so collected data from these experiments are scant. Figure 2.2c shows the high repetition rate 1053 nm Nd:Glass Peening laser, which has an on target energy around 25 J and can fire up to 6 Hz. The firing rate is matched to that of the LAPD such that the experiment

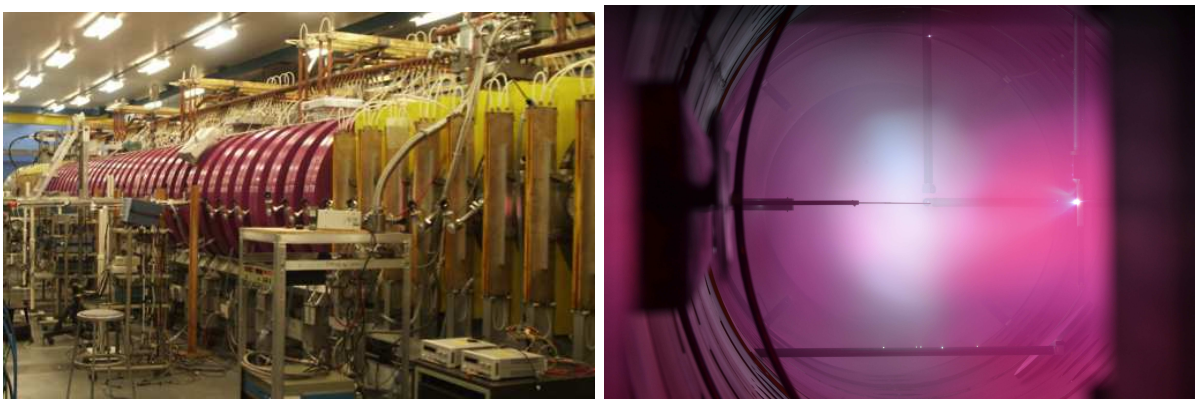

(a) (b)

Figure 2.3: Shows (a) the Large Plasma Device, and (b) a time integrated SLR image from one of the laser shots taken during and experimental campaign. The picture shows the target on the far right and inserted from the top and the laser-plasma plume exploding to the left. A diagnostic probe is inserted into the machine from the left.

can be repeated to take many more measurements in a given experimental campaign.

Figure 2.3a is a photograph of the Large Plasma Device (LAPD), which is an 18 m long solenoidal device that is 1 m in diameter. It contains a pair of plasma sources, one at each end of the machine, that create the plasma in the machine at 1 Hz that lasts for several ms. The laser experiments typically last on the order of 10 μs and are performed when the plasma is in near thermal equilibrium. The plasma state is highly reproducible, so that experiments can be run multiple times and probes can be inserted into the machine to measure various plasma properties at different points in space. The cathode at the south end of the machine is a Barium-Oxide (BaO) coated nickel cathode. The coating reduces the work function of the cathode so that electrons can be drawn from the cathode surface when a potential is set up via a biased mesh anode placed in front of the cathode. The cathode-anode pair generate a beam of electrons that travel down the machine along magnetic field lines and collide with neutral gas that is in the machine at low pressure. The high energy electrons collide with the neutral gas and impart energy into

the valence electrons, which then are excited and the gas ionizes. This process continues in an avalanche ionization process that produces the plasma in the machine. The electrons generated in the bulk plasma have a temperature $T_e \sim 1$ eV, the ions are around the same temperature, and the ion density is on the order of $n_e \sim 10^{12}$ cm^{-3}. The diameter of the plasma ranges from 40-80 cm depending on the operating magnetic field of the machine, which can operate from 200-1200 G. On the north end of the machine another cathode has recently been installed in 2013. This cathode consists of a low work function material called Lanthanum hexaboride (LaB_6), which has a much higher emissivity than the BaO coated cathode when heated to 3000 C. It has an anode like the other cathode and produces an electron beam that opposes that of the BaO cathode. The diameter of the plasma column generated by this cathode is 20-40 cm depending on the magnetic field configuration, and can create plasma densities of $n_i \sim \mathcal{O}(10^{13}$ cm$^{-3})$. Figure 2.3b shows a time-integrated SLR image of an experimental shot in the LAPD using the Raptor laser. The target is shown coming in from the top-right, being irradiated by the laser beam creating a laser ablation that interacts with the bulk plasma in the core of the machine. The large probes entering from the top-center and bottom-left are spectroscopic probes used to measure plasma photon emission. The probe entering the imaged from the left-center is a magnetic flux probe that is positioned in the debris blow-off axis to measure magnetic field changes that occur during the experiment.

2.3 Diamagnetic Cavity Size and Debris-Ambient Coupling Parameters

In the magnetized, quasi-perpendicular collisionless shock experiments performed in the LAPD, a high energy laser pulse is focused onto a HDPE target which is embedded in a quiescent, magnetized background plasma of either hydrogen or helium. The ablated carbon ions expand into the ambient plasma, perpendicular to the magnetic field, and

either acts as a piston and pushes the background ions through collisionless, collective electric and magnetic fields[4], which we will call coupling to the ambient plasma, or it streams through the ambient plasma without coupling and simply undergoes Larmor gyration in the background magnetic field.

The dynamics of an exploding plasma into vacuum have been investigated previously[35], and it has been shown that a diamagnetic bubble is formed with a size that can be calculated from an energy balance equation:

$$E_d = \frac{B_0^2}{8\pi}\frac{4\pi R_{b0}^3}{3}\,, \tag{2.10}$$

where E_d is the initial kinetic energy of the debris ions, B_0 is the background magnetic field, and the magnetic stopping radius R_{b0} is the size of the bubble.

If we now include background ion kinetic energy, assuming perfect coupling to the ambient plasma such that all of the ions within the diamagnetic bubble have been accelerated up to the debris drift velocity V_d, and that there are no other energy sinks (e.g. shear Alfvén waves or debris jetting), the energy balance equation can be modified to:

$$E_d = \frac{B_0^2}{8\pi}\frac{4\pi R_b^3}{3} + \frac{m_i n_i V_d^2}{2}\frac{4\pi R_b^3}{3}\,, \tag{2.11}$$

where R_b is the modified bubble size, and m_i and n_i are the background ion mass and density respectively. Eq. 2.11 can be manipulated to give the relationship:

$$\frac{R_b}{R_{b0}} = (1+\mathcal{M}_A^2)^{-1/3}\,, \tag{2.12}$$

where the Alfvénic Mach number is defined as $\mathcal{M}_A = V_d/v_A$, and $v_A = B_0/\sqrt{4\pi n_i m_i}$ is the Alfvén velocity. We now consider a new length R_m, the equal mass radius, defined in 3D as:

$$R_m = \left(\frac{3N_d m_d}{4\pi n_i m_i}\right)^{1/3}\,, \tag{2.13}$$

Eq. 2.13 is the radius of a sphere that encloses the amount of background ions which corresponds to the mass ablated from the target. Using $E_d = N_d m_d V_d^2/2$ to write Eq. 2.13

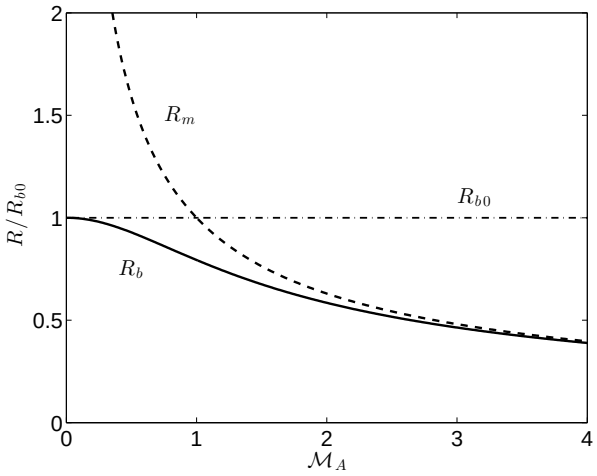

Figure 2.4: Bubble radius (R_b, solid), equal mass radius (R_m, dashed), and magnetic stopping radius (R_{b0}, dashed dotted) as a function of debris expansion Mach number ($\mathcal{M}_A$).

in terms of R_{b0} and $\mathcal{M}_A$, one can express the equal mass radius as:

$$\frac{R_m}{R_{b0}} = \mathcal{M}_A^{-2/3}\,. \tag{2.14}$$

Figure 2.4 shows a plot of the equal mass radius and the bubble radius over a range of Alfvénic Mach numbers. It shows that the bubble radius never exceeds the magnetic stopping radius, and approaches the equal mass radius asymptotically for large Mach number. It should be noted that the bubble size expression assumes perfect coupling. In reality, not all of the ambient ions will be expelled from the bubble, and may not be accelerated completely to the debris drift velocity. The actual bubble size will be somewhere in between the magnetic stopping radius and the bubble radius shown in Figure 2.4 depending on the degree of coupling. Figure 2.4 also assumes that the debris ions are sufficiently magnetized in vacuum to completely expel the magnetic field inside of the bubble, otherwise the cavity size could potentially be smaller than R_{b0}.[17]

2.4 The Magnetostatic Hybrid Model

Throughout this dissertation, the hybrid model will be examined and compared to experimental data to determine whether or not it captures the physics of diamagnetic cavities and shock formation. The hybrid model entails treating each ion species kinetically using the Vlasov equation, given by Equation (2.4). The first approximation made is that we are in the magnetostatic limit, where the displacement term in Ampere's law in neglected leaving the simplified equation that follows:

$$\nabla \times \mathbf{B} = \frac{4\pi}{c}\mathbf{J}\,. \tag{2.15}$$

The electrons are then treated as an inertialess charge-neutralizing fluid. The electron momentum equation in the inertia-less limit is as follows:

$$\cancelto{0}{m_e n_e \frac{D\bar{\mathbf{v}}_\mathbf{e}}{Dt}} = -en_e(\mathbf{E} + \frac{1}{c}\bar{\mathbf{v}}_\mathbf{e} \times \mathbf{B}) + en_e \overleftrightarrow{R} \cdot \mathbf{J} - \nabla \cdot \overleftrightarrow{P_e}\,. \tag{2.16}$$

Substituting in Equation (2.15) and solving for $\mathbf{E}$, assuming isotropic electron pressure, isotropic resistivity, and quasi-neutrality yields:

$$\mathbf{E} = -\frac{1}{c}\frac{\sum_\mathbf{i} \mathbf{J_i} \times \mathbf{B}}{e\sum_i Z_i n_i} + \frac{(\nabla \times \mathbf{B}) \times \mathbf{B}}{4\pi e \sum_i Z_i n_i} + \frac{c\eta}{4\pi}\nabla \times \mathbf{B} - \frac{\nabla p_e}{e\sum_i Z_i n_i}\,. \tag{2.17}$$

This equation for the electric field that emerges from the electron momentum equation does not depend on any electron parameters after manipulation. This determines an electric field that depends solely on the ion currents and the structure of the magnetic field at a given time. The time dependence of the magnetic field can be solved for using Faraday's law. Typically this set of equations is intractable to solve analytically, except in certain circumstances, so general problems are solved using the computational method described in Appendix A.

2.4.1 Collisions in the Large Plasma Device

The hybrid plasma model is one tool in the realm of collisionless plasma physics, so it must be shown that collisions do not play a large role in the formation of a shock-wave and that they can be neglected so that the hybrid model can be used.

To address this point, each type of collision will be examined, starting with the electron-electron (ee), electron-ion (ei), ion-electron (ie), and finally ion-ion (ii). We start by examining the collision rate and mean free path for electrons with a temperature $T_e \sim$ 8 eV. Calculating the slowing collision frequency numerically from the NRL formulary, we get $\nu_s^{ee} \sim 15\mu s^{-1}$, and $\lambda_{mfp}^{ee} \sim 8$ cm. The mean free path is on the order of the ion inertial length, and the collision time is sub microsecond. The experiments typically last a few microseconds, so the electrons will be collisional with themselves, and there will be some energy transport, or additional dissipation due to collisional diffusion. This effect should be minimal during shock formation, which is on a short time scale. However, it does allow us to use the fluid approximation for the electrons as the collisions will isotropize the electron temperature as well as make the velocity distribution Maxwellian.

Next we will address electron-ion collisions. Using the electron thermal velocity corresponding to $T_e \sim 8$ eV, and a background of protons at $T_i \sim 1$ eV, we calculate the slowing collision rate to be $\nu_s^{ei} \sim 41\mu s^{-1}$, and $\lambda_{mfp}^{ei} \sim 3$ cm. This would indicate that the electrons are colliding with the ions frequently on our time scales; however, if we look at the energy transfer rate $\nu_e^{ei} \sim .044\mu s^{-1}$, it becomes apparent that the collisions of electrons and ions do not transfer much energy to the ions over the duration of the experiment.

Now we will discuss the ion-ion collisions. If we first consider ion-ion collisions for protons using the thermal velocity associated with $T_i \sim 1$ eV, we calculate $\nu_s^{ii} \sim 5.7\mu s^{-1}$ and $\lambda_{mfp}^{ii} \sim 0.2$ cm. This means that the ambient plasma is indeed collisional on our time-scales; however, the interaction we are primarily interested in is between the upstream

and downstream ions. If we recalculate the collision rates using the measured velocity of the laser ablation for the test particle, $v_i \sim 4 \times 10^7$ cm/s, we get $\nu_s^{ii} \sim 9.7 \times 10^2 s^{-1}$ and $\lambda_{mfp}^{ii} \sim 4.1x10^4$ cm. Therefore, the interaction between the upstream and downstream protons is collisionless, and the shock cannot be formed via collisions.

Finally, if we examine the ion-electron collisions using the ablation streaming velocity, we obtain $\nu_s^{ie} \sim 4.2 \times 10^3 s^{-1}$ and $\lambda_{mfp}^{ii} \sim 9.5 \times 10^3$ cm. Therefore the ion-electron collisions are negligible.

Even though the ambient ions are collisional, a collisionless hybrid code is appropriate since the interaction between upstream and downstream ions is collisionless. The ambient ions are loaded with a Maxwellian velocity distribution, which the piston will encounter. The protons that are accelerated then become collisionless and interact through collisionless processes.

Another set of collisions to consider could potentially come from collisions with neutral gas particles. This could affect the plasma dynamics if there exists a sufficient number of neutral gas particles in the LAPD. The neutral particles could impart a drag force on moving ions, or could potentially undergo charge exchange in which fast ions pick up electrons from slow neutral particles. These could have an effect on the dynamics of the system, however require partial ionization of the LAPD plasma. The ionization fraction in the LAPD should be close to unity.

2.5 Detailed Derivation of 3D Bashurin Coupling Parameter

In this section, the procedure used to obtain the solution as well as the derivation of the energy coupling parameter, which describes the effectiveness of the energy transfer

from debris plasma to ambient plasma, will be shown with some in between steps for clarity. The notation will be updated to use modern typesetting as well to improve readability. The purpose of this is to introduce the use of the hybrid model in the context of solving for an approximate analytical solution. There are several approximations used in the derivation of this solution that will be discussed later in the text. Some of the approximations are the same as those used in the computational hybrid model, however one must keep in mind that many of the assumptions made to allow for a tractable analytical solution can be relaxed in computer simulation so that more physics may be unveiled.

Like most kinetic, or in this case partially kinetic plasma physics, the primary equation that comes to mind is the Vlasov equation, as shown in Equation (2.4). The Vlasov equation is used to describe the motion of the debris ions in phase space. Thusly, the debris ion density as a function of space and time ($n_d(\mathbf{x}, t)$) and average particle drift velocity ($\mathbf{v_d}(\mathbf{x}, t)$) can be calculated by taking moments of the Vlasov equation:

$$n_d(\mathbf{x}, t) = \int f_d(\mathbf{x}, \mathbf{v}, t) \mathrm{d}\mathbf{v}\,,\ \mathbf{J_d}(\mathbf{x}, t) = \int f_d(\mathbf{x}, \mathbf{v}, t) \mathbf{v} \mathrm{d}\mathbf{v}\,. \tag{2.18}$$

The ambient ions are assumed to be uniformly distributed in space and stationary ($T_i = 0$). The electrons are treated as an inertia-less, charge-neutralizing fluid in the ideal MHD approximation where resistivity and electron pressure are neglected in the electron momentum Equation (2.16), which can be written as:

$$\mathbf{E} + \frac{1}{c}\mathbf{v_e} \times \mathbf{B} = 0\,. \tag{2.19}$$

Since the fluid is charge neutralizing, this implies quasi-neutrality, which is written as:

$$Z_i n_i + Z_d n_d = n_e\,. \tag{2.20}$$

If we take Faraday's Law from Equation (2.5) and substitute in the potential vector for the electric field in the case where there is no electrostatic potential ($\mathbf{E} = -\frac{1}{c}\frac{\partial \mathbf{A}}{\partial t}$), and the magnetic field ($\mathbf{B} = \nabla \times \mathbf{A}$) we get:

$$\nabla \times \mathbf{E} = -\frac{1}{c}\frac{\partial}{\partial t}(\nabla \times \mathbf{A}) = \nabla \times (-\frac{1}{c}\frac{\partial \mathbf{A}}{\partial t})\,. \tag{2.21}$$

If we equate the terms within the curl operator, and substitute in the ideal MHD electron momentum Equation (2.19), we end up with:

$$\frac{\partial \mathbf{A}}{\partial t} = \mathbf{v_e} \times \mathbf{B}\,. \tag{2.22}$$

Now if we write down the equation for the net current:

$$\mathbf{J} = -en_e\mathbf{v_e} + eZ_dn_d\mathbf{v_d}\,, \tag{2.23}$$

and then substitute this into Equation (2.22), we then obtain the following equation for $\mathbf{A}$:

$$\frac{\partial \mathbf{A}}{\partial t} = \big[-\frac{c}{4\pi en_e}\nabla\times(\nabla\times\mathbf{A}) + \frac{1}{n_e}Z_dn_d\mathbf{v_d}\big]\times\big[\nabla\times\mathbf{A}\big]\,. \tag{2.24}$$

In the case where $\mathcal{M}_A \gg 1$, the magnetic curvature term becomes negligible and then we are in the net current zero limiting case ($\mathbf{J} \propto \nabla\times\mathbf{B} \sim 0$). Including quasineutrality from Equation (2.20), a simpler equation to be solved can be expressed as:

$$\frac{\partial \mathbf{A}}{\partial t} = \frac{Z_dn_d}{Z_dn_d + n_i}\mathbf{v_d}\times(\nabla\times\mathbf{A})\,. \tag{2.25}$$

Now that we have an equation to solve, we need to define the distribution function at $t = 0$ for the debris ion particles, which in the simplest unmagnetized case in the limit of $\mathcal{M}_A \gg 1$, where all of the debris ions originate from a point at the origin, as:

$$f_d(\mathbf{r},\mathbf{v},t=0) = N_d\delta^3(\mathbf{r})\psi(\mathbf{v})\,, \tag{2.26}$$

where $\psi(v)$ is the radially isotropic, normalized velocity distribution function for the debris cloud which will stay arbitrary for generality. Now we examine the simple characteristics for a radial expansion and find that $r_0 = r - v_rt$ and $v_{r0} = v_r$. Now we can write down the distribution function of the debris as a function of time in spherical coordinates as:

$$f_d(r,v_r,t) = \frac{N_d}{4\pi r^2}\delta(r-v_rt)\psi(\frac{r}{t}) = \frac{N_d}{4\pi r^2t}\delta(r/t-v_r)\psi(\frac{r}{t})\,. \tag{2.27}$$

Now we can take a couple of moments of this distribution function to obtain n_d, and $\mathbf{J_d}$, written as:

$$n_d = \frac{N_d}{t^3}\psi(\frac{r}{t}) \text{ and } \mathbf{J_d} = n_d\mathbf{v_d} = n_d\frac{r}{t}\hat{\mathbf{r}}\,, \tag{2.28}$$

so $\mathbf{v_d} = r/t\hat{\mathbf{r}}$. Manipulating Equation (2.25) yields:

$$\frac{\partial \mathbf{A}}{\partial t} = \frac{Z_d n_d}{Z_d n_d + n_i} v_{dr} \hat{\mathbf{r}} \times (\nabla \times \mathbf{A}) \,. \tag{2.29}$$

If we break this up into component form it becomes clear that $A_r = 0$ due to the radial expansion. This leaves two uncoupled differential equations of the form:

$$\frac{\partial A_\phi}{\partial t} = -\frac{Z_d n_d}{Z_d n_d + n_i} v_{dr} (\frac{1}{r}\frac{\partial}{\partial r}(r A_\phi)) \,, \tag{2.30}$$

and

$$\frac{\partial A_\theta}{\partial t} = -\frac{Z_d n_d}{Z_d n_d + n_i} v_{dr} (\frac{1}{r}\frac{\partial}{\partial r}(r A_\theta)) \,, \tag{2.31}$$

where the A_θ equation is exactly the same, but with $A_\phi \to A_\theta$. The initial conditions for the potential vector can be written as:

$$\mathbf{A}(\mathbf{r}, t = 0) = \frac{B_0 r}{2} \sin(\theta) \hat{\phi} \,, \tag{2.32}$$

where $\mathbf{B_0} = \nabla \times \mathbf{A_0} = B_0 \hat{\mathbf{z}}$. Since the initial value of $A_\theta(t = 0) = 0$, that means that it stays zero when integrating in time. This leaves only a single non-zero Equation (2.30), which when the θ dependence is removed by substituting $A_\phi(r, \theta, t) = A(r, t)\sin(\theta)$, yields the partial differential equation:

$$\frac{\partial A}{\partial t} + \frac{Z_d N_d \psi(r/t) \frac{r}{t^4}}{1 + Z_d N_d \psi(r/t) \frac{1}{t^3}} \frac{1}{r}\frac{\partial}{\partial r}(Ar) = 0 \,, \tag{2.33}$$

which is exactly Equation (2.6) in Bashurin[1]. The solution via Ansatz to this PDE is given in Bashurin Equation (2.7) and can be verified by substitution, which will not be shown here. The solution is:

$$A(r, t) = \begin{cases} 0 & 0 \le r \le r^* \\ \frac{B_0 R_*^2}{2r} \left[(\frac{r}{R_*})^3 + 4\pi \int_0^{r/t} \psi(v) v^2 \mathrm{d}v - 1 \right]^{2/3} & r^* \le r \end{cases} \,, \tag{2.34}$$

where $R_* = (3 N_d Z_d / 4\pi n_i Z_i)^{1/3}$, and r^* satisfies the following equation:

$$(\frac{r^*}{R_*})^3 + 4\pi \int_0^{r^*/t} \psi(v) v^2 \mathrm{d}v - 1 = 0 \,. \tag{2.35}$$

This solution can then be examined in the limit at $t \to \infty$ to determine to azimuthal component of the vector potential after the coupling has occurred. The vector potential in the limit as $t \to \infty$ is expressed as:

$$\lim_{t\to\infty} A(r,t) = \frac{B_0}{2r}(r^3 - R_*^3)^{2/3}\,. \tag{2.36}$$

We can easily see from Equation (2.36) that late in time, the velocity distribution becomes negligible. If we then use the conservation of angular momentum around the $\hat{\mathbf{z}}$-axis $\hat{\mathbf{z}} \cdot \mathbf{L} = \hat{\mathbf{z}} \cdot (\mathbf{r} \times \mathbf{p})$, where $\mathbf{p}$ is the canonical momentum for a charged particle in an electromagnetic field ($\mathbf{p} = m\mathbf{v} + \frac{Ze}{c}\mathbf{A}$), we can write a conservation law of the form:

$$r\sin(\theta)\Big(v_\phi + \frac{Z_i e}{m_i c}A_\phi\Big) = r_0\sin(\theta_0)\Big(v_{\phi 0} + \frac{Z_i e}{m_i c}A_{\phi 0}\Big)\,. \tag{2.37}$$

Assuming negligible displacement of a given ambient ion, (i.e. $r \sim r_0$, $\theta \sim \theta_0$), and that the ion is initially at rest ($v_{\phi 0} = 0$), we can solve for the azimuthal velocity of a particle after the expansion has completed as $t \to \infty$. This can be written as:

$$v_\phi = \frac{Z_i e}{m_i c}(A_{\phi 0} - A_\phi(t\to\infty)) = \begin{cases} \frac{\omega_{ci} r\sin(\theta)}{2} & 0 \le r \le R_* \\ \frac{\omega_{ci} r\sin(\theta)}{2}\big[1 - \big(1 - (\frac{R_*}{r})^3\big)^{2/3}\big] & r \ge R_* \end{cases}\,. \tag{2.38}$$

Now we want to calculate the total work done on the ambient ions by integrating over all ambient particles, in spherical coordinates it takes the form:

$$W_i = \frac{m_i n_i}{2}\int_0^\infty r^2 \mathrm{d}r \int_0^{2\pi} \mathrm{d}\phi \int_0^\pi \sin(\theta)\mathrm{d}\theta v_\phi^2\,. \tag{2.39}$$

Integrating over ϕ and θ after substituting in Equation (2.38) yields the following equation:

$$W_i = \frac{m_i n_i \pi \omega_{ci}^2}{3}\Big[\int_0^{R_*} r^4 \mathrm{d}r + \int_{R_*}^\infty r^4\big[1 - \big(\frac{R_*}{r}\big)^3\big]^2\Big]\,. \tag{2.40}$$

The first integral can easily be computed, the second however requires a change of variables ($x = r/R_*$) to create a dimensionless integral, which is written as:

$$W_i = \frac{m_i n_i \pi \omega_{ci}^2 R_*^5}{3}\big[\frac{1}{5} + \int_1^\infty [x^2 - (x^3-1)^{2/3}]^2 \mathrm{d}x\big]\,, \tag{2.41}$$

which can be written as:

$$W_i = \frac{m_i n_i \pi \omega_{ci}^2 R_*^5}{3} I\,, \tag{2.42}$$

where I is evaluated numerically to be $I \sim 0.707$. Now we need to compare the energy imparted to the ambient ions to the initial energy of the debris ions, which is written as:

$$W_{d0} = \frac{N_d m_d}{2} 4\pi \int_0^\infty v^4 \psi(v) \mathrm{d}v = \frac{N_d m_d}{2} < v^2 >= \frac{N_d m_d}{2} (\sigma^2 + < v >^2) \approx \frac{N_d m_d}{2} v_d^2 \,, \tag{2.43}$$

when the distribution thermal spread is much less than the expected value of v ($\sigma \ll < v >$), and the average debris velocity is defined as the expected value $< v >= v_d$. Now we can use this equation to determine the fraction of energy that is transferred to the ambient ions, which is written as:

$$\frac{W_i}{W_{d0}} = \frac{1}{2} \frac{R_*^2}{\rho_d \rho_i} I \,, \tag{2.44}$$

where $\rho_d = v_d/\omega_{cd}$ and $\rho_i = v_d/\omega_{ci}$ are the directed debris and ambient ion Larmor radii. If we define a parameter $\delta = R_*^2/(\rho_d \rho_i)$, and set Equation (2.44) to unity, we can solve for the condition in which a significant amount of energy is transferred to the ambient ions from the debris ions. This is written as:

$$\delta = \frac{2}{I} \approx 2.8 \,. \tag{2.45}$$

This parameter, which comes directly from the hybrid equations used in this sections determines a value for which coupling should occur. It will be shown later in this dissertation that this value can be relaxed and still have significant coupling to the ambient plasma.

2.6 Larmor Coupling and Shock Formation Criteria

The coupling of energy and momentum from the debris plasma to the ambient plasma has been shown previously[36, 1] to depend on a parameter that is proportional to R_m/ρ_d, where $\rho_d = V_d/\omega_{cd}$ is the directed Larmor radius of the debris ions and $\omega_{c\alpha} = Z_\alpha e B_0/m_\alpha c$ is the cyclotron frequency of a species α and Z_α is the charge state.

Golubev[36] derives a coupling parameter $\delta_1 \geq 1$, for a cylindrical expansion, which is equivalent to:

$$\delta_1 = \left(\frac{R_m}{\rho_d}\right)^2 \left(\frac{Z_i}{Z_d}\right)^2 \left(\frac{m_d}{m_i}\right) . \tag{2.46}$$

Bashurin[1] gives a different coupling parameter for a spherical expansion (see Equation (2.45)), which is equivalent to:

$$\delta_2 = \left(\frac{R_m}{\rho_d}\right)^2 \left(\frac{m_d}{m_i}\frac{Z_i}{Z_d}\right)^{1/3} . \tag{2.47}$$

The paper gives $\delta_2 \geq 2.8$ as the value required for coupling energy and momentum to the background ions. In chapter 3 we will compare the parameter R_m/ρ_d to 2D hybrid simulation results to see what value is required for coupling in the laboratory experiments. Hybrid simulations suggest that the condition for coupling is less stringent than the coupling condition derived in the Bashurin paper.

As discussed in the Golubev and Bashurin papers, the hybrid model where resistivity and electron pressure are neglected, in the high Mach number limit ($\mathcal{M}_A \gg 1$), the dominant term in Equation (2.17) will be the ion current term. Assuming the ambient plasma is current free, only the debris ions that are ablated will contribute to the electric field. If the ablation is symmetric and isotropic, ($\mathbf{J_d} = eZ_d n_d v_d \hat{\mathbf{r}}$), and the magnetic field is aligned with the $\hat{\mathbf{z}}$-axis, then the direction of the electric field will be $-\hat{\mathbf{r}} \times \hat{\mathbf{z}}$. If we confine our attention to the X-Y plane and use cylindrical coordinates, the electric field will be purely azimuthal ($\hat{\phi}$). Larmor coupling occurs when there is a significant azimuthal electric field that does work on the ambient ions. If the field persists long enough to accelerate the ambient ions up to the drift velocity in the azimuthal direction, they will then gyrate forward ahead of the magnetic pulse and drift radially. The conditions set forth by Equations (2.46) and (2.47) are the relevant parameters to determine whether or not coupling occurs. Namely it states that the debris mass must be sufficiently large, and the cavity size must be larger than the Larmor radius of the debris ions to couple energy to the ambient plasma.

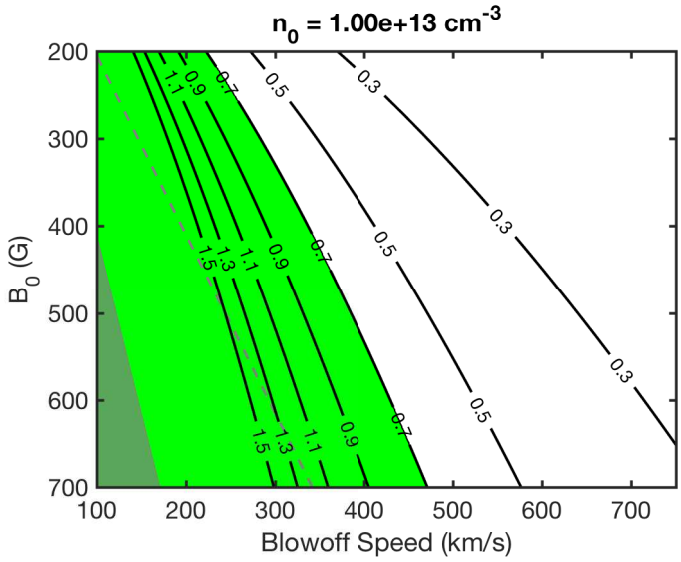

Figure 2.5: Estimated shock formation region in parameter space given in green region for debris kinetic energy of 200 J. The black contours are the calculated values of R_m/ρ_d given the parameters on the X and Y axis. The grayed out green region is sub-Alfvénic, the dashed grey line represents a $\mathcal{M}_A = 2$ expansion.

If the coupling is sufficient to transfer the energy from the debris ions to the ambient, then the debris will stop near the cavity edge and the accelerated ions will continue to stream across the magnetic field. The piston of the debris ions compresses and accelerates the ambient ions, which forms into a shock downstream region. If the drift velocity is super-Alfvénic, then a prediction for whether or not a shock is formed for a given set of parameters can be obtained.

Figure 2.5 is a composite plot that wraps up the coupling and shock formation criteria into a single figure that can be used to guide experiments. The axes are experimentally tunable parameters; the ambient magnetic field can be controlled by changing the current in the conducting copper rings around the LAPD, and the laser generated plasma blow-off velocity can be controlled by modifying the laser spot size on the target to change the irradiance and the laser debris blow-off velocity. The black contours in figure 2.5 represent calculated values of R_m/ρ_d in the parameter space. The light green

region gives the region in parameter space in which coupling occurs and a shock is formed. This corresponds to a value of $R_m/\rho_d > 0.7$, which has been shown in chapter 3 to be a sufficient condition for coupling and shock generation (see Fig. 3.5). The total debris kinetic energy used in the calculations to generate figure 2.5 is $E_d \sim 200$ J, the ambient density is assumed to be uniform with a density of $n_i \sim 10^{13}$ cm^{-3}, and the ambient plasma consists of H^{+1}, while the debris is C^{+4}. The figure shows that higher Mach number shocks can be obtained when operating at a lower magnetic field strength, but the laser plasma blow-off velocity must also be scaled back so as not to have the debris move too fast to decouple.

2.7 Relationship of Collisionless Coupling to collisionless Shock Physics

Much has been said in the previous sections about the experimental system, and how energy is imparted onto an ambient plasma given certain debris and ambient plasma conditions. In this chapter it has been discussed in the context of an early time model, derived using the assumption that the Mach number is very large ($\mathcal{M}_A \gg 1$), and the coupling is weak $R_m/\rho_d \ll 1$. To generate a collisionless shock using a super-Alfvénic piston, the ambient ions must move in the model system to be able to account for the physics of shock generation. This automatically invalidates the analytical model for time scales larger than the coupling time $\mathcal{O}(\omega_{ci}^{-1})$. This means that the coupling requirements may not be as stringent as suggested by the Bashurin model.

In figure 2.6, two different times are portrayed. Thus far we have discussed the physics of early time coupling, which is displayed on top. This region is important, and has been discussed extensively, since the experimental conditions directly affect the properties of the debris piston as well and the ambient plasma properties. The idea is

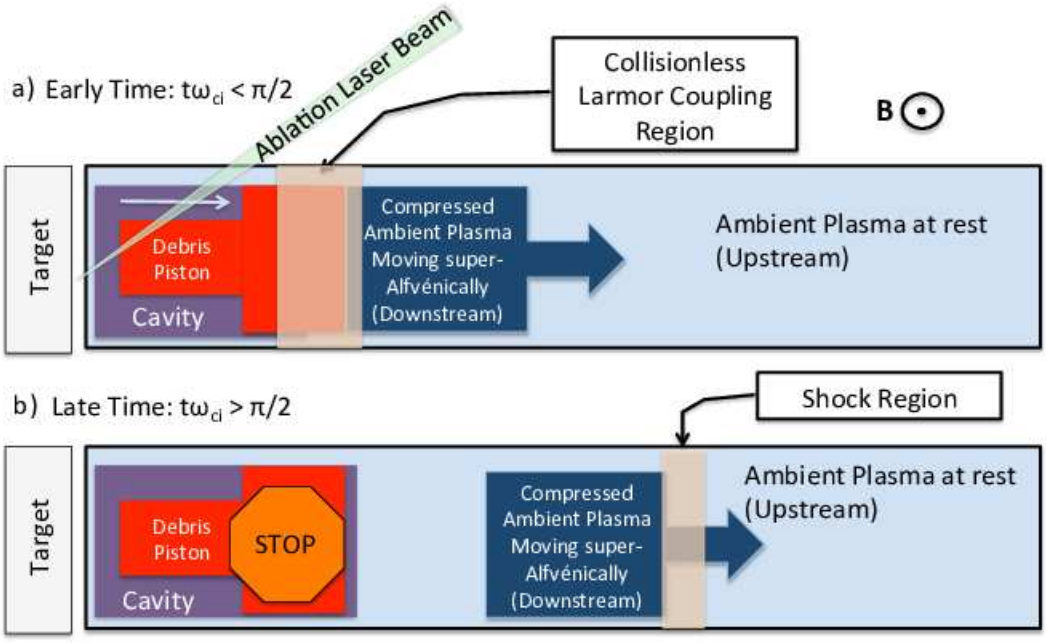

Figure 2.6: Cartoon of a shock being generated by a piston at early ($t\omega_{ci} < \pi/2$) and late ($t\omega_{ci} > \pi/2$) times .

that we control the plasmas such that strong coupling occurs between the debris plasma and the ambient plasma. Now this begs the question of what happens at later times, after coupling has occurred, and the ambient plasma is no longer uniform. Computer simulations are required at this point to model the system appropriately.

The lower panel in figure 2.6 illustrates a cartoon of the system at later time, after the debris plasma has expanded and stopped, giving its energy and momentum to a population of ambient ions. The downstream ambient population now consists of the accelerated ions that interacted with the debris plasma. In the lab frame the downstream region travels with some velocity relative to the stationary upstream ions. They stream into the ambient plasma at a super-Alfvénic velocity. Since these ambient ion motions are not taken into account when solving for the analytical solution, none of this can be discussed using the previously defined concepts. The following chapters will run simulations of debris expansions in various configurations and ambient plasma conditions to determine how the coupling parameter relates to shock formation. It will be shown that sufficient coupling that satisfies the aforementioned coupling parameters will generate a shock given enough space and time.

The two panels show some important regions that will be discussed much more in the following chapters. The upstream region of the shock consists of the ambient plasma provided by the LAPD. The downstream region consists on a region in which the magnetic field and ion densities are compressed by a factor predicted by the RH jump conditions. There are however kinetic ion effects that modify the shape of the shock ramp. In MHD, the shock ramp is a step function, however in kinetic ion hybrid simulations, the extent of the shock transition is spread over a region with a width on the order of the ion inertial length ($\Delta_{\text{shock}} \sim \mathcal{O}(c/\omega_{pi})$). This is due to impinging upstream ions that hit the cross-shock potential and turn around, or reflect from the shock. In super-critical perpendicular shocks, where $\mathcal{M}_A > 2.76$, there are so many reflected ions that a foot, or pedestal is created in front of the shock where there is a small bump up in ion density

and magnetic field compression. Super-critical shock dynamics will not be discussed much in this dissertation, as the shocks experimentally obtained are sub-critical. Future improvements to LAPD and the Phoenix laser facility will allow for higher Mach number shocks to be attained, but is left for future experimentation and analysis.

Shock physics consists of a balancing act of a few different competing phenomena that determine the structure of collisionless shock-waves. The RH jump conditions give an idea of what the ion density, magnetic field compressions, and temperature should be in the upstream and downstream regions, but there are several factors not included in the formation of the RH jump conditions using MHD theory. A shock is formed when when something moves faster than the wave speed can propagate away from it. In the case of a fast magnetosonic wave, the speed at which it propagates is very near the Alfvén velocity. These waves try to propagate outward, but cannot escape the obstruction, so they end up steepening into a shock wave. In competition with the wave steepening is wave dispersion, and dissipation. In a parallel shock, wave dispersion plays an important role in the shock dynamics, but in the perpendicular case, the wave is nearly dispersionless, i.e. waves do not move out in front of the shock front. The mechanism that keeps the shocks in check in the case of a parallel shock is dissipation. Energy is dissipated away from the shock as it steepens and reaches a steady state condition at some point. In super-critical shocks, ion reflection causing ion heating downstream is the dominant form of dissipation, but in the sub-critical regime, the ions and electrons are resistively heated via cross-field micro-instabilities[37]. The ion and electron heating occurs because there exists a tangential current driven by a combination of ∇n_e effects and $\mathbf{E} \times \mathbf{B}$ drifts associated with the radial components of the electric field at the leading edge of the shock. This current drives cross-field instabilities which saturate and heat the ion and electron population in the downstream region. The electron heating in the hybrid model can easily be incorporated with an appropriate electron pressure model, where we use an adiabatic temperature model with $\gamma \sim 5/3$. The ion heating due to micro-instabilities is ignored in the hybrid model, however a warmer electron population will increase the

cross shock potential, which will reflect some of the upstream ions that impinge upon it. These reflected ions then gyrate back into the downstream region and aids in generating a warmer downstream ion temperature. In chapter 5, the computer simulations will be compared to electrostatic measurements to verify that the fields generated by the electrons is consistent with observation in the laboratory.

Chapter 3

Two Dimensional Hybrid Simulations

The simulations presented in this chapter are computed using a 2D3V collisionless magnetostatic hybrid code in which there are two Cartesian spatial dimensions, but the fields and velocities are in three dimensions[22]. The magnetostatic approximation is a low frequency approximation which neglects the displacement current in Ampere's law. The code treats the ions kinetically using the particle-in-cell technique, while treating the electrons as a massless fluid. The electrons are modeled such that they do not have a uniform temperature, but heat adiabatically ($T_e(\vec{x}) = T_{e0}(n_e(\vec{x})/n_0)^{\gamma_e - 1}$, with $\gamma_e = 5/3$). The simulation model is valid for collective plasma behavior that occurs over multiple ion inertial lengths (c/ω_{pi}) over a number of ion gyroperiods ($2\pi\omega_{ci}^{-1}$), as is the case in astrophysical explosions[22]. The simulation can be spatially resolved down below the ion inertial length, but may not be accurate when approaching cell sizes on the order of the electron inertial length since the electrons are treated as massless. More information regarding the computational algorithm used can be found in Appendix A.

3.1 Analysis of Coupling Parameter Using 2D Hybrid Simulations

The coupling parameters that were discussed in Chapter 2 are examined in this section using the 2D hybrid code. This examination is done to verify the coupling parameter and to determine the best experimental conditions to generate a collisionless shock.

3.1.1 Some Relevant Simulation Parameters

Since the simulations are in two spatial dimensions, it is useful to recast a few parameters in two dimensions. Since the simulation is in dimensionless units, the parameters examined will be dimensionless as well. In two dimensions, the equal mass radius can be expressed in terms of the ion inertial length c/ω_{pi}, where $\omega_{pi}^2 = 4\pi Z_i^2 e^2 n_i/m_i$, as:

$$\frac{R_m}{c/\omega_{pi}} = \left(\frac{2Z_i e}{m_i c}\right)\sqrt{N_d m_d}\,. \tag{3.1}$$

The directed debris ion gyroradius can be expressed as:

$$\frac{\rho_d}{c/\omega_{pi}} = \mathcal{M}_A \left(\frac{Z_i}{Z_d}\right)\left(\frac{m_d}{m_i}\right)\,. \tag{3.2}$$

Dividing Eq. 3.1 by Eq. 3.2 yields:

$$\frac{R_m}{\rho_d} = \mathcal{M}_A^{-1}\left(\frac{2Z_d e}{m_d c}\right)\sqrt{N_d m_d}\,. \tag{3.3}$$

Note that when expressed in this manner, the magnetic field does not enter explicitly. In order to maximize Eq. 3.3 we want to maximize the ablated mass and the charge to mass ratio of the debris, while keeping $\mathcal{M}_A > 1$.

3.1.2 Simulation of a Magnetosonic Shock in the LAPD

This section discusses a high resolution simulation, based on LAPD experimental parameters, of a laser produced diamagnetic bubble that drives a shock wave. The ambient plasma consists of hydrogen with a density $n_i \sim 10^{13}$ cm^{-3}, and the debris plasma consists of C^{+4}. The calculated equal mass radius is $R_m \sim 5.3\ c/\omega_{pi} \sim 40$ cm, which effectively sets the number of debris ions N_d. There are just under 6 million macro-particles for each species, which corresponds to 100 particles per cell for the ambient ions. The simulation domain consists of 240×240 interior cells that span 32 c/ω_{pi} in both dimensions. This gives a cell size of 0.13 c/ω_{pi} in x and y. The debris ions are initialized in the center of the simulation domain as a Gaussian distribution that spans over a few cells. These simulations neglect the laser-target physics as well as the target geometry, which has a non-symmetric one-sided expansion. This is to be able to connect to previous analytical theory as well as give a simplified geometry to distill the basics of coupling and shock generation physics. The debris ions are initialized to expand cylindrically from the center of the simulation domain with a blow-off speed of 275 km/s or $\mathcal{M}_A \sim 2$. In addition to the radial drift velocity, the debris ions also have a random thermal velocity that corresponds to a temperature $T_d \sim 1$ eV. A density floor of 5% of n_0 is imposed in the simulation to handle the bubble region so that the Alfvén speed does not get too large when the number of macro-particles decreases in the center of the simulation domain. The ambient ions are initialized randomly in the simulation domain with a temperature $T_i \sim 1$ eV. The electrons are treated as a charge neutralizing fluid with a temperature $T_{e0} \sim 5$ eV. The initial background magnetic field is $B_0 \sim 200$ G, which is oriented in the $\hat{z}$ direction, or out of the page when looking at the following figures.

The streak plots in Figure 3.1 show the evolution of the simulation over time versus position along the $\hat{x}$ direction. The magnetic field profile in Figure 3.1a shows a diamagnetic bubble that is roughly the size of the equal mass radius R_m. It also shows a double compression feature that is present after the shock wave separates from the piston

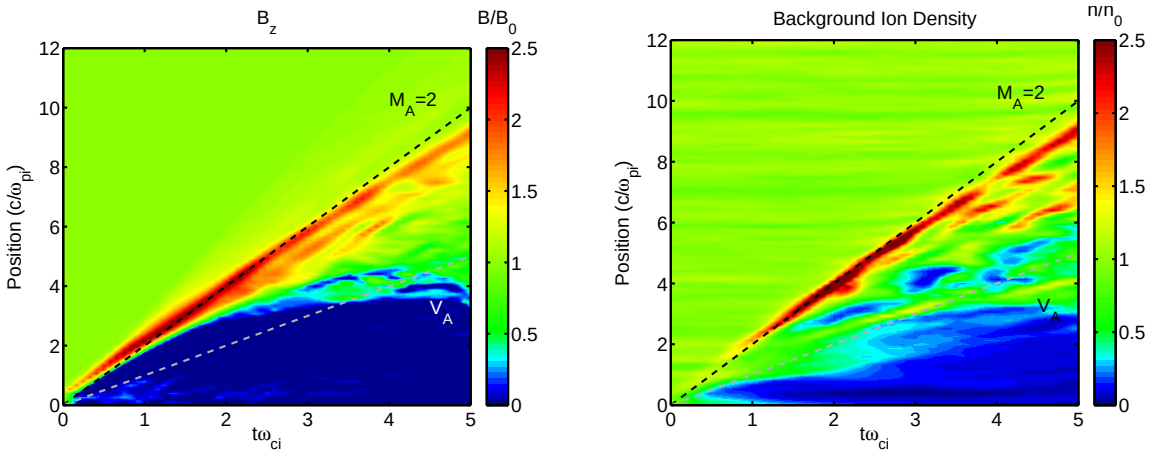

Figure 3.1: Magnetic field strength in $\hat{z}$ direction B_z (a), background plasma density n_i (b), and debris plasma density n_d (c) on the line $y = 0$, for $x > 0$ for the duration of the simulation. The dashed black line represents the slope of a $\mathcal{M}_A \sim 2$ expansion, and the white dashed line is $\mathcal{M}_A \sim 1$.

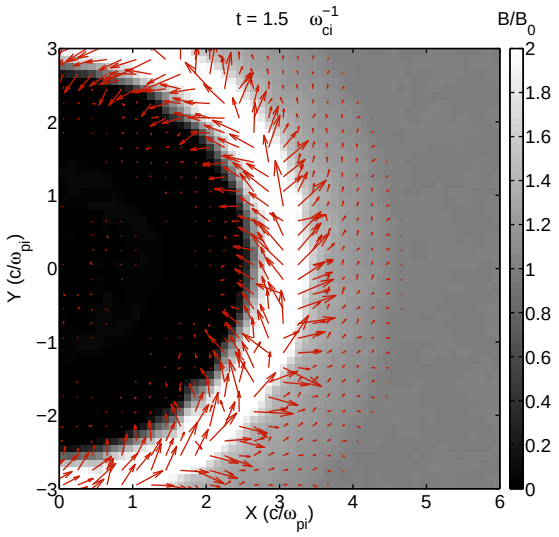

Figure 3.2: A composite figure of the background magnetic field (grayscale) along with relative electric field strength and direction (red arrows) at $t\omega_{ci} \sim 1.5$.

and propagates out. In this simulation the initial blow-off speed is $\mathcal{M}_A \sim 2$, which is the initial bubble formation velocity. At time $t\omega_{ci} \sim 1$, the magnetic pulse slows as the debris slows, which can be seen more clearly in Figure 3.1c. From $t\omega_{ci} \sim 1$ to ~ 3, the magnetic pulse speeds up, and after $t\omega_{ci} > 3$, it propagates outward at roughly $\mathcal{M}_A \sim 2$ as it separates from the diamagnetic bubble.

Figure 3.1b shows that coupling occurs since the background ions are depleted from the central region of the bubble. The background density compression for $t\omega_{ci} < 1$ is moving outward at a bit less than $\mathcal{M}_A \sim 2$, lagging the initial magnetic pulse. After time $t\omega_{ci} > 1$ the background ion density increases and, comparing Figures 3.1b and 3.1c, the magnetic pulse is now carried by the background ions as opposed to the debris ions. During the time that the pulse speeds up ($t\omega_{ci} \sim 1$ to ~ 3), it also steepens into a $\mathcal{M}_A \sim 2$ shock that propagates away from the magnetic cavity[38]. The density and magnetic field compressions of this shock are consistent with the Rankine-Hugoniot jump conditions.[39] Figure 3.1c shows the debris ions slowing down, mostly concentrated in a shell, until a time $t\omega_{ci} \sim 3$ (corresponding to $t\omega_{cd} \sim 1$), when the debris ions begin to diffuse.

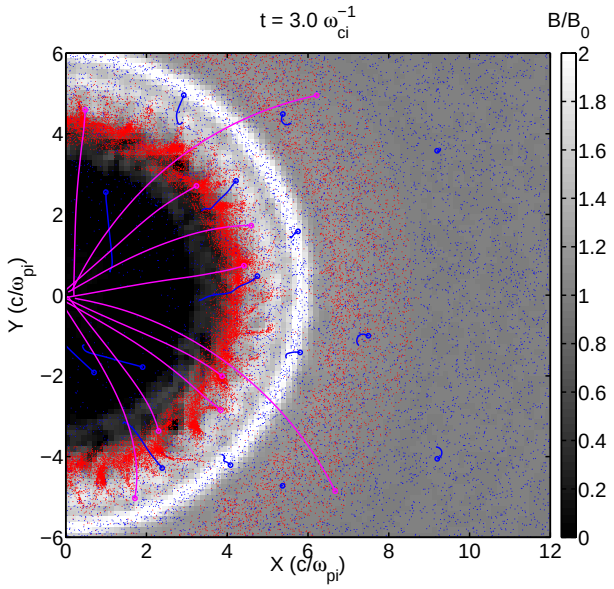

Figure 3.3: A composite figure of the background magnetic field along with a sampling of background (blue) and debris (red) ions overlaid at time $t\omega_{ci} \sim 3$. The lines represent a time history of selected background (blue) and ion (magenta) particles from the beginning of the simulation.

Figure 3.2 shows a 2D spatial plot of the magnetic field compression with the relative electric field strength at time $t\omega_{ci} \sim 1.5$. This is at a time when the magnetic field and background density are compressing and steepening, but the magnetosonic pulse has not separated from the debris piston. It can be seen that the electric field is pointed azimuthally around the bubble as opposed to being pointed radially outward. In the case of low Mach number expansions, the dominant electric field that couples energy and momentum to the background is radial[14]. In higher Mach number expansions, such as this simulation, the dominant coupling mechanism is Larmor coupling[40]. Previous simulations[38, 24] have shown that as the outward streaming debris ions begin to be deflected by the magnetic field, an azimuthal electric field (E_θ) is generated. This azimuthal electric field and the magnetic field in the $\hat{z}$ direction cause a drift of the background ions radially outward.

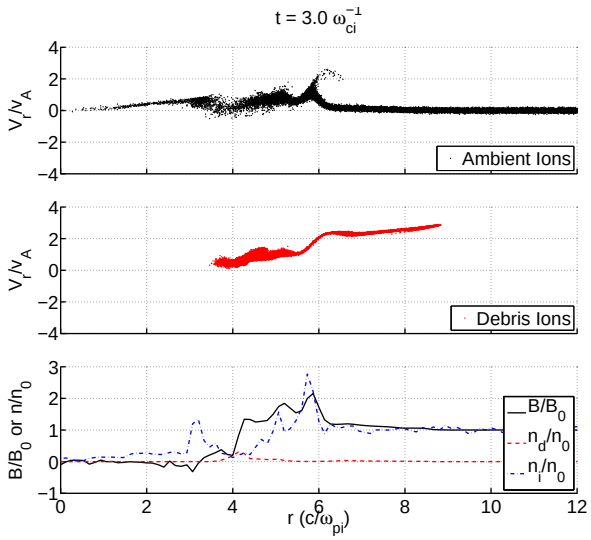

Figure 3.4: Phase space plot at time $t\omega_{ci} \sim 3$ of radial position and radially directed velocity components along with the corresponding magnetic field strength, background ion density, and debris ion density on the line $y = 0$, for $x > 0$.

The composite image in Figure 3.3 shows the magnetic field, a sampling of background and debris ions, and time history trajectories of a handful of particles at a time just after the magnetic pulse separates from the bubble. The bulk of the debris ions stop at the bubble edge, but there are a number of fast ions that are out in front of the compression. The electrons set up a strong radial electric field at the edge of the debris plasma early in the simulation due to large density and temperature gradients which accelerate a small percentage of debris ions up to high velocity. The fast debris ions exhibit Larmor gyration in the background magnetic field, but the particles that constitute the bulk of the debris mass move out radially and then stop at the bubble edge. The blue lines show a few sample background particles which have attained a radial velocity. Some background ions that are inside of the bubble, but were not accelerated all the way up to the magnetic pulse speed, free stream inside of the diamagnetic cavity. The background ions within the pulse are gyrating in the magnetic field, but are also moving outward, due to $E_\theta \times B_z$.

Figure 3.4 is a phase space plot of the radius versus radial velocity component of both the background and debris ions. The top panel clearly shows a population of reflected background ions at the foot of the magnetic pulse. Reflected ions are a well known dissipation mechanism for quasi-perpendicular shocks[25, 41] and spread out the shock front to a thickness c/ω_{pi}, as seen in the bottom panel.

Figure 3.4 also shows the acceleration of background ions in the downstream region that move with the shock front in the laboratory frame. Most of the debris ions in Figure 3.4 are bunched up at the bubble edge, but there are some fast debris ions which escape and move into the upstream region.

Figures 3.1 and 3.4 show that this simulation, which is representative of attainable parameters in the LAPD, will form a shock. The ion inertial length (c/ω_{pi}) is 7.2 cm and the bubble radius is around 5 c/ω_{pi}, which corresponds to a bubble radius of roughly 36 cm. This size bubble will fit well in the LAPD, with some room for a shock to propagate outward across the magnetic field.

3.1.3 Design Space for Laboratory Shock Experiments

Two interesting parameter sweeps were run using the hybrid code. The first sweep consists of a series of runs which keep the laser energy ($E_d \sim N_d m_d V_d^2/2$) on-target constant while varying the blow-off speed to reduce the Mach number across a number of different background densities. This is effectively like changing the laser spot size on the target. (Note: the dynamics of the laser target interaction are neglected in the calculation) A larger spot will illuminate a larger area of the target with less intense light causing more particles to be ablated at a lower velocity.[42, 43] In the simulations, only Carbon V (C^{+4}) is being ablated from the target. The assumption is that the dominant charge state will be C^{+4} for each of the runs[44]. In reality, lower ionization states may become the dominant charge state as laser radiation intensity drops. This set of runs is in

a background plasma of hydrogen with a temperature $T_i \sim 1$ eV, an electron temperature $T_e \sim 5$ eV, and a background magnetic field $B_0 \sim 200$ G. The background consists of ionized hydrogen, where the density n_i is varied between 10^{12} cm^{-3} to 4×10^{13} cm^{-3}, and the debris blow-off velocity varies from 500 km/s to 100 km/s while keeping the initial kinetic energy of the debris constant. The configuration of the simulation domain is the same as the detailed simulation, but there are 120 interior cells in each dimension and the number of macro-particles for each species is set to 25 particles per cell.

The equal mass radius was set to $R_m \sim 2.9\, c/\omega_{pi}$ for the simulations with a blow-off speed of 500 km/s. This was determined using Eq. 2.13 and setting the initial kinetic energy to 250 J. This is a conservative estimate as the explosions in the simulation are cylindrical, whereas in the experiment the energy in the debris will be directed in a cone moving away from the laser interaction region. The conical geometry leads to larger debris densities and a longer interaction region. The cylindrical geometry was chosen here to simplify the comparison to the analytical coupling parameter.

Figure 3.5a shows the results of the first scan where total energy in the simulation domain is held constant for each run. As the velocity drops, the amount of ablated mass is increased such that the energy ($E \sim N_d m_d V_d^2/2$) remains constant. As density increases, the scaled equal mass radius remains constant, since in 2D the density drops out of the scaled value. (see Eq. 3.1) The green region in Figure 3.5a indicates simulations in which the magnetic field compression meets or exceeds the Rankine-Hugoniot jump conditions. This metric is used to determine if a shock is formed in a particular simulation in parameter space. This figure shows that shocks begin to form when $R_m/\rho_d \geq 0.7$. Using the condition in Eq. 2.46 with the simulation parameters, $\delta_1 \geq 1$ implies a similar, but slightly more constrained condition, $R_m/\rho_d \geq 1.1$. One of the important features to note is that the isolines of the values for R_m/ρ_d cross over the Mach contours as the density of the background plasma is increased. Thus, increased background densities lead to higher Mach number shocks that are attainable in laboratory experiments. Though, as

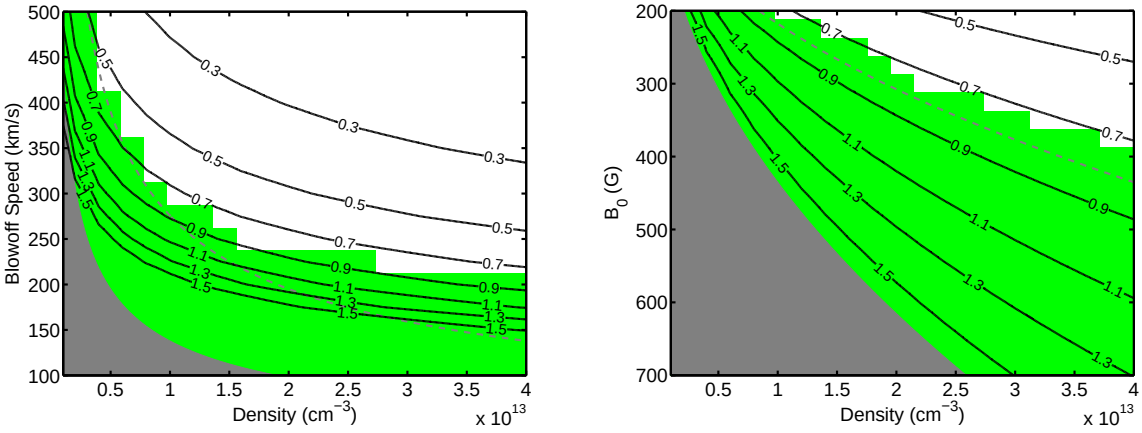

(a) (b)

Figure 3.5: Parameter space for (a) blow-off speed vs density with a background field of 200 G and (b) magnetic field vs. density with a blow-off speed of 300 km/s, both with a constant initial debris ion kinetic energy. The grey region marks the parameter space which is sub-Alfvénic, and the grey dashed line denotes the $\mathcal{M}_A \sim 2$ line. The green region indicates simulations which had magnetic field compression which met or exceeded the Rankine-Hugoniot jump conditions. The black contours show computed isolines of R_m/ρ_d.

	C^{+5}	C^{+4}	C^{+3}	C^{+2}
$\frac{R_m}{c/\omega_{pi}}$	1.8	5.0	2.7	1.8
$\frac{R_m}{\rho_d}$	0.3	0.8	0.4	0.2
$\mathcal{M}_A$	2.4	2	1.6	1.3
% E_{tot}	7%	85%	7%	1%

Table 3.1: Parameters for simulation with multiple charge states.

the background density increases, the collisional mean free path decreases and the Alfvén velocity approaches the sound speed. This brings the system into the collisional regime, which violates our assumptions for shock formation. This figure shows that for a C^{+4} plasma expanding into a hydrogen background plasma with density $n_i \sim 4 \times 10^{13}$ cm^{-3}, $\mathcal{M}_A \sim 3$ shocks should be attainable in the LAPD.

Figure 3.5b is similar to Figure 3.5a, except the background magnetic field is varied instead of the blow-off velocity to change the Mach number of the expansion. The figure shows a similar trend as the first scan except that the isolines of R_m/ρ_d do not cross the lines of constant Mach number. To attain a higher Mach number shock while increasing background density, it is more effective to increase the laser spot size and ablated mass coming from the target as much as possible without reducing the charge state of the blow-off. If one cannot increase the ablated mass further without compromising the charge state, it is then necessary to increase the background magnetic field to reduce the Mach number and enter the coupling regime. In experiments with $n_i \sim 10^{13}$ cm^{-3} and $B_0 \sim 200$ G, it should be possible to shock the background plasma with a debris blow-off Mach number of $\mathcal{M}_A \sim 2$. This corresponds to a debris blow-off velocity of ~ 250 km/s, which should be experimentally attainable on the LAPD.

3.1.4 Effect of Multiple Charge States

This section contains simulation results from a run where different charge states were ejected from the target at different velocities.[45] Table 3.1 shows the parameters that differ for each debris species, the calculated coupling parameter R_m/ρ_d, as well as the Mach number of the expansion. The background plasma is hydrogen with a density of $n_i \sim 10^{13}$ cm^{-3}. The background magnetic field is $B_0 \sim 200G$, the ion temperatures are $T_i = T_d \sim 1$ eV, and the electron temperature is $T_{e0} \sim 5$ eV. The equal mass radius for each species is calculated by taking the single species equal mass radius (R_{m0}) from the previous section and multiplying it by the energy percentage up to the one third power, i.e. $R_m = R_{m0}(\%E_{tot}/100)^{1/3}$. This follows from Eq. 2.11, where $R_b \propto (E_d)^{1/3}$. The dominant charge state, grid size, domain length, and number of macro-particles per species was chosen to match that of the detailed simulation in the previous section for direct comparison. The energy distribution of the debris species was chosen such that only C^{+4} would be in the coupling regime. The point of this simulation is to verify that under the assumption of a dominant charge species, the other species do not interact much during the shock formation. The question of having two debris species that couple and move at different velocities is not addressed here.

Figure 3.6 is included for direct comparison to Figure 3.1a. They exhibit all of the same features. The diamagnetic bubble radius is very near the equal mass radius, the magnetic field and background ion compressions satisfy the Rankine-Hugoniot jump conditions for a Mach 2 expansion, and the pulse separates from the bubble and propagates away just as it did in the previous simulation.

Figure 3.7 illustrates how the faster debris species with a higher charge state do not interact with the background plasma and simply undergo Larmor gyration out in front of the shock wave. The dominant charge state, which is C^{+4} (red/magenta) behaves nearly the same as the previous simulation. The slower charge species free stream in the

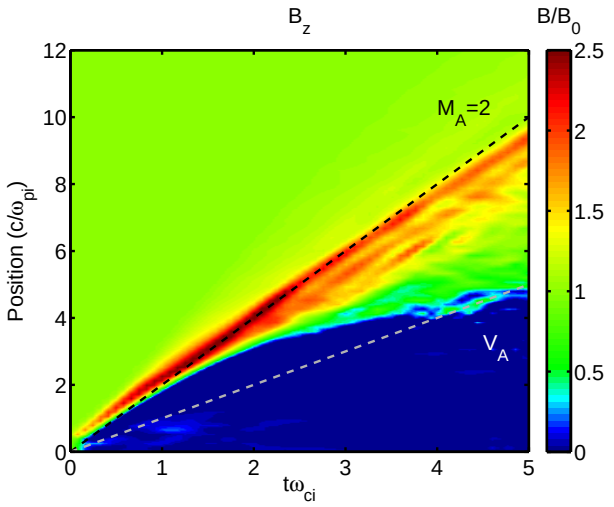

Figure 3.6: Streak plot of the magnetic field B_z on the line $y = 0$, for $x > 0$ for a simulation containing multiple charge states. The dashed black line represents the slope of a $\mathcal{M}_A \sim 2$ expansion, and the white dashed line is $\mathcal{M}_A \sim 1$.

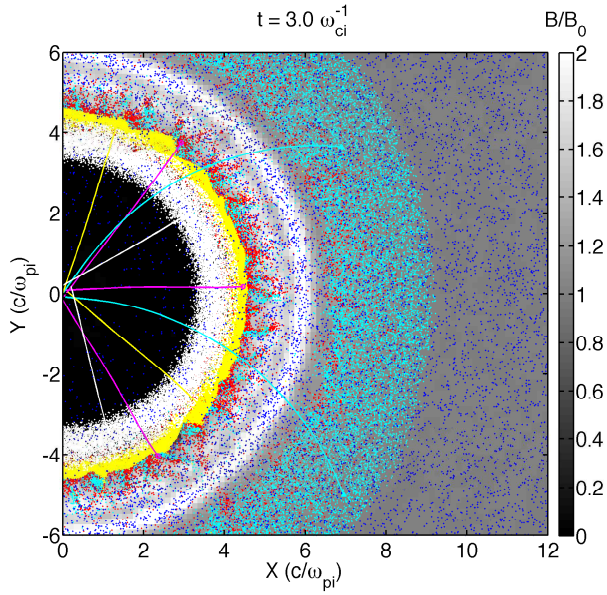

Figure 3.7: A composite figure of the background magnetic field (grayscale) along with a sampling of background (blue) and debris ions of different charge states ($Z = 4$:red, $Z = 5$:cyan ,$Z = 3$:yellow, $Z = 2$:white) overlaid at time $t\omega_{ci} \sim 3$. The lines represent a time history of selected background (blue) and ion ($Z = 4$:magenta, $Z = 5$:cyan, $Z = 3$:yellow, $Z = 2$:white) particles from the beginning of the simulation.

diamagnetic cavity and do not play a role in the bubble/shock formation.

The phase space (not included) shows reflected ions in the background plasma, so the shock is still formed even with other species involved in the simulation. Unless multiple energetic species exist which are thought to contribute to the shock formation, the other species need not be simulated to obtain reasonable results.

3.2 Effect of a Density Gradient on Shock Formation

This section of the dissertation extends previous computational studies to investigate the effects of a density gradient on the coupling of energy from the debris plasma to the ambient plasma. Hybrid simulations are performed in which the debris cloud is treated as a cylindrical expansion passing over a step function density jump. The simulation results are compared to a simple fluid model, initially conceived by Conrad Longmire but rigorously derived by Wright[46], which provides insight into the dependence of the electric and magnetic fields on the ambient ion density. Finally, magnetic flux probe measurements[31] will be compared to a simulation that more closely resembles experimental conditions, in which the debris plasma is modeled as a conical ejection which interacts with a high density core of plasma embedded in a lower density plasma.

Two simulations are presented to compare the difference between a cylindrical super-Alfvénic expansion through a uniform background and one with a lower density region near the initial debris cloud. Both simulations have an ambient plasma consisting of H^{+1} with a density $n_i = 10^{13}$ cm^{-3} everywhere, though the nonuniform case has a lower density near the initial debris ions of $n_i = \frac{1}{3} \times 10^{13}$ cm^{-3}, with a radius of 2 c/ω_{pi}. The debris consists of C^{+4} with initial kinetic energy of 50 J, and an expansion velocity of $\mathcal{M}_A \sim 2$. The simulation consisted of 240 $\times$ 240 cells with 100 particles per cell in each species and a grid size of 0.1 c/ω_{pi}. The ambient ion temperature is initialized to

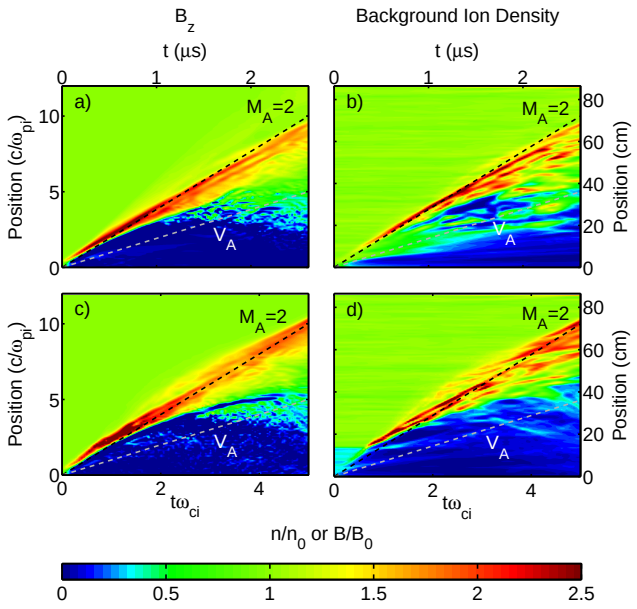

Figure 3.8: Space-time contour plots for two comparative hybrid simulations. The first row shows (a) B_z and (b) ambient ion density for the simulation case with uniform initial background density. Panels (c) and (d) show the same plots, but for the case with nonuniform ambient ion density. Each panel shows spatial profiles along a line through the domain for $x > 0$ and $y = 0$, as a function of time.

$T_i = 1$ eV and the electron temperature to $T_{e0} = 8$ eV. The initial background magnetic field is $B_z = 200$ G, which is perpendicular to the expansion. For the uniform density case, we find that $R_m \sim 5.3\ c/\omega_{pi}$, $\rho_d \sim 6\ c/\omega_{pi}$, and the ratio of the two is $R_m/\rho_d \sim 0.9$, where it has been shown that if the coupling parameter is greater than or equal to 0.7 a shock is formed[47]. These parameters are representative of attainable experimental plasma conditions.

Figure 3.8 displays space-time contour plots of the $\hat{z}$ component of the magnetic field and the ambient ion density. Figures 3.8a and 3.8b are typical of low Mach number shock simulations with a uniform background[47]. Figure 3.8a shows B_z for the uniform simulation, which indicates a diamagnetic bubble is formed[40], and a compressional elec-

tromagnetic pulse separates and propagates away from the edge of the bubble. Fig. 3.8b displays the ambient ion density being swept out partially in the diamagnetic bubble region. The magnetic field and ambient ion density show compressions on the order of two associated with the wave, which satisfies the Rankine-Hugoniot (RH) jump conditions for a $\mathcal{M}_A \sim 2$ shock[37]. The ion phase space (not shown) indicates that a small percentage of ambient ions are being reflected at the shock front. The combination of the compression satisfying RH jump conditions and the presence of dissipation indicates that the wave can be classified as a shock wave.

The lower panels in Fig. 3.8 show simulation data from the nonuniform simulation. The results look similar, but there are several noticeable differences. Fig. 3.8c shows that the shock that is launched is slightly faster than in Fig. 3.8a. The diamagnetic bubble also extends further spatially. Fig. 3.8d shows the density compression moving out faster than in the homogeneous case (Fig. 3.8b), the density is more fully swept out, and the compression is slightly higher.

The results presented in Fig. 3.8 imply that the coupling of energy and momentum to the ambient ions is stronger in the nonuniform case, resulting in stronger shock generation. This can be understood from the parameter R_m/ρ_d, which has been shown to correlate to the coupling of energy and momentum from debris ions to ambient ions[47]. From simple geometrical considerations, the nonuniform equal mass radius in two dimensions (2D) is $R_{mn}^2 = R_m^2 \times (1 + (1 - \alpha_n)(R_n/R_m)^2)$, where R_n is the radius of the density jump, and α_n is a dimensionless parameter that represents the density fraction in the core ($n_{in} = \alpha_n n_i$). In our case $\alpha_n = 1/3$, which gives a simplified expression: $R_{mn}^2 = R_m^2 \times (1 + 2/3(R_n/R_m)^2)$. So the nonuniform equal mass radius is larger than its uniform counterpart ($R_{mn} > R_m$), which leads to a larger coupling parameter in the nonuniform case ($R_{mn}/\rho_d > R_m/\rho_d$). The nonuniform equal mass radius (R_{mn}) is larger than the uniform case due to the lower density core. This implies stronger coupling for the nonuniform case.

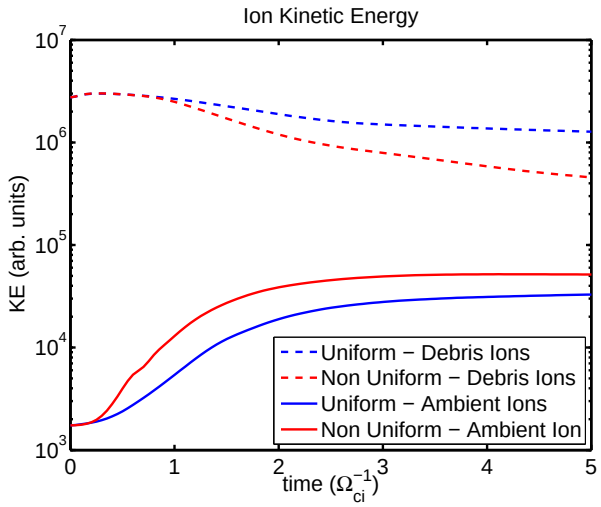

Figure 3.9: Kinetic energy of ambient ions (solid) and debris ions (dashed) for the uniform (blue/outer) versus the nonuniform (red/inner) simulation calculated from a sampling of particle data, which shows improved energy coupling to the ambient ions in the nonuniform case.

Fig. 3.9 clearly shows that the coupling of energy and momentum to the ambient plasma is increased in the nonuniform simulation. If we examine the solid lines, which represent the total kinetic energy of the ambient ions in the simulation, we see that ambient ions in the nonuniform simulation start to gain more energy relative to the uniform case around $t\omega_{ci} \sim 0.5$, which is when the bulk of the debris plasma expansion is propagating within the core region. In the non-uniform case, where the ambient plasma has less density than that of the uniform case within the interaction region, the ambient ions are accelerated to much higher velocity (see Fig. 3.11c). If we examine the dashed lines in figure 3.9 we can infer that the debris ions do not lose much energy early in the expansion. The debris ions in the nonuniform case start to lose a significant amount energy relative to the uniform case around $t\omega_{ci} \sim 1$, when the pulse overruns the density jump. This indicates that the energy coupling to the ambient plasma after the expansion overruns the density jump is greater in the case of the non-uniform ambient plasma simulation.

Since the electric and magnetic fields are responsible for coupling energy and momentum to the ambient ions, one would expect stronger fields in the lower density region, where the coupling is enhanced. Following the procedure outlined in Wright[46], one can derive $\vec{E}$ and $\vec{B}$ for a cylindrical expansion analogously to a spherical expansion. The model assumes unmagnetized debris ions that expand out radially, ambient ions which are stationary and uniform, and completely magnetized electrons that are bound to magnetic field lines. This model neglects electron inertial effects and electron pressure. The magnetic field is modeled as three regions: a cavity where $B_z = 0$, a magnetic field compression in $\hat{z}$ with an associated electric field in $\hat{\phi}$ that causes the electrons to $E_\phi \times B_z$ drift outward radially in a shell, and a region outside of the shell with uniform magnetic field B_0. For a given radius R_s, which is the outside radius of the shell, there is a shell thickness $\Delta R/R_s \approx 1/2 \frac{m_d/m_i}{Z_d} \left(\frac{R_s}{R_m}\right)^2 \propto n_i$ for $(R_s/R_m)^2 \ll 1$. The shell thickness, which is a parameter present in the field solutions, is determined using quasineutrality; thus it is proportional to the ambient ion density. The magnetic field inside the shell can be expressed as $B_z/B_0 = 1 + \frac{Z_d}{m_d/m_i}\left(\frac{R_m}{R_s}\right)^2$, which means that the field compression is inversely proportional to the ambient ion density. The electric field in the shell is given by $E_\phi/B_0 = \mathcal{M}_A \left(\frac{\Omega_i}{\omega_{pi}}\right)\left(\frac{r}{R_s}\right)\frac{Z_d}{m_d/m_i}\left(\frac{R_m}{R_s}\right)^2 \propto n_i^{-3/2}$, where r is the position inside of the shell. These analytical expressions for E_ϕ and B_z dictate that the physical electric and magnetic fields are stronger in lower density background plasmas. A full derivation and discussion of the Wright model can be found in Appendix B.

Fig. 3.10 shows the fields associated with the electromagnetic pulse. While the analytical model and simulation do not match up exactly at early times (not shown) because the initial debris cloud has a finite extent in the hybrid simulation, the simulation shows that the fields are in fact larger as the pulse overruns the density jump at $t\omega_{ci} \sim 1$, which leads to better coupling and energy transfer from the debris ions to the ambient ions. The analytical model is no longer valid after any ambient ions have been swept up, but it does provide some insight into the coupling physics. Launching a magnetosonic pulse into a low density region, which then propagates into a higher density region improves

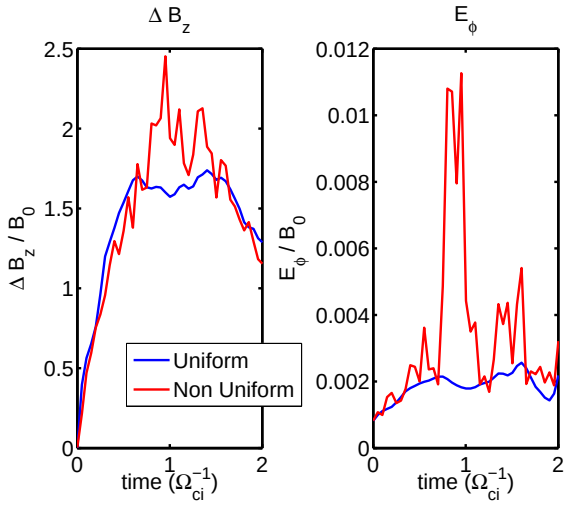

Figure 3.10: $\Delta B_z/B_0$ and E_ϕ/B_0 maximum values on the line $x > 0$ and $y = 0$ vs. time for uniform (blue/lower line) and nonuniform (red/upper line) simulations.

coupling due to larger electromagnetic fields in the compressed electron shell that interact with the ambient ions.

Figure 3.11 shows several interesting features at a time just before the pulse runs over the density gradient. The azimuthal and radial components of the electric field are larger in the nonuniform (Fig. 3.11b) simulation at this time compared to the uniform case (Fig. 3.11a). The magnetic field compression in the nonuniform case leads the debris ion cloud more than in the uniform case. The phase space (Fig. 3.11c) shows that the bulk of the ambient ions for the nonuniform case are accelerated to a velocity in excess of twice that of the uniform case. The stronger E_ϕ accelerates the ambient ions faster in the nonuniform case, which then turn upstream in the enhanced magnetic field and get ahead of the piston[24]. The density is swept out more effectively behind the magnetic pulse due to the larger electric field, as shown in Fig. 3.11d. In the low density region of the nonuniform simulation a larger percentage of debris ions participate in transferring energy to the ambient ions and do not slip out past the cavity, or do not "decouple" in the parlance of Hewett[24]. The enhanced coupling in the low density region limits the number of particles that "decouple," which increases the energy transferred to the

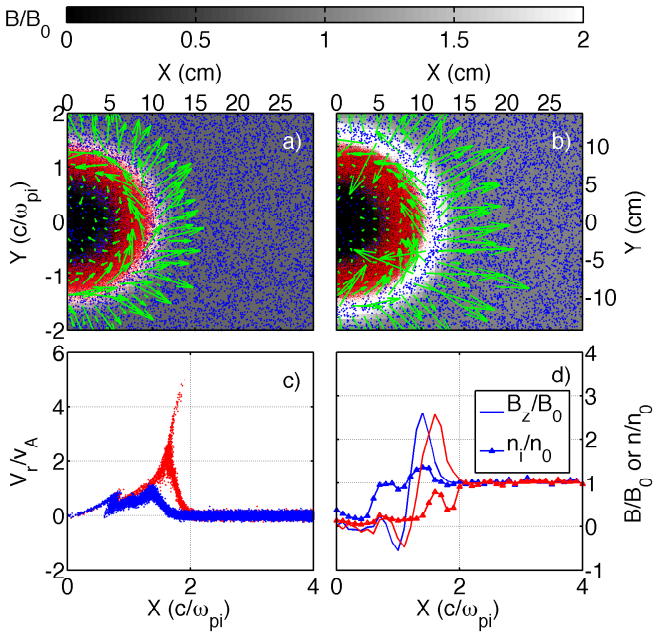

Figure 3.11: Simulation output at a time $t\omega_{ci} \sim 0.5$. Panels (a) and (b) are composite figures which show B_z in grayscale over the simulation domain, a sampling of debris ions (red) and ambient ions (blue), as well as relative electric field strength and direction (green arrows). Panel (c) shows an overlay of the phase space of the ambient ions for the uniform (blue/lower) and nonuniform (red/upper) simulations. Panel (d) shows overlays of the magnetic field for uniform (blue line to left) and nonuniform (red line to right) cases as well as ambient ion density for the uniform (blue/upper line with triangles) and nonuniform (red/lower line with triangles) simulations.

ambient ions.

In summary, this section takes a first look at extending shock formation theory to more realistic conditions with the aid of hybrid simulations. In contrast, previous theories for shock formation using diamagnetic bubbles as a piston typically consider the ambient ions as initially uniform, and the expansion as either cylindrically or spherically symmetric. It has been shown analytically and computationally that a density gradient enhances coupling, reduces the shock formation time and increases the Mach number of the shock, which are important for the design of laboratory shock experiments.

Chapter 4

Three Dimensional Hybrid Simulation of the 2013 LAPD Shock Experiment

In the years since the 2013 LAPD experiment was initially analyzed in part using the 2D hybrid code[2], a 3D code has been developed named fHybrid3D. The major improvement to the code other than extending it to three dimensions is that it can perform its computations across several compute nodes allowing the full 3D problem to be solved on supercomputers. More details regarding the computational algorithm and efficiency can be found in Appendix A. A benefit of the 3D code is that it allows the simulation initial conditions to more closely resemble those of the actual experiment. This chapter presents output from fHybrid3D, which is then compared to the experimental data as well as a 2D simulation using similar initial conditions.

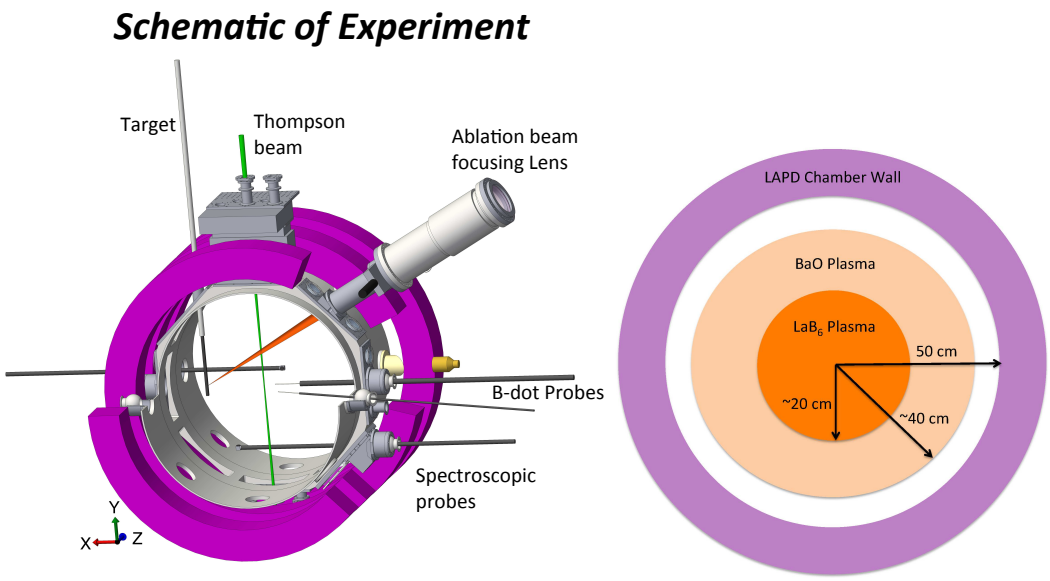

(a) (b)

Figure 4.1: (a) Schematic of experimental setup on Port 19W of LAPD, and (b) cartoon representation of the plasma cross-section in LAPD.

4.1 LAPD Shock Experimental Setup

Figure 4.1a shows a rendering of the LAPD experiment with several diagnostics including spectroscopic probes, a Thomson scattering beam, and magnetic flux (B-dot) probes. This chapter will focus almost solely on the magnetic flux probe data. This data is the most easily accessible and can be compared directly to simulation output. The spectroscopic data as well as the Thomson scattering data require more in depth analysis and are detailed in other recently published works[48, 49]. There are two B-dot probes used during this experiment, a single axis five tip probe with centimeter spacing to quickly sample B_z along the blow-off axis, and a 3-axis probe that is off at a $\sim 30°$ angle pointing toward the target. The data from both of these probes will be compared to various simulations that will follow in the subsequent sections.

Figure 4.1b is a cartoon of the non-uniform plasma that is created in the LAPD for

this experimental setup. The background gas that is used in all the experimental runs in this chapter is hydrogen. Other gases are used for data collected during our experimental runs, but the scope of this chapter will be limited to the hydrogen runs. As shown in the previous chapter, density gradients affect how a shock is formed, so capturing this feature is important for the simulations. This is approximated in simulation by having a column of hot plasma with a Gaussian profile.

4.2 New Initial Conditions for Hybrid Simulations

In the previous simulations a simplified set of initial conditions were used where the debris plasma was modeled either as a drifting Maxwellian distribution, or as a cylindrically symmetric expansion of v_d with a small thermal distribution. In the simulations presented in this chapter and the next, a distribution inspired by experimental data will be used.

It became apparent after the 2013 shock campaign that the initial conditions of the laser blow-off needed to be improved to better account for the proper energy density of the ablated plasma. Figure 4.2a is a fast-gate photograph with a spectral line filter to allow self-emission of light from excited C^{+4} to pass through. It gives an idea of the shape of the plasma plume, as well as an image of some of the instabilities that grow on the edge of the bubble during expansion. The flute modes that show up in figure 4.2a could be attributed to the electron-ion hybrid instability[50], which is not reproduced with the hybrid code, since it requires a non-zero electron mass. The repetitive nature of the experiment will also average over different instances of these instabilities yielding probe measurements that do not capture these modes after averaging a sufficient number of laser shots. The image in figure 4.2a is taken from a single laser shot and the flute modes are resolved. After trying a couple of different geometries inspired by the image, a model was settled on that comes from experimental measurements of laser plasmas ablated in a

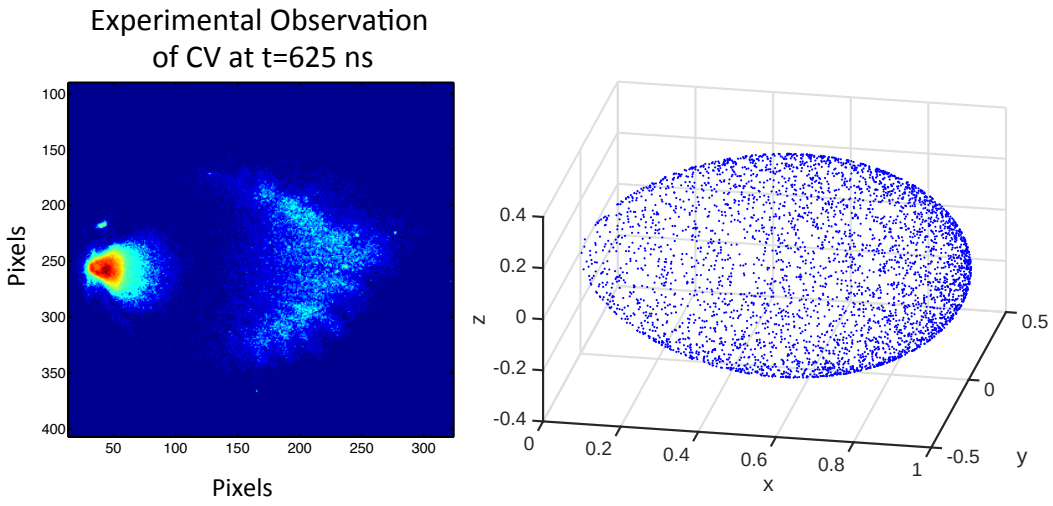

(a) (b)

Figure 4.2: Panel (a) shows a filtered image of C^{+4}, which is roughly 30×30 cm, with the magnetic field going into the page. The target is on the left at x=20 pixels and explodes to the right. Panel (b) shows a normalized velocity distribution used in the simulation.

vacuum using similar targets and laser irradiance[51, 42, 43]. The measurements lead to an empirical model that has an angular distribution relative to the target normal vector. In the following equations, θ represents the angle off of the target normal. The laser plasma has the following dependences:

$$v_r(\theta) = v_d \cos^2(\theta)\,,\ n_d(\theta) = n_{d0} \cos^4(\theta)\,. \tag{4.1}$$

Figure 4.2b is generated by taking the relations in Equation (4.1) and plotting test particles that start at the origin and ballistically expand such that the fastest particle is at $(x, y, z) = (1, 0, 0)$. It graphically represents the velocity distribution function. It will be seen in the remainder of the thesis that this distribution matches well with experimental measurements and leads to 3D simulations of higher accuracy and fidelity.

4.3 Simulation Conditions

The 3D simulation was performed using fHybrid3D in a cube domain of size $32 \times 32 \times 32$ c/ω_{pi}, and 180 cells in each dimension, leading to a cell size of 0.18 c/ω_{pi}. The reference density in the simulation is chosen to be $n_0 \sim 1.5 \times 10^{13}$ cm^{-3}, which corresponds to the peak density in the LAPD. The reference mass and charge state are that of H^{+1}, with $m_0 = m_p$ and $Z_0 = 1$. This leads to an ion inertial length, which determines the coordinate scaling of the simulation system, of $c/\omega_{pi} \sim 5.9$ cm. The background magnetic field strength is $B_0 \sim 300$ G. This determines the Alfvén speed in the plasma core of $v_a \sim 170$ km/s. The plasma ablated from the polyethylene (C_2H_4) target is initially placed in a Gaussian shaped spot centered at $(x, y, z) = (8, 16, 16)$ c/ω_{pi}, with a standard deviation $\sigma \sim 0.25$ c/ω_{pi}. The debris consists of two species, namely C^{+4} and C^{+3}, in which the C^{+4} acts as the driving piston and the C^{+3} is a warm cloud that follows behind the piston to backfill the cavity[52]. The C^{+3} is used to approximate all lower charge states of carbon and supplies ions and electrons that ballistically free stream within the diamagnetic cavity as well as supply a diamagnetic current path which returns back to the target location. This alleviates the hybrid code from having to deal with vacuum regions, and helps with the diamagnetic cavity expulsion and formation, without having to track all species of debris ions. The velocity distribution used for both debris species consists of a combination of the aforementioned conditions in Equation (4.1) that determine particle drift velocities, and a Maxwellian thermal distribution. The C^{+4} plasma has a peak drift velocity in $\hat{x}$ of $v_{d0} \sim 500$ km/s and a thermal velocity of $v_{td} \sim v_{d0}/2$. The C^{+3} plasma has a peak drift velocity of $v_{d0} \sim 300$ km/s and a thermal velocity $v_{td} \sim 0.85 v_{d0}$. The piston of C^{+4} then has a peak expansion Mach number of $\mathcal{M}_A \sim 3$. The number of particles is chosen such that the total kinetic energy in the piston is $E_d \sim 55$ J and the energy in the trailing debris cloud of C^{+3} is 60 J. The laser energy fluctuated between 150 - 200 J in the experiment, so this is roughly a 60% conversion of laser energy to debris kinetic energy, with ~ 25 % of the energy going into the piston. The energies were chosen by matching the

final diamagnetic bubble size to that measured in the experiment. The ambient plasma density is non-uniform, with a density of H^{+1} of $n_i \sim 0.3n_0$ that peaks at $n_i \sim n_0$ in a column that spans the $\hat{z}$-direction in the domain uniformly and has a Gaussian profile in the $\hat{x}$ and $\hat{y}$ directions, that is offset from the target by $(5.1, 1, 0)\ c/\omega_{pi}$, with a standard deviation $\sigma \sim 1.53\ c/\omega_{pi}$.

It is interesting to view a full 3D composite image of magnetic fields along with a sampling of the ions to visualize what is happening in the LAPD laser experiments. Figure 4.3 shows slices of data through the data cube that give an idea of what the 3D structure of the magnetic field looks like. The ions are overlaid to see how they contribute to the dynamics. A diamagnetic cavity is formed in the wake of the debris ions (cyan), where the magnetic field is expelled. At this point in time the cavity is nearing the end of its expansion, and the debris ions are mostly confined to the edge of the cavity. Ahead of the debris ions, it can be seen that the high density region of ions, denoted by black, are displaced. The magnetic compression is mostly being carried by the high density ambient plasma. The trailing lower charge debris species is not shown for clarity, but they sit inside of the diamagnetic cavity. Now that a 3D simulation has been calculated, it is time to perform a detailed comparison to the experimental data.

4.3.1 Magnetic Field Data

The primary diagnostic for the experiment was a 5-tip single axis magnetic flux probe. It's design and construction are similar to the 3-axis magnetic flux probe designed by Everson[31]. The difference is that this probe has five single $\hat{z}$-aligned coils spaced by 1 cm. The probe was designed to be able to collect data at multiple points from a single laser shot since the repetition rate of the Raptor laser is 45 minutes. This allows for more rapid scanning along the $\hat{x}$ axis.

Figure 4.4 is the main measurement that was compiled over several days worth of

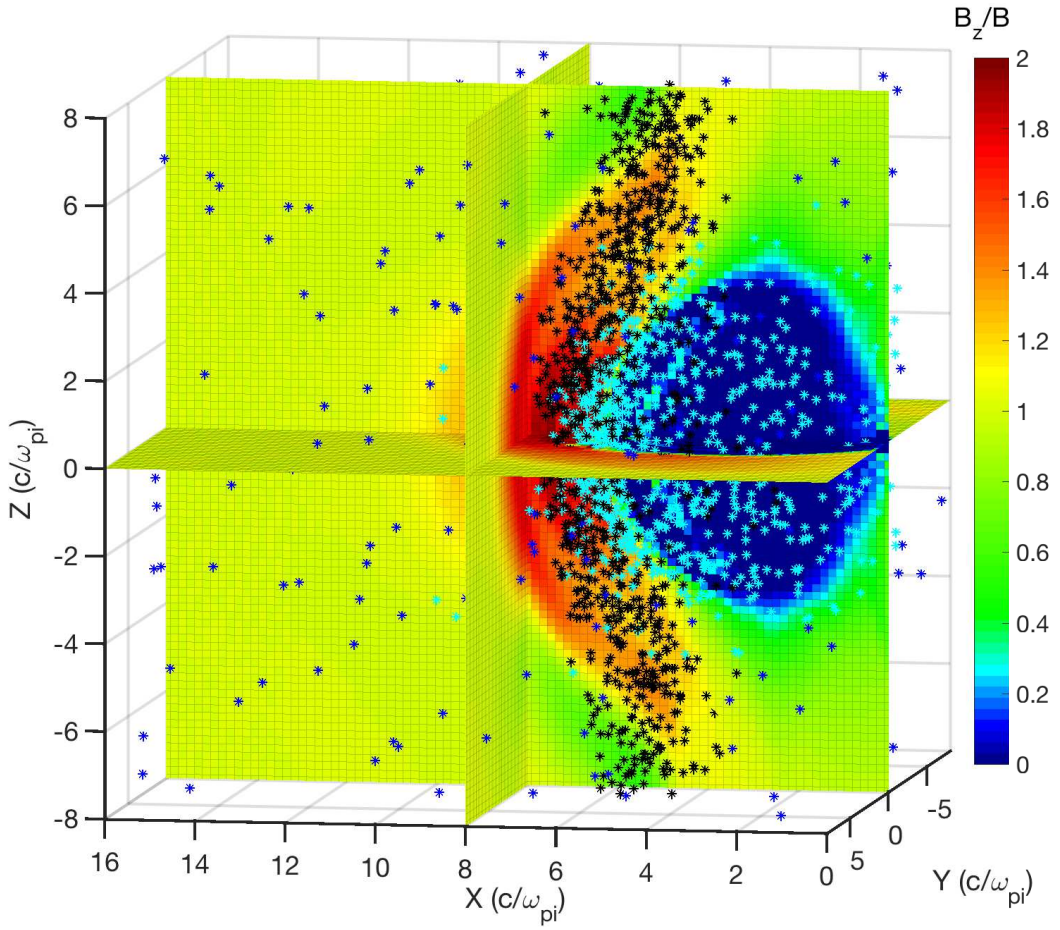

Figure 4.3: Composite 3D slice figure showing B_z, with all planes intersecting (x,y,z) = (8,0,0) c/ω_{pi}, along with a sampling of debris (cyan), ambient (blue), and non-uniform ambient (black) ions, at time $t\omega_{ci} \sim 3$.

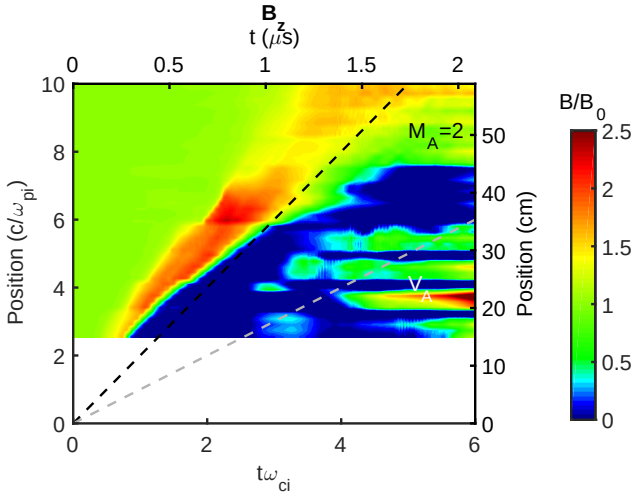

Figure 4.4: A composite of several experimental shots to obtain a spatial profile of B_z along the blow-off axis.

laser shots. This was the first experiment in which a sub-critical magnetized collisionless shock has been launched[2]. Previous two-dimensional simulations suggested that this was indeed a steepening shock that is forming in the high density region of the LAPD plasma. The front of the measured magnetic compression at $t\omega_{ci} \sim 2.3$ near the spatial position of $\sim 6c/\omega_{pi}$ away from the target shows a ramp in which the magnetic field compresses by a factor of two within a single ion inertial length (c/ω_{pi}). This compression is consistent with the Rankine-Hugoniot jump conditions for a $\mathcal{M}_A \sim 2$ shock-wave. The front of the compression is peeling away from the diamagnetic cavity that is slowing down and moving away from the piston debris ions, which should be located near the diamagnetic cavity's edge. Since the ambient plasma is hydrogen, emission spectroscopy could not be used to measure the velocity of the ambient plasma. The Thomson scattering diagnostic in the experiment did not yield measurements of the temperature and velocity of the electrons in the shock-wave due to issues with stray light. Since the measurements were sparse, hybrid simulation becomes an important tool for analysis. Up until this point in time, only a couple of 3D hybrid runs were performed using the LLNL massively parallel hybrid code[24]. Most previous analysis was done with the aid of the 2D hybrid code from Los

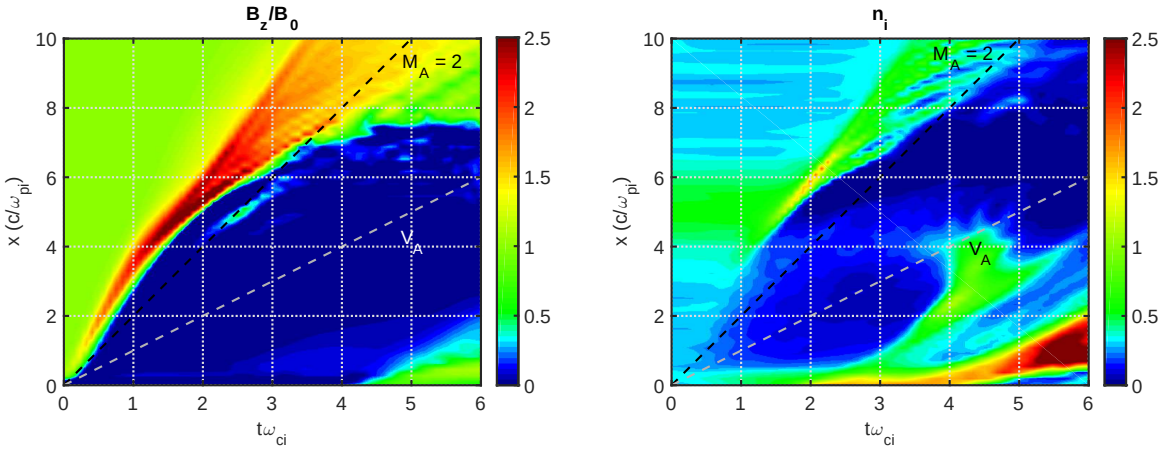

(a) (b)

Figure 4.5: Output from fHybrid3D along the blow-off axis for (a) B_z and (b) n_i.

Alamos.

In order to be able to use the hybrid simulation output to learn about our physical system, we first need to make sure that it matches the measured observable in the experiment. Figure 4.5a shows a streak plot from the 3D simulation. The energy put into the debris cloud was chosen so that the extent of the diamagnetic cavity matched the experimental observation. This is due to Equation (2.11), which relates the size of the cavity to the debris kinetic energy. Qualitatively, figure 4.4 and figure 4.5a are quite similar. The pulse has an initial velocity around $\mathcal{M}_A \sim 3$ and a similar magnetic pulse width. The magnetic field compression in the simulation is close to that of the experiment and again, satisfies the RH jump conditions. If we look at figure 4.5b, we see the simulation output of the ambient ion density which shows a compression of the ambient ions in the shock front. These ions are picked up by the piston via collisionless coupling mechanisms, are sped up to roughly the piston speed and compressed into a downstream region.

If we look at spatial line-outs that are over-plotted with one another we can see how well the simulations match that of the experiment. In figure 4.6 we can see two important times in the experiment. The first depicted in figure 4.6a is at a time when

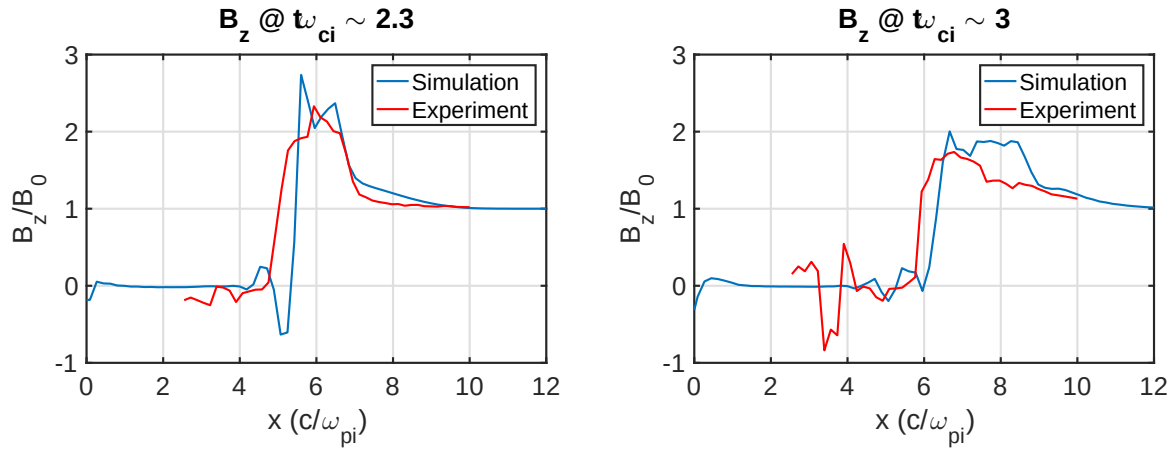

(a) (b)

Figure 4.6: Spatial line-outs at times (a) where the ambient plasma is shocked in the high density plasma region, and (b) after the pulse has run into the lower density ambient plasma.

the ambient plasma is compressed, the magnetic field is compressed, and a shock-wave is forming and peeling away from the piston. The shock ramp at $x \sim 7c/\omega_{pi}$ coincides well. The simulation has a magnetic foot that may come from a velocity distribution that has a few more debris particles that slip through just in front of the magnetic pulse and couple some energy into the leading ions. The cavity edge also looks to be slightly ahead of the measured cavity edge at these times, but ultimately pushes out to the same size. Without knowing the exact debris distribution functions it is difficult to replicate the experiment precisely, but in spite of that fact the agreement is very good. If we look to figure 4.6b, we see at later times that the compression in the experiment dies out faster than that of the simulation, but still agrees well with width and magnitude of the compression. It could be that the energy variance from shot to shot leads to this discrepancy as the energy varies by up to 20 J, or the ambient plasma column could have changed parameters as it slowly changes throughout the day. Without doing multiple shots to average over these variations and get better measurement statistics it is difficult to determine the source of the difference. In general though, the measurements and the simulation agree quite well.

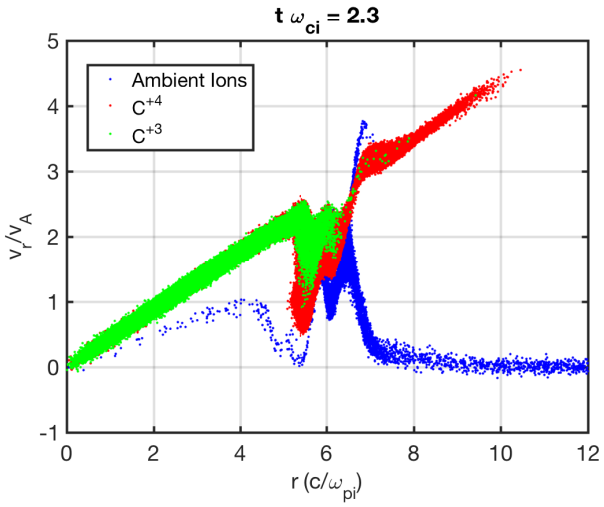

Figure 4.7: Radial phase space output from fHybrid3D in the X-Y plane coincident with the target.

In order to get a better feel for the ion dynamics in the simulation, it is imperative to examine the ion phase space plot. Figure 4.7 shows the phase space plot for a sampling of particles from each of the ion species in the simulation. These are calculated by collecting particles that are within a quarter of an ion inertial length of the X-Y plane that corresponds to $z = 0$, the target plane. The particles are then projected into the radial phase space figure to see what the ions are doing. Upon examination of figure 4.7, one can see that at the location of the shock ramp ($\sim 7c/\omega_{pi}$) that the ambient ions are being reflected ahead of the shock ramp. Looking at the particles between 5-7 ion inertial lengths away from the target, we see that the carbon ions have been slowed and the ambient ions sped up into a downstream region, which has a velocity near $\mathcal{M}_A \sim 2$. The C^{+3} sits in the diamagnetic cavity, and the C^{+4} interacts with the H^{+1} to impart momentum and generate a shock. Ahead of the shock, there are streaming debris ions which do not fulfill the coupling criteria and move out in front of the shock.

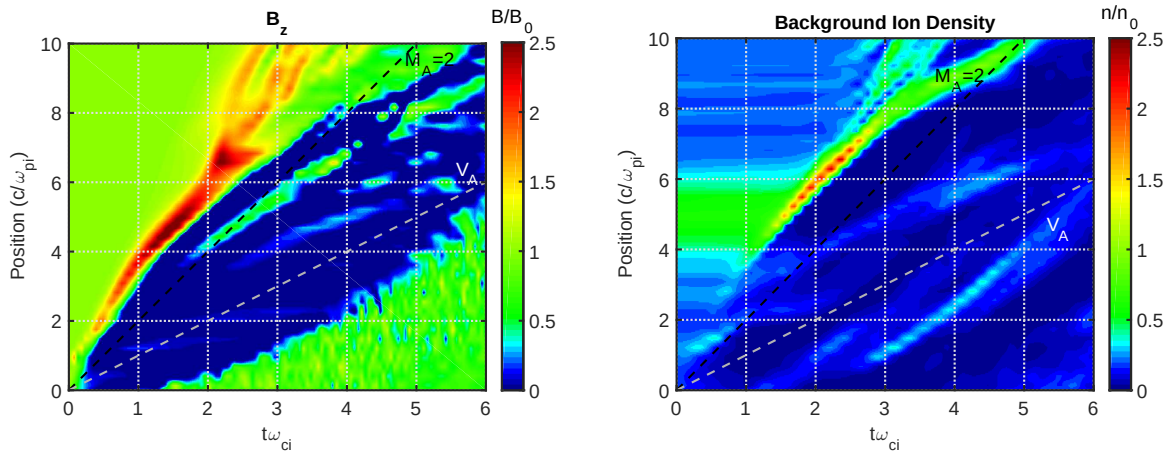

(a) (b)

Figure 4.8: Output from FPIC-2D along the blow-off axis for (a) B_z and (b) n_i.

4.4 Comparison to 2D Simulation

This section will highlight some of the differences between the 3D simulation and a comparable 2D simulation using the same initial conditions and domain setup, including an inhomogeneous ambient plasma. The 2D code used in chapter 3 is configured similarly to the 3D simulation so that the debris initial conditions, bubble size, and ambient plasma conditions are as close as possible. There are obvious geometric differences, since in 3D the plasma blow-off is finite in extent along $\hat{z}$, whereas the 2D hybrid code assumes uniformity in $\hat{z}$. The initial conditions are the same in the X-Y plane and follow the distributions given in Equation (4.1). The energies are normalized so that in 2D and 3D the equal mass radii are similar.

Figure 4.8 shows corresponding output from the 2D code FPIC-2D using the same initial conditions as the 3D code. Since the energy density in the system drops slower in 2D due to geometric constraints ($1/r^2$ falloff vs. $1/r^3$), the energy density of the piston stays stronger for longer and generates larger compressions in density and magnetic field. The current density associated with the edge of the cavity also stay stronger for longer in

2D leading to enhanced azimuthal electric fields that couple energy to the ambient ions. Figure 4.8a shows a cavity that has a different shape in the streak plot and decelerates much slower than that of the 3D case depicted in figure 4.5a. The peak magnetic field compression in figure 4.8a is greater than $B/B_0 \sim 2.5$, and the velocity of the front of the shock-wave is faster than that of the 3D expansion in figure 4.5a. Figure 4.8b shows a compression similar to the 3D case, but with a larger magnitude. The density expulsion mimics the size and shape of the diamagnetic cavity. All of these subtle differences lead to an increase in the magnetic and electric fields in the 2D geometry, which in turn leads to slightly increased coupling and shock generation. This should be noted as previous analysis using the 2D code overestimates coupling slightly, but still is useful for examining the relevant physics since the 2D code runs faster, is easier to visualize, and does not require special computing resources to run. The 3D code in turn reproduces the experimental dynamics more closely and is a better tool for analysis so long as the computational resources and expertise are available to run the more complex code.

4.5 Conclusions

In this chapter, the 2013 LAPD shock campaign was discussed in the context of simulating the experiment. Three dimensional simulations were presented which agree quite well with the data and corroborate the claim that it is in fact a sub-critical shock that is being formed in the high density plasma in the LAPD. It may not be fully formed and separated from the piston, since this would require several ion cyclotron periods to completely form the downstream region of the shock that we normally associate with a steady state shock that is observed in space. A 2D simulation was presented in which it is shown that the two-dimensional geometry, which assumes uniformity along $\hat{z}$, predicts stronger coupling and compressions than in 3D. Ultimately, the 2D code is a great tool to rapidly explore parameter regimes for shock formation, but when analyzing actual data

the 3D code is superior in that it reproduces features of the simulation without having to fudge the debris energy for a particular simulation.

Chapter 5

High Repetition Rate Experimental Data and Simulations

In this chapter, three-dimensional hybrid simulations are compared to high repetition rate data obtained in the LAPD using the Peening laser. The Peening laser is a 1053 nm Nd:Glass laser that is designed to operate up to 6 Hz with each shot having roughly 20 J of energy. This is an order of magnitude less that the Raptor laser, but the high repetition rate allows us to gather much more data. The experimental setup is similar to that of the high energy shock experiment, except instead of a single axis 5-tip B-dot probe as the primary diagnostic, a traditional 3-axis B-dot probe with a single tip and an emissive probe are fielded. The emissive probe is a newly designed probe similar to that of a Langmuir probe, except that the tip of made of a highly emissive material that thermionically emits electrons when heated[3]. This allows the probe potential to settle to the local plasma potential. Measuring the plasma potential at a fine enough spatial resolution allows the electrostatic component of the electric field to be calculated. The emissive probe has previously been fielded to measure electrostatic potential in sub-Alfvénic expansions in the LAPD[53]. Since the electric field will have both electrostatic and inductive fields,

it is preferred to transform simulation data into the electrostatic potential and compare to the experimental data directly. The comparison of the potential structure will allow us to examine how well the adiabatic electron pressure model represents the physics of the experiment. These measurements of the experiment are used to validate and benchmark the hybrid model in which the electrons are treated as a compressible, adiabatic fluid.

5.1 Experimental Setup and Simulation Parameters

The experiment again uses a multi-cathode setup in which there are two opposing cathodes at each end of the LAPD that generate an inhomogeneous plasma, which has a dense core ($n_i \sim 1.6\times10^{13}$ cm^{-3}) with a diameter of ~ 40 cm in the middle of the machine, surrounded by lower density plasma ($n_i \sim 5 \times 10^{12}$ cm^{-3}). The simulation models this using periodic boundary conditions that are sufficiently far to not affect the simulation during the cavity and magnetosonic wave formation. The ambient plasma consists of ionized hydrogen, so the ion inertial length is $c/\omega_{pi} \sim 5.7$ cm in the dense center of the plasma column. The simulation models the plasma column as having a Gaussian profile in $\hat{\mathbf{x}}$ and $\hat{\mathbf{y}}$ with a standard deviation of $\sigma = 12.1$ cm, and a target offset of 20 cm to the center of the high density plasma. The plasma has uniform distribution along $\hat{\mathbf{z}}$. The simulation domain consists of 180^3 cells, each plasma species has 100 particles-per-cell if they were uniformly distributed throughout the domain. The domain length in all three dimensions is $L_x = L_y = L_z = 24\, c/\omega_{pi} = 136.8$ cm, so each cell has a dimension of $\Delta x = \Delta y = \Delta z = 0.13\, c/\omega_{pi} = 0.76$ cm, which resolves the ion inertial length nicely and also has a similar resolution to the experimental measurements of 1 cm spacing. The ambient electron fluid has a temperature $T_e \sim 10$ eV, and the ambient ions have a temperature $T_i \sim 1$ eV. The debris is initialized in a similar fashion to what was presented in chapter 4, but this time the driver species of C^{+4} has a total initial kinetic energy of 4 J, with a blow-off speed of 325 km/s and a thermal speed of 80 km/s. The trailing

species of C^{+3} that is meant to embody the remainder of the charge species ablated from the target has a drift velocity of 200 km/s with a comparable thermal speed, with a total kinetic energy in this species of 6 J. This gives a total of 10 J of total debris kinetic energy in ionized species, where the rest could go into heating the target. This gives a piston conversion efficiency of 20% and a total conversion efficiency to kinetic energy of 50%, which is not unreasonable. Without full experimental diagnosis of the velocity distribution of the ablation beam, this seems to work as a good estimate. The electrons that come from the laser debris initially are very hot, but by the time the hybrid simulation starts the electrons cool down to a much lower temperature than that of the ambient plasma, so they are modeled as having zero temperature. This alleviates several initialization problems with the hybrid model where it was difficult to determine the amount of energy initially in the simulation due to having large pressure gradients over a single cell that would seed numerical instability. If we examine Figures 4.1 and 4.2 in D. B. Schaeffer's dissertation[48], we see that in the LAPD and in the Phoenix laboratories test chamber, for typical experimental irradiance, the debris electron temperature falls near to zero in under a few cm and under a tenth of a μs. The LAPD experiments with a hydrogen gas fill have typical ion inertial length of ~ 6 cm and an cyclotron frequency $\omega_{ci} \sim 1.9 Mrad/s$, which gives a time-scale of $\tau_{ci} \sim \omega_{ci}^{-1} \sim 0.5\mu$s. The hybrid simulation is initialized over some fraction of an ion inertial length and only resolves the physics on the time-scale of τ_{ci}. If we examine the Thomson scattering data presented by Schaeffer, we see that on the initialization time and length scales of the simulation, the debris electron temperature drops down to near zero by the time we reach relevant length or time scales for hybrid simulation. We are effectively initializing the simulation after the debris electrons have already imparted their energy to the debris ions, and the cold debris electron approximation is valid and appropriate.

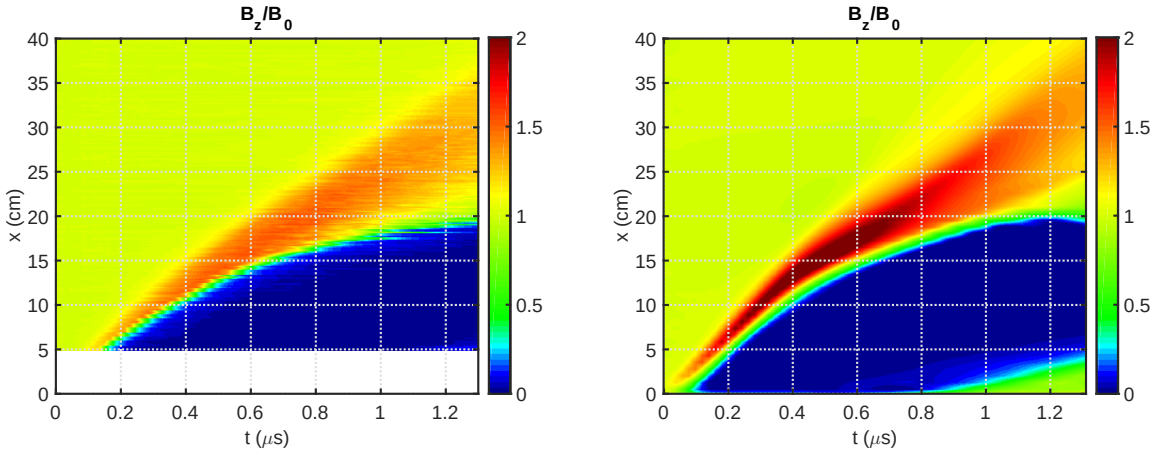

(a) (b)

Figure 5.1: Shows (a) measured experimental B_z along the blow-off axis and (b) the corresponding output from fHybrid3D.

5.2 Magnetic Field Data Comparison

The first diagnostic that was used during the Peening campaign was a single-tip 3-axis magnetic flux probe with a tip width of $\mathcal{O}(1mm)$. A fine scan of the probe along the blow-off axis was measured with 0.5 cm measurement spacing. Figure 5.1 shows the compilation of time integrated B-dot signals that is very similar to the data collected during the shock campaign, though with better resolution. These measurements should be slightly better than those taken with the 5-tip probe as the Peening energy stability from shot to shot is better, and there are not shadowing problems with the trailing tips, and well as potential cross-channel interference. The simulation was initially matched to have the same cavity diameter of $\sim$ 20 cm, as well as a similar initial blow-off to match that of the experiment. The cavity edge, as well as the front of the magnetic pulse line up well between Figures 5.1a and 5.1b, and the cavity is fully expelled in both cases. The ablations in this experimental campaign are around $\mathcal{M}_A \sim 1.5$, which according to the RH jump conditions should have a compression ratio of $r \sim 1.6$. The magnetic field looks like it could be near the jump conditions, but if examining the density in the

simulation (not shown), it shows compression of the ambient plasma, but it does not quite reach the jump conditions. There appears to be significant energy coupled to the ambient ions, but the magnetosonic pulse does not quite steepen into a shock. Some differences between the simulation and the experiment are that the magnetic compression in the simulation is much higher than that measured. This could potentially be due to the fact that the magnetic flux probe has a finite bandwidth in the amplifier, as well as some inductance that could counteract some of the high frequency magnetic field changes. The simulation also tends to exhibit some overshooting at sharp transitions, which is evident in Figure 4.6, where the experimental data and simulation data are overlaid. The edge of the magnetically expelled region has an overshoot and undershoot associated with the sharp magnetic field transition, which could possibly be due to a disagreement between the simulation initial debris conditions and those of the experiment. Though in spite of the disagreement in that one region, the figures look very similar. The hybrid simulation appears to be capturing the relevant physics of the expansion, at least along the blow-off axis. Further experimental measurements of the laser ablation will be required to fine tune the ablation model.

In previous experimental campaigns Figure 5.1 was nearly all the data that would be available after several weeks of using the Raptor laser as the ablation beam. This experiment is quite different in that orders of magnitude more measurements can be made during a given experimental run using the Peening laser as an ablation beam. Though a shock is not generated in this case, the simulation data is a useful tool to validate the hybrid simulation model. So for the remainder of this chapter, X-Y and X-Z planes of data will be compared to the corresponding data from fHybrid3D at various times chosen to represent different phases of the expansion.

Figure 5.2 shows a side-by-side comparison of three-dimensional magnetic field data. The colored plot shows the compression of the magnetic field, and the overlaid arrows give the relative strengths and directions of B_x and B_y. This way all three com-

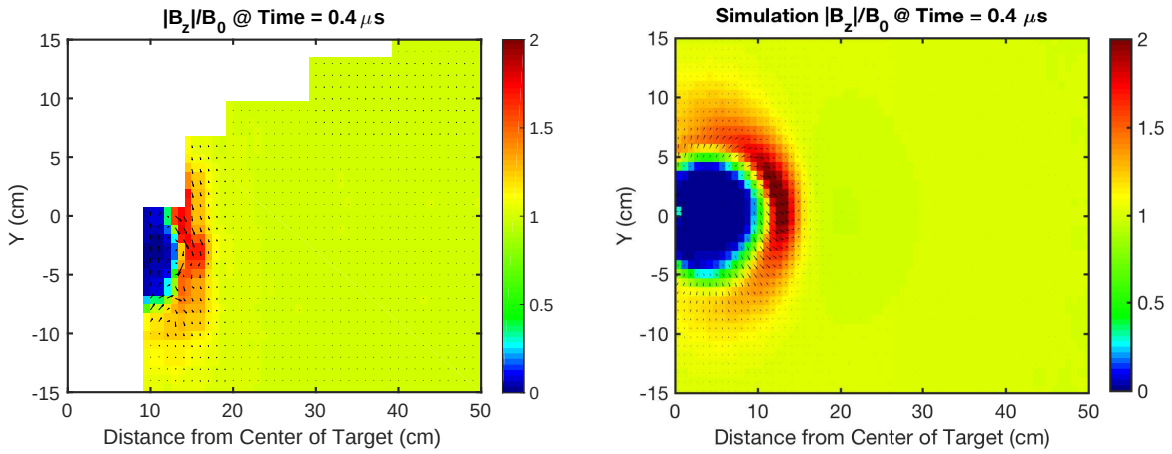

(a) (b)

Figure 5.2: Shows (a) measured experimental B_z in an X-Y oriented plane at $t = 0.4\mu$s, with arrows over-plotted to show direction and magnitude of transverse B field, and (b) the corresponding output from fHybrid3D.

ponents can be qualitatively compared. The magnitude of B_z is compared so that the values would be positive, since in LAPD coordinates the background magnetic field is counter-aligned with $\hat{\mathbf{z}}$, or $\mathbf{B_0} = -B_0\hat{\mathbf{z}}$. The simulation data is transformed to LAPD coordinates for direct comparison to the data. In Figure 5.2a there are several patches of data that could not be collected due to the fact that the probe would be too close to the ablation beam. These values are filled in as NaN, and is rastered as a blue patch. The rest of the X-Y figures presented in this chapter will have similar structure. The time at this point is 0.4 μs, which is during the coupling phase, where the debris plasma is slowing down and the ambient plasma is being accelerated. One thing to notice at this early time is that off of the blow-off axis, the diamagnetic bubble has a larger extent than that of the simulation. This would seem to imply that the initial debris distribution off of the target normal has a different distribution that that which is currently being used to initialize the simulations. This discrepancy suggests that a full distribution measurement in the future would be beneficial in order to match the experimental data better. The initial experimental data suggests that a larger angular extent of debris ions may be necessary.

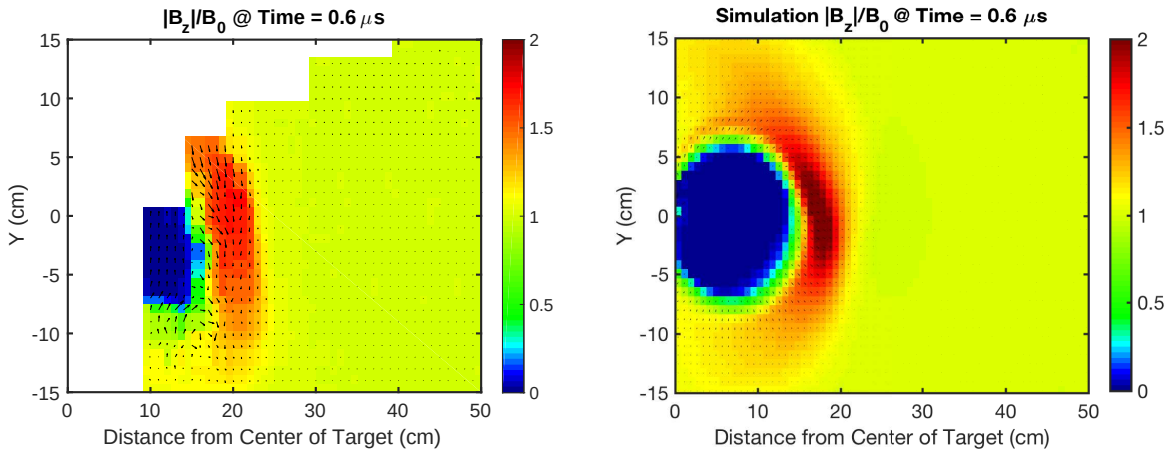

(a) (b)

Figure 5.3: Shows (a) measured experimental B_z in an X-Y oriented plane at $t = 0.6\mu$s, with arrows over-plotted to show direction and magnitude of transverse B field, and (b) the corresponding output from fHybrid3D.

Though the simulation has a more spherical bubble extent off axis, the magnetic field structure and magnitude match quite well.

Figure 5.3 is at a time in which most of the debris should be slowing and the ambient ions are compressing a bit. The magnetosonic pulse is starting to be carried by the ambient plasma and the pulse front begins to peel away from the cavity edge. This looks similar to Figure 5.2, though it has progressed a bit in time. The extent of the cavity has a similar look, in which it is not fully expelled in the experiment near the leading edge of the cavity. This probably has to do with the fact that the trailing ions are being approximated as a warm cloud of C^{+3}. This is also during the phase of the expansion when the magnetic pulse is propagating through the most dense region of the ambient plasma. The plots used to determine the ambient plasma density and extent are not Gaussian, so some of the deviation could be due to the fact that the real density is not an exact Gaussian distribution in space. Though, again the pulse has a similar shape in the simulation, which begins to start turning upward as it interacts with the higher ambient plasma density. The direction that it turns follows that of a free streaming ion

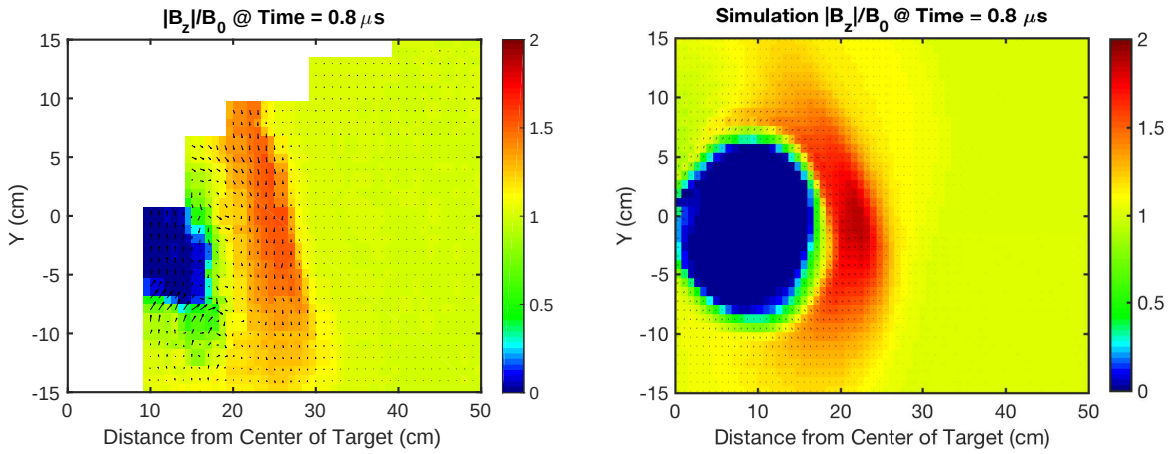

(a) (b)

Figure 5.4: Shows (a) measured experimental B_z in an X-Y oriented plane at $t = 0.8\mu$s, with arrows over-plotted to show direction and magnitude of transverse B field, and (b) the corresponding output from fHybrid3D.

that leads pulse. That is, the front of the wave is no longer vertical, but has some tilt to it indicating a wave vector that is turning upward away from the $\hat{\mathbf{x}}$-axis.

Figure 5.4 is near when the diamagnetic bubble is nearing its maximum size, and the bubble expansion rate is decreasing. The magnetic field compression on axis is again larger than measured experimentally. The cavity has a larger extent along the $\hat{\mathbf{y}}$ direction in the experimental measurements. This again implies that the angular distribution of the debris blow-off should be examined further. The front of the magnetic pulse is now beginning to curve upward in the figures, which the simulation matches nicely.

Figure 5.5 is when the bubble is at its largest, and the pulse is moving away from the cavity edge. The experimental cavity has diminished significantly more than that of the simulation. The simulation cavity has also shifted downward as the ions gyrate upward. The pulse front does still appear to match well with the experiment and is propagating away with similar magnitude and velocity.

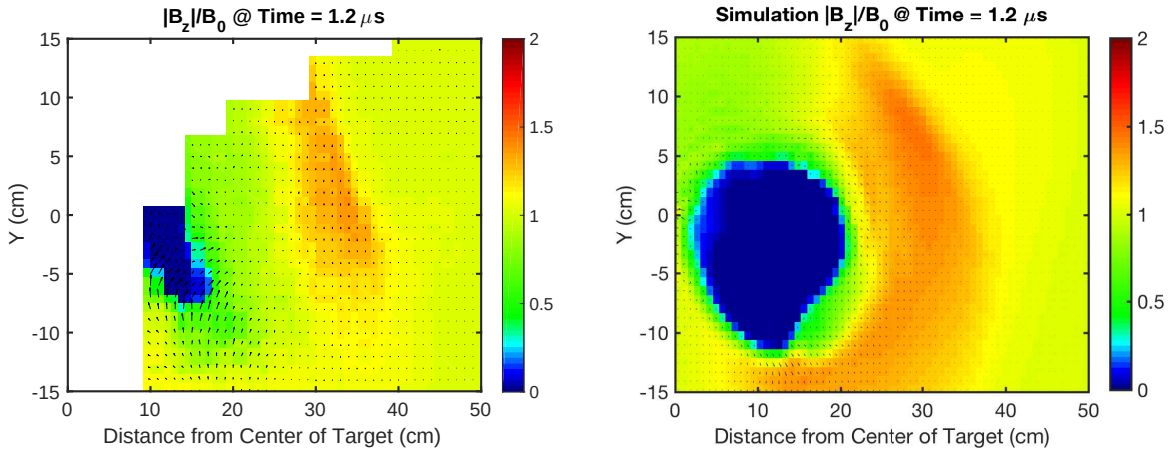

(a) (b)

Figure 5.5: Shows (a) measured experimental B_z in an X-Y oriented plane at $t = 1.2\mu$s, with arrows over-plotted to show direction and magnitude of transverse B field, and (b) the corresponding output from fHybrid3D.

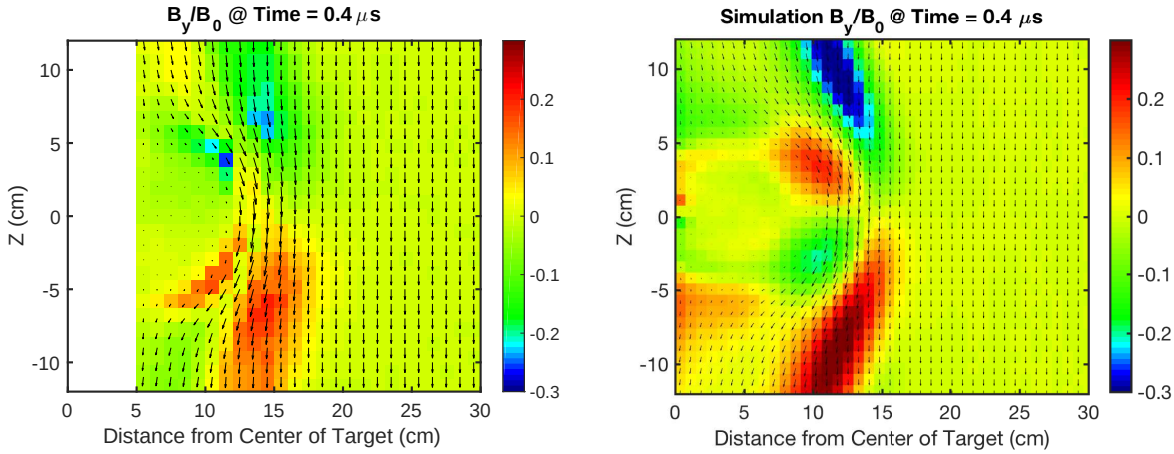

(a) (b)

Figure 5.6: Shows (a) measured experimental B_y in an X-Z oriented plane at $t = 0.4\mu$s, with arrows over-plotted to show direction and magnitude of transverse B field, and (b) the corresponding output from fHybrid3D.

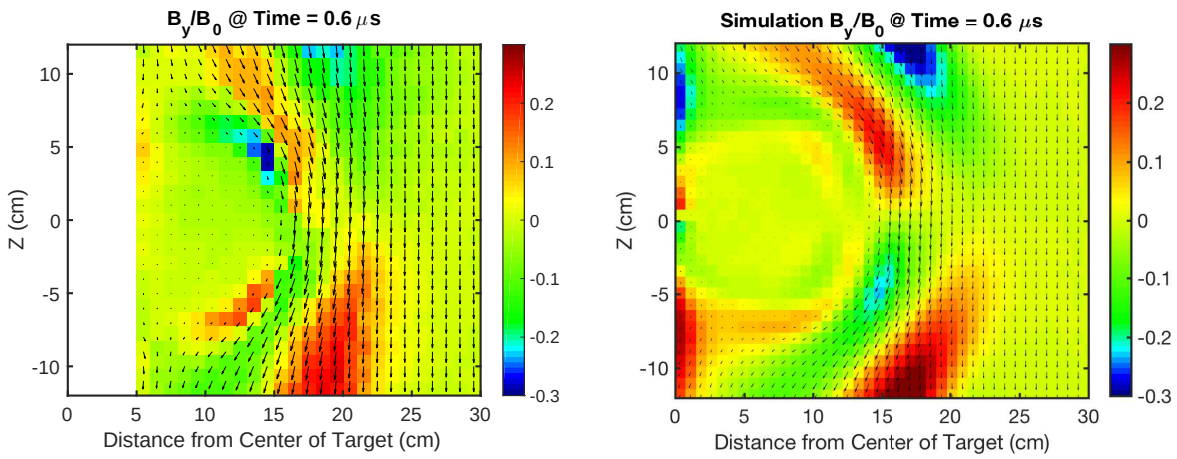

(a) (b)

Figure 5.7: Shows (a) measured experimental B_y in an X-Z oriented plane at $t = 0.6\mu$s, with arrows over-plotted to show direction and magnitude of transverse B field, and (b) the corresponding output from fHybrid3D.

In the Peening campaign, X-Z planes were taken as well to give a feel for what the expansion looks like in three-dimensions. They were taken in front of the target at $y = 0$ from 5 cm away to 30 cm away from the target, extending ± 12 cm along the $\hat{\mathbf{z}}$-axis, with 1 cm spacing between measurements. Figure 5.6 shows a similar plot used in the X-Y planes, but in this case the colored portion corresponds to B_y, and the black arrows represent the magnetic field direction and magnitude in the transverse dimensions. The leading edge of the pulse gives rise to large shear fields that propagate down the magnetic field. The diamagnetic cavity appears to have a similar shape and extent in the X-Z plane as shown by the black vectors. The experimental B_y is near zero inside of the cavity, and outside of the cavity it has a quadrapole structure. The simulation accentuates the quadrapole structure outside of the cavity

Figure 5.7 shows a similar picture, though later in time. The quadrapole fields near the edge of the cavity match better between simulation and experiment at this time. The cavity expansion still looks spherical in both simulation and experiment during this time when the cavity is still expanding rapidly and the coupling is occurring.

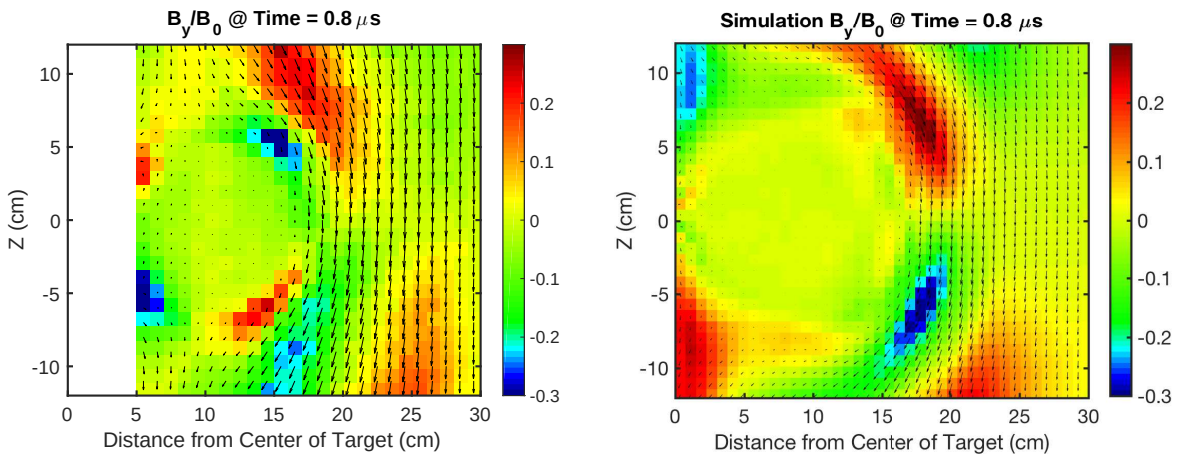

(a) (b)

Figure 5.8: Shows (a) measured experimental B_y in an X-Z oriented plane at $t = 0.8\mu$s, with arrows over-plotted to show direction and magnitude of transverse B field, and (b) the corresponding output from fHybrid3D.

Figure 5.8 shows the fields at the point that the cavity edge is slowing down. The shear fields match in magnitude and general shape very well at the edge of the bubble. The magnetic fields inside of the cavity look to be larger in the experiment. The bubble looks to be diffusing inward faster in the experiment than in the simulation.

Figure 5.9 shows the fields at late time after the bubble has stopped expanding and the pulse is separating from the cavity edge. The shear fields associated with the outward propagating wave match well, however in the experiment there are some shear fields being generated near the target, which most likely has to do with slower ions moving away from the target that act differently than the warm cloud that is used to approximate them. The warm cloud used as an approximation to the rest of the charge states and distributions that come off of the target serves a few purposes, as it maintains a non-zero density inside of the diamagnetic cavity and allows for a return current to come back to the target and fully expel the diamagnetic cavity. This replicates the bubble expansion and collapse from near the target side well, but is not exactly representative of what comes from the target. A full simulation containing all charge states could be run after measuring the the debris

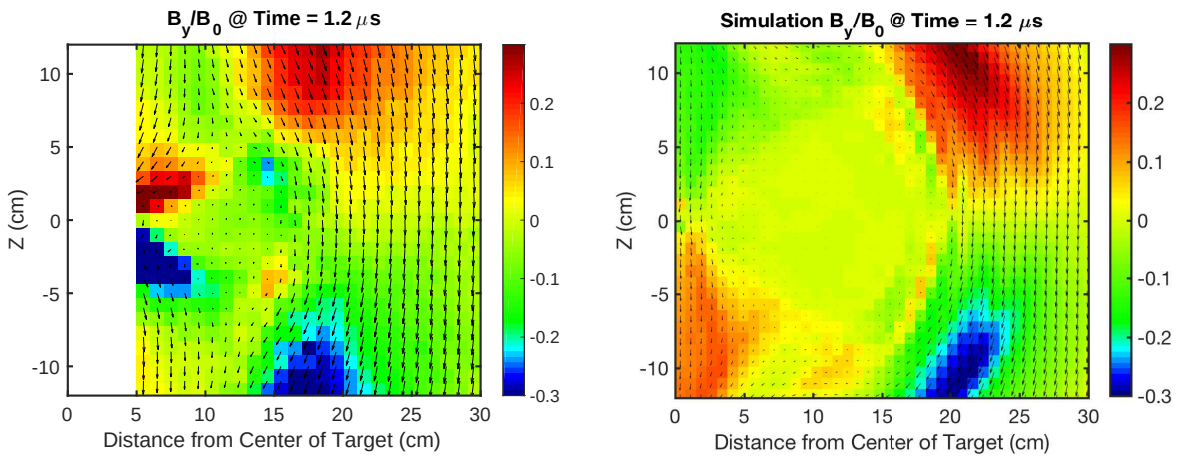

(a) (b)

Figure 5.9: Shows (a) measured experimental B_y in an X-Z oriented plane at $t = 1.2\mu$s, with arrows over-plotted to show direction and magnitude of transverse B field, and (b) the corresponding output from fHybrid3D.

distributions with a Thomson parabola, which would most likely fully reproduce the fields near to the target, that do not participate in coupling energy to the ambient plasma.

5.3 Electrostatic Potential Comparison

The electrostatic potential structure in the experiment, measured by the emissive probe, will be examined in this section. The simulation output, which is in electric and magnetic fields, is post-processed to transform it to electrostatic potential. This can be done in the Coulomb gauge, where $\nabla \cdot \mathbf{A} = 0$, starting from the electric field expressed as electrostatic and magnetic potentials:

$$\mathbf{E} = -\nabla\phi - \frac{1}{c}\frac{\partial \mathbf{A}}{\partial t}\,, \tag{5.1}$$

where ϕ is the electrostatic potential. Taking the divergence of Equation (5.1) and dropping the latter term yields:

$$\nabla^2\phi = -\nabla \cdot \mathbf{E}\,. \tag{5.2}$$

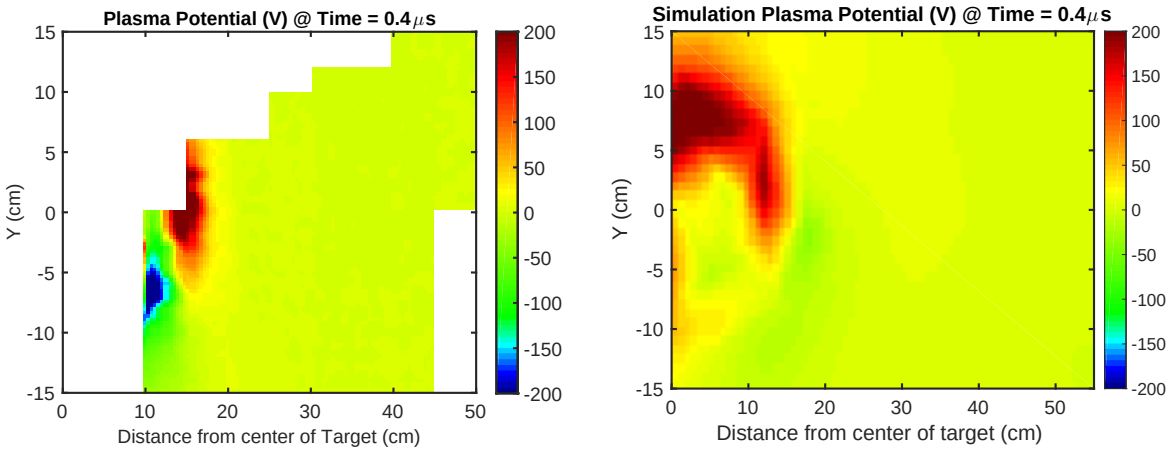

(a) (b)

Figure 5.10: Shows (a) measured experimental ϕ in an X-Y oriented plane at $t = 0.4\mu$s and (b) the corresponding output from fHybrid3D.

The term on the right $(-\nabla \cdot \mathbf{E})$ is easily computed using a finite differencing scheme. In this case the divergence function in MATLAB was used to calculate the source term. The source term is then run through MATLAB's PDE solver, which is implemented by a fast finite element method solver, to compute the electrostatic potential assuming homogeneous, Dirichlet boundary conditions. These are suitable boundary conditions so long as the edge of the simulation domain is far enough away from the simulated ablation.

Figure 5.10 shows the measured and calculated simulation potentials early in time when the strongest fields are present to couple energy and momentum to the ambient ions. Comparing the portions that have been measured outside of the Peening beam path gives a potential structure that has a similar magnitude and extent to that of the experiment. Since the electrostatic component of the electric field is the negative gradient of the potential, the radial electric fields due to the pressure model can be compared via the electrostatic potential. The measured experimental potential is reasonable as it leads to a radial electric field that points outward at the outer edge of the pulse and inward at the inner edge of the pulse. The maximum value of the potential in both cases is ~ 200 V.

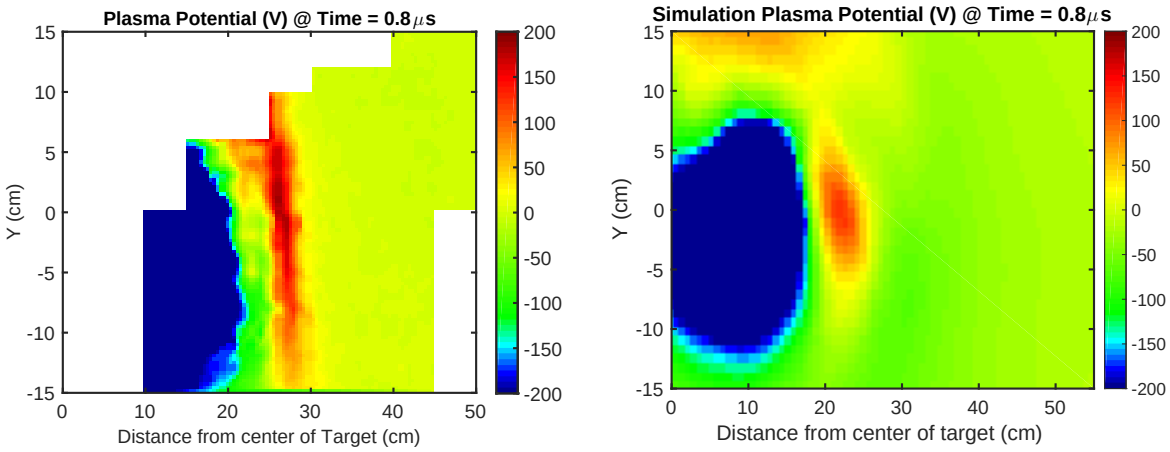

(a) (b)

Figure 5.11: Shows (a) measured experimental ϕ in an X-Y oriented plane at $t = 0.8\mu$s and (b) the corresponding output from fHybrid3D.

At a later time, Figure 5.11 shows a potential structure that is somewhat more diffuse than that which is measured, however is still has a similar shape and magnitude to the measured values.

Figure 5.12 shows the pulse, at $t = 1.2\mu$s, as it is moving upwards and peeling away from the cavity. The general shape, direction of propagation and magnitude are all on the same order of magnitude. The potential is consistent with the cavity moving down and the ions gyrating upward in the figure.

Figure 5.13 shows an in between time (t=0.6 μs) where coupling is still important, but not as early as the X-Y planes at 0.4 μs. This was due to mounting the probe on a different probe drive, which could not push the probe in as far. Due to the physical constraint, it could only get as close as 15 cm away from the target. The ablation did not yet get to the point where the structure could be measured early in time. At 0.6 μs the experiment shows a narrower and sharper gradient which would lead to stronger fields, but again the shape and magnitude match fairly well for using such a simple electron pressure model instead of having to follow the electron dynamics.

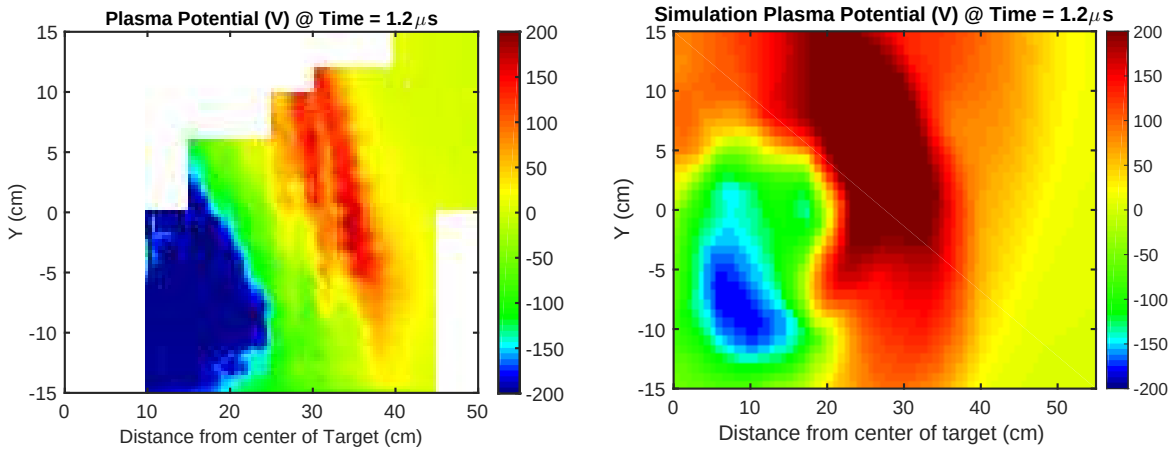

(a) (b)

Figure 5.12: Shows (a) measured experimental ϕ in an X-Y oriented plane at $t = 1.2\mu$s and (b) the corresponding output from fHybrid3D.

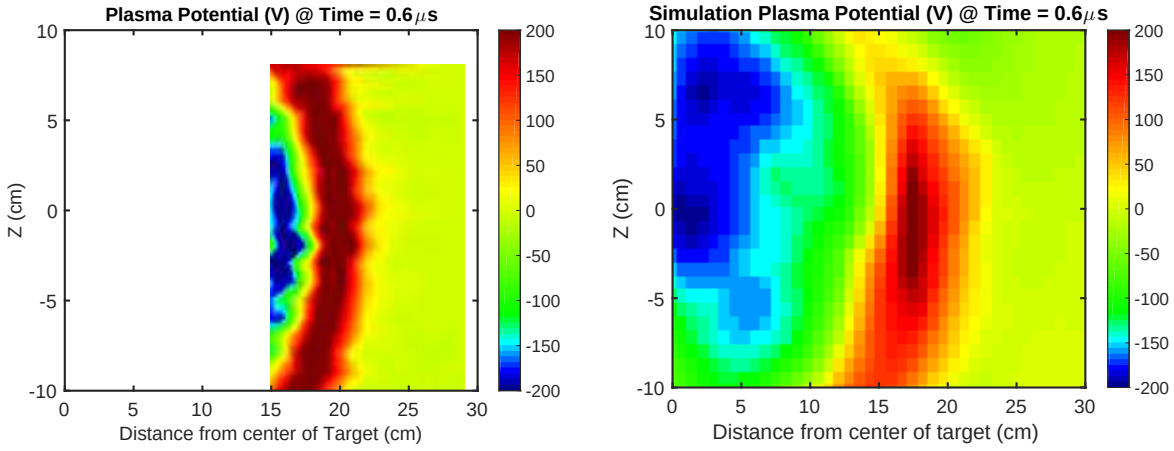

(a) (b)

Figure 5.13: Shows (a) measured experimental ϕ in an X-Z oriented plane at $t = 0.6\mu$s and (b) the corresponding output from fHybrid3D.

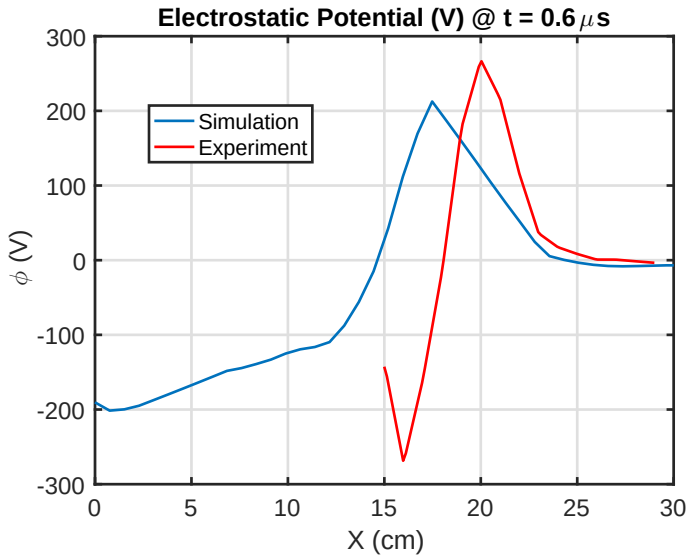

Figure 5.14: Shows a comparison of the simulation and experimental potential data along the blow-off axis.

Figure 5.14 shows a line-out of the experimental and simulation data along the blow-off axis. In this figure it is seen that the magnitude of the experimental data is higher, and the cavity is more fully expelled to a larger radius in the experimental data. The simulation data has a broader peak that is a bit lower. The slopes of the line, which correspond to the magnitude of the electric field are steeper in the experimental data. The simulation and experiment both have a similar shape and will produce a radial electric field that points outward at the outside part of the compression, while pointing inward at the back edge of the pulse.

Figure 5.15 shows the potentials at a slightly later time, showing similar diffusivity in the width of the potential spike associated with the front of the compression.

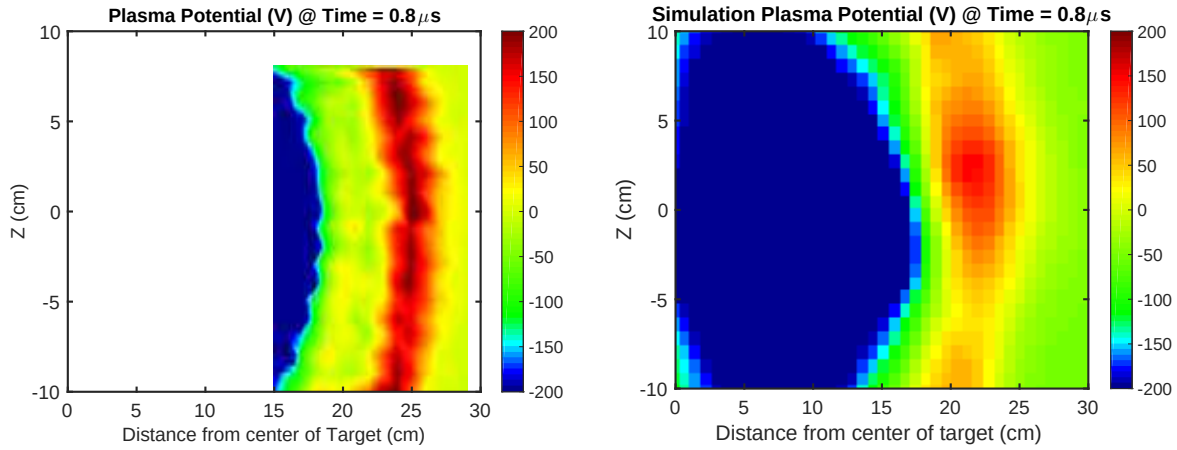

(a) (b)

Figure 5.15: Shows (a) measured experimental ϕ in an X-Z oriented plane at $t = 0.8\mu$s and (b) the corresponding output from fHybrid3D.

5.4 Conclusions

This is the first time electrostatic measurements have been compared to the hybrid model using a very simple isotropic electron pressure model. The magnetic field structure matches quite well, though could be improved by measuring the spatial ion distributions that come off of the target given our experimental laser conditions. The coupling physics tends to be dominated by the azimuthal Larmor field associated with the ablation ion current. The electron pressure model looks to reproduce the electrostatic potential measured by the emissive probe in broad strokes. The model could be improved, but seems to work reasonably well in the case of simulating collisionless shocks and strong magnetosonic waves that propagate across the magnetic field. The question of whether or not the pressure model works well enough for parallel shocks and waves remains open though, as the data used to compare to simulation has been collected is very near to the initial ablation. Fields down the machine in future experiments could be used to benchmark the hybrid simulation methodology for Alfvén waves that propagate along the machine. This however would require significant work and is outside of the scope of this dissertation.

Chapter 6

Conclusions

In this computational dissertation, a hybrid algorithm in which the ions are treated kinetically using Particle-In-Cell (PIC) techniques and the electrons are treated as a charge-neutralizing massless fluid has been used to plan experiments and help analyze experimental results. In turn, recent experimental results have been used to benchmark the hybrid code and validate the use of a simple isotropic electron pressure model.

Laboratory collisionless shock experiments based at UCLA are underway in which it is being attempted to ultimately generate a super-critical perpendicular shock, as well as parallel shocks in the LAPD. Over the past few years much work has gone on at UCLA to improve the laboratory capabilities. It has been shown that a $\mathcal{M}_A \sim 2.5$ shock has been launched in the LAPD using the kJ-class Raptor laser. In the 2013 experimental campaign, the Raptor laser could attain on target energies of ~ 200 J. With this laser energy output along with the LaB_6 cathode upgrade at the north end of the LAPD, the group was able to generate favorable plasma conditions, with a high enough ambient density in which a shock was generated.

The success of the shock campaign was in part due to simulation studies performed

at UCLA initially using a 2D hybrid code provided by Dan Winske at Los Alamos National Laboratory. It provided insight into the collisionless coupling physics that occur during these laser ablation experiments. The initial parameter study had a simplified geometry where the ambient plasma is uniform and the debris explosion is cylindrical. This allowed us to connect simulation results to previous analytical hybrid solutions as well as understand the relevant parameters needed to be experimentally modified. The parameter study guided us in finding the sweet spot for generating shocks, that is that the laser spot size should be defocused to ablate more mass at a slower velocity, and to have a lower magnetic field to allow for higher Mach number shocks given a slower debris piston (see Fig. 3.5). We learned that it is easy to ablate particles too fast so that they are not coupled to the magnetic field on the scales that fit into the LAPD. This was important to realize that the parameter space for generating a shock is small and the conditions need to be just right, though the hybrid simulations relaxed the coupling parameter compared to previous analysis[1]. Given higher densities and ablation energies, the parameter space opens up a bit and makes it easier to couple energy to the ambient plasma to generate a shock-wave. These 2D computational studies also made it apparent that there is a single driving species that acts as the piston, the faster species just stream out and gyrate through the magnetic field with little interaction, and the slower species free-stream in the diamagnetic cavity, which does not contribute to coupling of energy to the ambient ions during the time-scale of the shock formation (see Figs. 3.6 and 3.7).

Another question arose throughout early experiments, and that was due to the size of the LaB_6 cathode being smaller than the the BaO cathode, This led to an inhomogeneous plasma density profile. A simulation study was performed to determine the effect of having a debris piston running over a density gradient during the critical coupling time in the experiment. It was shown that running up a density gradient actually increases the coupling fields (see Fig. 3.10) experienced by the ions in the more dense region and boosts the acceleration of ambient ions (see Fig. 3.11). This result demonstrates nicely that the non-uniform density actually aids in collisionless coupling and ultimately leads

to a stronger shock.

After the collisionless shock campaign, a massively parallel three-dimensional hybrid code was developed. This took some time to debug and get the parallelization running effectively. Computational resources were awarded by XSEDE to run 3D hybrid simulations after submitting a proposal that showed preliminary results from the 3D code. The code output has been compared to a slightly different 3D hybrid code developed at Lawrence Livermore National Laboratory that uses a slightly different predictor-corrector algorithm. The results agreed quite well, so some research went into finding a good approximation to the laser debris distribution (see Fig. 4.2b). The results from simulating the debris cloud using the more realistic velocity distributions agreed quite well with experiment (see Fig. 4.5a).

The 2D code and 3D code were run on similar problems that are normalized to have roughly the same energy, which expel the magnetic field out to a particular cavity size. Due to the differences in geometry it was shown that the 2D code tends to overestimate shock coupling and the strength of the outgoing magnetosonic shock wave when compared to the 3D code (see Figs. 4.5 and 4.8) due to the expansion geometry. Particles in 3D can stream down the magnetic field and not participate in coupling at all, but drive electromagnetic instabilities instead.

The 3D code was then applied to modeling the Peening experimental campaign. The amount of data that could be experimentally gathered and compared to simulation would be much greater. In conjunction with magnetic field measurements, electrostatic potential could be measured, which represents the physical electric fields in the experiment. Due to the coarse spacing of the measurements it was difficult to convert the potential into electric fields with much accuracy, since the signals were a bit noisy and the numerical differentiation increased the noise. This led to solving for the electrostatic potential from the simulation using a 3D Poisson solver that recently has been released in MATLAB. The potential structure that came from this numerical PDE solution match

the experimental results quite well. It was shown that the isotropic, adiabatic electron model works for these laboratory experiments, as it also agrees well with space based data that measured electron heating across the Earth's bow shock. The electric and magnetic field structures that couple energy to the ambient ions is modeled accurately and is benchmarked against real data. This gives users of the hybrid code a boost in confidence when using it to analyze perpendicular shock experiments and collisionless coupling.

It still remains to be seen if the model works well enough for parallel shock geometries in the LAPD. It could be that the pressure tensor needs to be anisotropic along the magnetic field to correctly model parallel shock geometries. These questions are out of the scope of this dissertation, and will be left for the next student to take over the UCLA 3D hybrid code fHybrid3D.

Appendix A

Description of Hybrid Algorithm

The simulation software being used is a three-dimensional magnetostatic hybrid code, which treats the ions kinetically using the particle-in-cell method, and the electrons are treated as an inertialess charge neutralizing fluid. The following sections will discuss each of these approximations and show the relevant equations used in the code. First, the code units and normalizations will be discussed.

A.1 Code Units and Normalization

The simulation code operates using dimensionless parameters, which are listed in Table A.1. In Table A.1, the values with a naught subscript represent the reference values chosen for the simulation. These are typically chosen to be the mass and density of a uniform and ambient plasma species, but the choice is arbitrary. The plasma frequency (ω_{pi}) and cyclotron frequency (ω_{ci}) used in the normalizations are calculated using the reference parameters (m_0, n_0, B_0, Z_0), where Z_0 is the charge number of the reference species. It should be noted that the input and output velocities are relative to the Alfvén

Time	$\tilde{t} = t\omega_{pi}$
Space	$\tilde{\mathbf{x}} = \frac{\mathbf{x}}{c/\omega_{pi}}$
Velocity	$\tilde{\mathbf{v}} = \frac{\mathbf{v}}{c}$
Temperature (Energy)	$\tilde{T} = \frac{k_B T}{m_0 c^2}$
Electric Field	$\tilde{\mathbf{E}} = \frac{\mathbf{E}}{B_0}\frac{\omega_{ci}}{\omega_{pi}}$
Magnetic Field	$\tilde{\mathbf{B}} = \frac{\mathbf{B}}{B_0}\frac{\omega_{ci}}{\omega_{pi}}$
Density	$\tilde{n} = \frac{n}{n_0}$
Scalar Resistivity	$\tilde{\eta} = \frac{\omega_{pi}\eta}{4\pi}$
Scalar Electron Pressure	$\tilde{p_e} = \frac{p_e}{n_0 m_0 c^2}$

Table A.1: Internal code normalizations used in fHybrid3D.

velocity ($\tilde{\mathbf{v}} = \frac{\mathbf{v}}{v_a}$), and the time is measured relative to the inverse ion gyro-frequency ($\tilde{t} = t\omega_{ci}$), but are translated into the aforementioned dimensionless units within the code.

A.2 Grids and Macro-Particles

The simulation domain consists of 2 staggered three-dimensional Cartesian grids. The main grid is set up such that the grid points straddle the domain edges, meaning that the origin of the coordinate system resides between the first and second grid vertex in each dimension. Most values in the simulation are saved at the cell centers of the main grid. The magnetic field is then solved on an offset grid , where the vertices of the main grid represent where its data is stored. The macro-particles in this simulation have a cuboid shape with an extent that is equal to the cell size. These macro-particles represent a group of particles spread uniformly throughout the cuboid.

A.3 Model Equations

Now that the code normalizations are chosen, the grids have been determined, and the particle shape and extent has been specified, one needs to specify the model equations that are to be solved. In this case, the first set of equations to examine are Maxwell's equations:

$$\begin{aligned} \nabla \cdot \mathbf{E} &= \cancelto{0}{4\pi\rho} & \nabla \cdot \mathbf{B} &= 0 \\ \nabla \times \mathbf{E} &= -\tfrac{1}{c}\tfrac{\partial \mathbf{B}}{\partial t} & \nabla \times \mathbf{B} &= \tfrac{4\pi}{c}\mathbf{J} + \cancelto{0}{\tfrac{1}{c}\tfrac{\partial \mathbf{E}}{\partial t}} \end{aligned} , \tag{A.1}$$

where we are assuming charge quasi-neutrality, and neglecting the displacement current (magnetostatic approximation). In conjunction with Maxwell's equations, we need the electron momentum equation in the inertia-less limit:

$$\cancel{m_e n_e \frac{D\bar{\mathbf{v}}_\mathbf{e}}{Dt}}^{\,0} = -en_e(\mathbf{E} + \frac{1}{c}\bar{\mathbf{v}}_\mathbf{e} \times \mathbf{B}) + en_e \overleftrightarrow{R} \cdot \mathbf{J} - \nabla \cdot \overleftrightarrow{P_e} \,, \tag{A.2}$$

where $\overleftrightarrow{R}$ is the resistivity tensor and $\overleftrightarrow{P_e}$ is the electron pressure tensor. These equations are then coupled to the ion equations of motion for each species, denoted by α:

$$\frac{dv_m}{dt} = \frac{Z_\alpha e}{m_\alpha}(\mathbf{E} + \frac{1}{c}\mathbf{v_m} \times \mathbf{B}) - \frac{Z_\alpha e}{m_\alpha}\overleftrightarrow{R} \cdot \mathbf{J} \,, \tag{A.3}$$

where this equation is used to update the velocity of each macro-particle, denoted by m. This updated velocity is then used to advance the position of each particle. In each of these cases the current can be written explicitly as:

$$\mathbf{J} = -en_e\bar{\mathbf{v}}_\mathbf{e} + e\sum_\alpha Z_\alpha n_\alpha \bar{\mathbf{v}}_\alpha \,. \tag{A.4}$$

Using the normalizations given in Table A.1, one can rewrite each equation using dimensionless parameters. Maxwell's equations become:

$$\begin{aligned} \tilde{\nabla} \cdot \tilde{\mathbf{E}} &= 0 & \tilde{\nabla} \cdot \tilde{\mathbf{B}} &= 0 \\ \tilde{\nabla} \times \tilde{\mathbf{E}} &= -\tfrac{\partial \tilde{\mathbf{B}}}{\partial \tilde{t}} & \tilde{\nabla} \times \tilde{\mathbf{B}} &= \tilde{\mathbf{J}} \,. \end{aligned} \tag{A.5}$$

Starting from Equation (A.2), assuming quasi-neutrality, isotropic plasma resistivity ($\overleftrightarrow{R} \rightarrow \eta$) and electron pressure ($\overleftrightarrow{P_e} \rightarrow p_e$), one can recast the equation in terms of dimensionless parameters, solve for $\tilde{\mathbf{E}}$, eliminate $\tilde{\bar{\mathbf{v}}}_{\mathbf{e}}$ using a normalized version of Equation (A.4), and finally eliminate $\tilde{\mathbf{J}}$ using the dimensionless version of Ampere's law in Equation (A.5), one obtains:

$$\tilde{\mathbf{E}} = \frac{(\tilde{\nabla} \times \tilde{\mathbf{B}}) \times \tilde{\mathbf{B}} - (\sum_\alpha Z_\alpha \tilde{n}_\alpha \tilde{\bar{\mathbf{v}}}_\alpha) \times \tilde{\mathbf{B}} - \tilde{\nabla} \tilde{p}_e}{\sum_\alpha Z_\alpha \tilde{n}_\alpha} + \tilde{\eta} \tilde{\nabla} \times \tilde{\mathbf{B}} \,. \tag{A.6}$$

The normalized equations of motion for each macro particle become:

$$\frac{\mathrm{d}\tilde{\mathbf{v}}_{\mathbf{m}}}{\mathrm{d}\tilde{t}} = \frac{Z_\alpha}{\tilde{m}_\alpha} [(\tilde{\mathbf{E}} + \tilde{\mathbf{v}}_{\mathbf{m}} \times \tilde{\mathbf{B}}) - \tilde{\eta} \tilde{\nabla} \times \tilde{\mathbf{B}}] \,. \tag{A.7}$$

Finally, there is a need to close the electron momentum equation with an expression for the electron pressure. We use this equation for the electron pressure:

$$\tilde{p}_e = \tilde{T}_{e0} (\sum_\alpha Z_\alpha \tilde{n}_\alpha)^\gamma \,, \tag{A.8}$$

where $\gamma = 5/3$ is typically the value used and $\tilde{T}_{e0}$ is a reference temperature used for the calculation, which represents the temperature of the electron fluid given its density is equal to the reference density n_0.

The model equations presented in this section are similar to those used in a fully kinetic PIC code, but they are easier to solve since the electric field is calculated using the electron momentum equation (Equation (A.6)). In contrast to a full PIC code, where $\mathbf{E}$ and $\mathbf{B}$ are both explicitly advanced in time and special attention is required to keep $\nabla \cdot \mathbf{J} = 0$, the hybrid model does not explicitly advance $\mathbf{E}$ and $\nabla \cdot \mathbf{J} = 0$ is satisfied automatically.

A.4 Computational Algorithm

Now that the model equations have been written down the algorithm must be discussed. In this section, it is assumed that all equations being used are the dimensionless

versions and the tilde notation will be dropped for symbolic simplicity. Typically the number of macro-particles used in a simulation is about 100 particles per cell. The positions and velocities of the macro-particles are initialized for each plasma species of interest. The magnetic field is usually initialized as a uniform field pointing in the $\hat{z}$ direction. The mean velocity ($\bar{v}_\alpha$) and density (n_α) for each ion species are collected on a grid. The electric field is then calculated using a discretized version of Equation (A.6). After initialization, the algorithm proceeds assuming that $\mathbf{E}$, $\mathbf{B}$, and n_α are know for each species α at a timestep n. The ion velocity moments $\bar{v}_\alpha$ are know at timestep $n - 1/2$.

1. Broadcast $\mathbf{E}^n$, $\mathbf{B}^n$, and $\eta(\nabla \times \mathbf{B}^n)$ to each compute node.

2. The macro-particle velocities are advanced using a second order centered difference scheme to discretize the time derivative in Equation (A.7).

$$\mathbf{v_m}^{n+1/2} = \mathbf{v_m}^{n-1/2} + \frac{Z_\alpha \Delta t}{m_\alpha}[(\mathbf{E} + \mathbf{v_m} \times \mathbf{B}) - \eta \nabla \times \mathbf{B}]^n \,. \tag{A.9}$$

   Since $\mathbf{v_m}$ is only known on the half time steps, it must be expanded as an average value[54]. After substituting $\mathbf{v_m}^n = \frac{1}{2}(\mathbf{v_m}^{n+1/2} + \mathbf{v_m}^{n-1/2})$ into Equation (A.9) and solving for $\mathbf{v_m}^{n+1/2}$, the velocity advance equation, after some manipulation, can be written as:

$$\mathbf{v_m}^{n+1/2} = \mathbf{V_0} + \frac{h}{2}\mathbf{E}' + \frac{fh}{2}\mathbf{P_0} \times \mathbf{B}^n + \mathcal{O}(h^3) \,, \tag{A.10}$$

   where

$$\begin{aligned} \mathbf{V_0} &= \mathbf{v_m}^{n-1/2} + \tfrac{h}{2}\mathbf{E}' \\ \mathbf{P_0} &= \mathbf{V_0} + \tfrac{h}{2}\mathbf{V_0} \times \mathbf{B}^n \\ \mathbf{E}' &= \mathbf{E}^n - \eta(\nabla \times \mathbf{B}^n) \\ f = \tfrac{2}{1+(\frac{h}{2})^2|\mathbf{B}^n|^2} \,, h &= \tfrac{Z_\alpha \Delta t}{m_\alpha} \,. \end{aligned} \tag{A.11}$$

3. Now that the velocities have been advanced, the positions are then advanced using a leapfrog scheme:

$$\mathbf{x_m}^{n+1} = \mathbf{x_m}^n + \Delta t \mathbf{v_m}^{n+1/2} \,. \tag{A.12}$$

4. Calculate density (n_α^{n+1}) and velocity ($\bar{\mathbf{v}}_\alpha^{n+1/2}$) moments for each ion species from the macro-particles on each compute node. Perform an MPI reduction to sum the moments on the main node.

5. The magnetic field is then advanced using a fourth order Runge-Kutta (RK) integration scheme to integrate Faraday's Law in Equation (A.5). Since the integration does not converge for larger values of Δt, it must be integrated iteratively using a smaller timestep. This smaller timestep will be defined as $\Delta t' \equiv \Delta t/\theta$, where θ is a positive integer that determines how many integration cycles are required to advance $\mathbf{B}^n$ to $\mathbf{B}^{n+1}$. Each sub-cycle of the RK integration proceeds as follows:

$$\mathbf{B}^{n'+1/\theta} = \mathbf{B}^{n'} + \frac{\Delta t'}{6}(\mathbf{K_1}^{n'} + 2\mathbf{K_2}^{n'} + 2\mathbf{K_3}^{n'} + \mathbf{K_4}^{n'})\,, \tag{A.13}$$

where the RK coefficients are given by:

$$\begin{aligned} \mathbf{K_1}^{n'} &= -\nabla \times \mathbf{F}(\mathbf{B}^{n'})\,, \\ \mathbf{K_2}^{n'} &= -\nabla \times \mathbf{F}(\mathbf{B}^{n'} + \tfrac{\Delta t}{2}\mathbf{K_1}^{n'})\,, \\ \mathbf{K_3}^{n'} &= -\nabla \times \mathbf{F}(\mathbf{B}^{n'} + \tfrac{\Delta t}{2}\mathbf{K_2}^{n'})\,, \\ \mathbf{K_4}^{n'} &= -\nabla \times \mathbf{F}(\mathbf{B}^{n'} + \Delta t\mathbf{K_3}^{n'})\,, \end{aligned} \tag{A.14}$$

and $\mathbf{F}(\mathbf{B^{n'}})$ is the electric field given in Equation (A.6) evaluated at mixed time intervals:

$$\mathbf{F}(\mathbf{B}^{n'}) = \frac{(\nabla \times \mathbf{B}^{n'}) \times \mathbf{B}^{n'} - (\sum_\alpha Z_\alpha n_\alpha \bar{\mathbf{v}}_\alpha)^{n+1/2} \times \mathbf{B}^{n'} - \nabla p_e^{n+1/2}}{(\sum_\alpha Z_\alpha n_\alpha)^{n+1/2}} + \eta \nabla \times \mathbf{B}^{n'}\,. \tag{A.15}$$

where the ion density $n_\alpha^{n+1/2} = \frac{1}{2}(n_\alpha^n + n_\alpha^{n+1})$. The timestep n' is initially set to n and iterates until $n' + 1/\theta = n + 1$.

6. Now that $\mathbf{B}^{n+1}$ has been calculated, the only piece missing to calculate $\mathbf{E}^{n+1}$ is $(\bar{\mathbf{v}}_\alpha)^{n+1}$. This is estimated by extrapolation, other methods use a predictor-corrector scheme[55]. If we define:

$$\mathbf{U}^n \equiv \sum_\alpha Z_\alpha n_\alpha^n \bar{\mathbf{v}}_\alpha^{n-1/2} / \sum_\alpha Z_\alpha n_\alpha^n\,, \tag{A.16}$$

then $\mathbf{U}^{n+1}$ can be estimated as:

$$\mathbf{U}^{n+1} = \frac{3}{2}\mathbf{U}^{n+1/2} - \frac{1}{2}\mathbf{U}^{n-1/2}\,. \tag{A.17}$$

7. The electric field can now be advanced by calculating Equation (A.6) with the extrapolated ion mean velocity:

$$\mathbf{E}^{n+1} = \frac{(\nabla \times \mathbf{B}^{n+1}) \times \mathbf{B}^{n+1} - \nabla p_e^{n+1}}{(\sum_\alpha Z_\alpha n_\alpha)^{n+1}} - \mathbf{U}^{n+1} \times \mathbf{B}^{n+1} + \eta \nabla \times \mathbf{B}^{n+1}\,. \tag{A.18}$$

A.5 Code Stability Constraints

The code runs with a large timestep compared to that of a full PIC simulation, but the timestep is still constrained since the hybrid algorithm is an explicit method for advancing the fields and particle data. The first constraint is the Courant-Friedrichs-Lewy (CFL) condition, which is a particle velocity constraint where a particle can not move more than one half of a cell size in a given timestep. This can be expressed as:

$$v_{\text{fast}}\Delta t \leq \frac{\text{Min}(\Delta x, \Delta y, \Delta z)}{2}\,, \tag{A.19}$$

where v_{fast} is the velocity of the fastest particle in a given timestep. If setting a global timestep that does not change, one must anticipate how fast particles may be accelerated and set an appropriate timestep before starting the simulation to temporally resolve particle motions across cell boundaries. In code normalized units, this condition can be expressed as:

$$\tilde{\Delta} t \leq \frac{\text{Min}(\tilde{\Delta} x, \tilde{\Delta} y, \tilde{\Delta} z)}{2\mathcal{M}_{\text{fast}}}\,, \tag{A.20}$$

where $\mathcal{M}_{\text{fast}}$ is the fastest Mach number a particle moves in a given simulation.

There also exists a whistler wave constraint[55], which is expressed as:

$$\Delta t \leq \frac{1}{\sqrt{3}\pi}\frac{1}{\omega_{ci}}\Big(\frac{\text{Min}(\Delta x, \Delta y, \Delta z)}{c/\omega_{pi}}\Big)^2\,, \tag{A.21}$$

which can also be written in normalized code units as:

$$\tilde{\Delta t} \leq n_{\tilde{\min}} \frac{\mathrm{Min}(\tilde{\Delta x}, \tilde{\Delta y}, \tilde{\Delta z})^2}{\sqrt{3}\pi}\,, \tag{A.22}$$

where $n_{\tilde{\min}}$ is the fractional density of the lower density plasma regions used in inhomogeneous plasma simulations. In the typical LAPD experimental simulation, there is a high density cylinder surrounded by a lower density plasma, so the lower density region must be whistler stable as well. This constraint in these inhomogeneous simulations becomes dominant over the CFL constraint since the timestep scales with the cell size squared. In normalized units this will normally be a fractional quantity less than unity. This constraint relaxes when looking at much larger phenomena in which the cell sizes are on the order of or larger than the ion inertial length.

A.6 Code Performance and Scaling

The performance of how fHybrid3D scales across nodes was determined by running a test simulation multiple times across a varying number of nodes. The test case was designed to fit into the memory space of a single node and complete within a few hours, but be large enough to break up across nodes to determine scaling performance. Specifically, the grid was set up such that the cell size is $\Delta x \sim \Delta y \sim \Delta z \sim 0.25\ c/\omega_{pi}$, or roughly a quarter of the ambient ion inertial length. The grid size is 120x120x150, which ends up being $\sim$ 2.16 million cells. The domain size in the XY plane is chosen such that it is just larger than the size of the LAPD, which is 1m across, or 10-20 ion inertial lengths depending on the density. There are two species of ions in the code, both with 100 macro-particles per cell. This ends up being roughly a half billion particles that need to be moved each time step. Since most of the computation is due to the motion of macro-particles, the particles are split across the nodes, while the fields are advanced on a single node. This will limit the scaling somewhat, but it will be shown that for the problem size of interest, more cumbersome and complicated parallelization is not required. The rest of

the simulation parameters were chosen to be representative of a typical case that may be simulated, but only for a short time. In this case, 100 time steps were run to minimize the amount of CPU hours used, but still show the scaling performance. The time step $\Delta t\omega_{ci} \sim 0.01$, so the simulations run out to $1\omega_{ci}^{-1}$, or about a sixth of an ambient ion cyclotron period. The background magnetic field is $B_0 \sim 200$ G oriented along the z axis, and the ambient hydrogen ion density is $n_0 \sim 10^{13}$ cm^{-3}. The ambient ions are initialized with an isotropic temperature $T_i \sim 1$ eV, and the electron fluid reference temperature is $T_{e0} \sim 5$ eV. In the center of the domain, a hot blob of carbon V (C^{+4}) is initialized such that it expands out radially at $\mathcal{M}_A \sim 2$, where $\mathcal{M}_A$ is the Alfvénic Mach number.

A.7 Performance on Blacklight

Blacklight is a shared non-uniform memory architecture, or NUMA computer. The machine has several blades which share a single system image where the entire memory space of the machine is addressable on any given node. The simulation code was initially only parallelized with OpenMP. The code was tested and used the methods of process pinning and first touch to attempt to control memory allocation across nodes. It became immediately evident that the code did not scale well across nodes. The test run took almost twice as long to run on two nodes as it did to complete on a single node. The code was then updated to control inter-node communication via MPI. The particle arrays were explicitly set up on separate nodes, and only the fields and particle moments needed to be transmitted back and forth between compute nodes.

Figure A.1a is a curve that shows the wall clock time of the simulation run over a varying number of nodes. The wall clock time is the overall time a given simulation takes to start and run to completion. If there were no overhead associated with adding machines to a given simulation, each doubling of the number of CPUs should half the wall time. The curve shows that the code scales well up 8-16 nodes, or 128-256 processors.

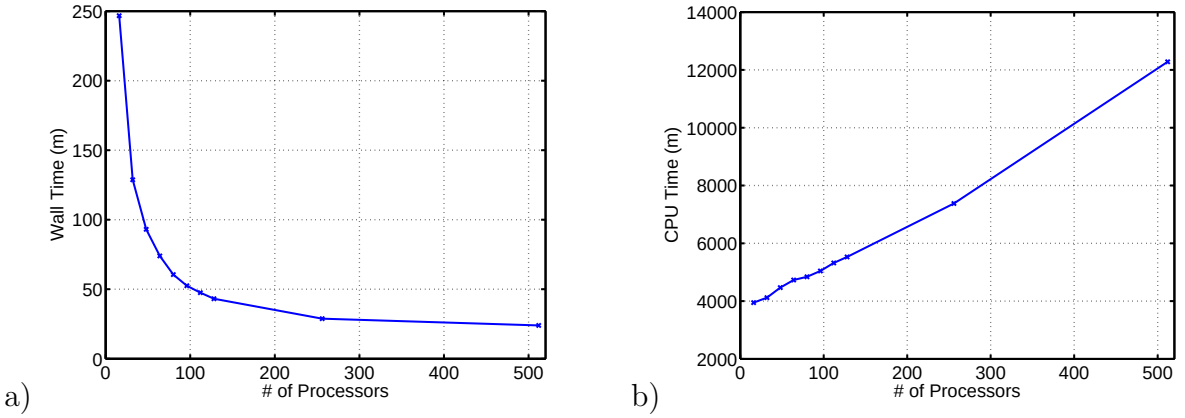

Figure A.1: CPU Time (a) and Wall Time (b) of the test simulation run on Blacklight for a varying number of processors.

Figure A.1b shows the CPU time used for the computations. The CPU time is the overall amount of time spent computing. That is if you spend 1 hour computing on 10 CPUs, the CPU time is 10 hours and the wall time is 1 hour. If scaling is ideal, then the CPU time should not increase when doubling the number of processors. It gives an idea of how much overhead is being spent in communicating between processors. This curve indicates that a CPU hour penalty is paid, but is under 50% when using 128 processors, and $\sim 80\%$ when running on 256 processors. Typical large scale runs should have a smaller CPU hour percentage penalty due to a larger overall number of particles, because of a larger grid and due to running with more than two species. This will increase the ratio of particle moves to field updates, which will better utilize the particle pushing nodes.

A.8 Performance on Gordon

The code is now parallelized with both OpenMP and MPI, so the necessity for using a shared memory architecture has been mitigated. Following the testing on Blacklight, a supplemental allocation for Gordon was requested so that the code could be tested in

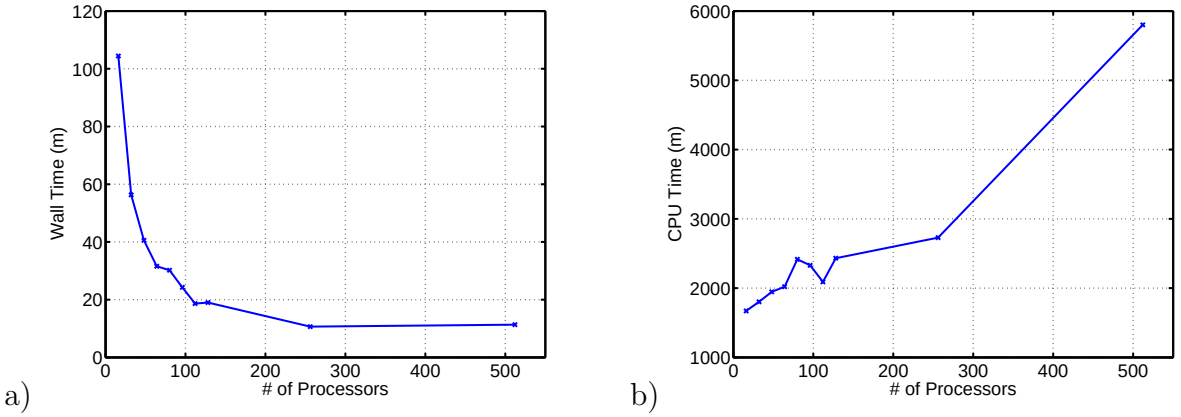

Figure A.2: CPU Time (a) and Wall Time (b) of the test simulation run on Gordon for a varying number of processors.

a standard cluster architecture. The code was compiled for Gordon, and the exact same simulations were run on that machine.

Figure A.2a shows a similar curve to that shown in Figure A.1a, but it should be noted that they do not share the same scale. The same runs on the same number of nodes completed much faster than those on Blacklight. There is some variance on the curve across runs, but we attribute it to different network topologies from run to run. Again, in this case the knee of the curve is around the same place, which is 128-256 processors or 8-16 nodes, though the number of CPU hours on Gordon used is much less. Figure A.2b also shows a similar trend, where the CPU hour penalty paid for runs using less than 32 nodes is under 80%.

A.9 Performance Conclusions

The scaling tests performed indicate that our code is suited for running on a standard cluster architecture like Gordon. The initial idea was that a shared memory computing architecture could be used to simplify the parallelization. Blacklight is one

such architecture that has a single address space that is shared across all nodes. This eliminates having to manually partition data arrays across compute nodes and manually sharing information between compute nodes using MPI. This technique however turned out to be problematic, as control of where memory resides is left up the operating system. This resulted in excessive communication overhead between nodes and the code scaled poorly. The simulations ran much faster on Gordon and scaled to a similar number of processors. Larger, higher resolution runs that represent the target simulation resolution have been completed that run in under 12 hours on 16 nodes. This is roughly 3000 CPU hours for a single run, with 2 species. It is expected to scale linearly with the number of species, as the field solutions do not change size. Thus, in target simulations, where we expect 2-4 species of ions to run (sometimes more), we would place an upper limit of 6000 CPU hours per run. The code scales reasonably well for the problem size of interest, and the computational burden is not too high.

Appendix B

Derivation of Wright Model in Cylindrical Coordinates

This appendix details the calculations that are parallel to Wright's calculations[46], but in cylindrical coordinates to match the simulations performed using the 2D hybrid simulation code. This is a fairly simple model, where the electrons are treated in the ideal MHD limit, and electron pressure as well as resistivity are neglected. These approximations are made to create a tractable solution to be able to gain some insight into the hybrid model being used in the computer simulation, which includes all of these effects.

The model starts out assuming there exists an ambient plasma of uniform density n_i, with a mass m_i, and an ambient magnetic field $\mathbf{B} = B_0\hat{\mathbf{z}}$. Embedded within this ambient plasma are N_d debris ions that exist at the origin each with a mass m_d. It is assumed that the system is quasi-neutral, so obeys the following relation:

$$n_e = Z_d n_d + n_i \,, \tag{B.1}$$

where n_d is the debris density.

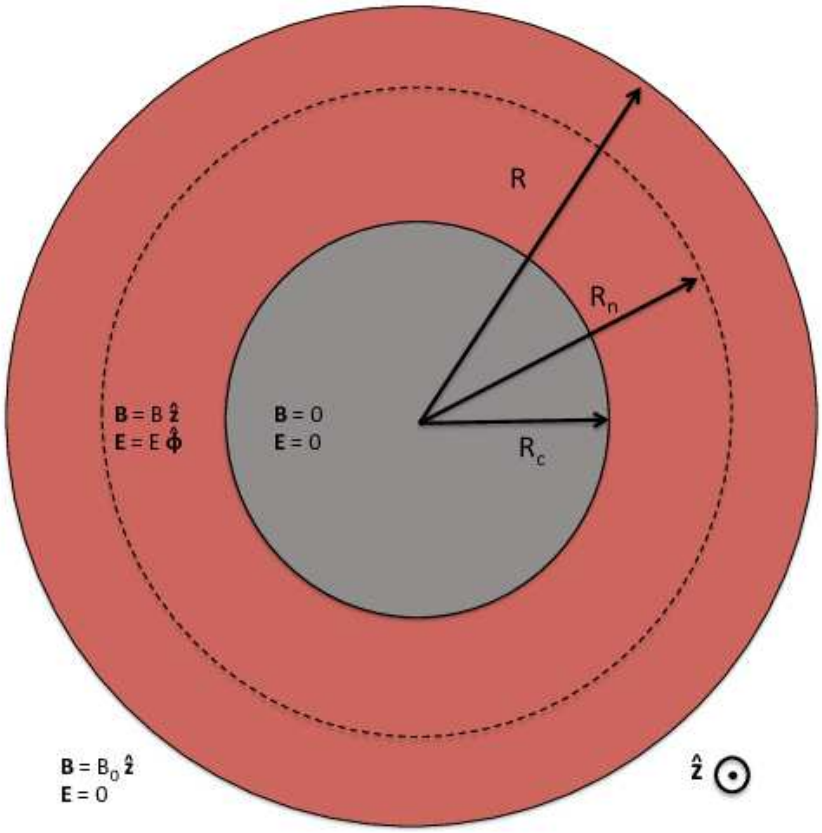

Figure B.1: Shows a cartoon depicting the geometry of the problem, where R is the radius of the debris expansion, R_c is the radius of the diamagnetic cavity, and R_n denotes the radius of an ambient ion density jump, which will be used later in the derivation.

Figure B.1 shows a few of the key radii in the problem. R denotes the radius of the debris expansion, which expands out uniformly and radially from the center at a velocity v_d, at a time $t = R/v_d$. This gives a debris density of:

$$n_d = \frac{N_d}{\pi R^2}\,, \text{for } r < R\,, \quad n_d = 0 \text{ otherwise}\,, \tag{B.2}$$

where N_d represents the total number of debris ions. If we then use the 2D equal mass radius:

$$R_m^2 = \frac{N_d m_d}{\pi n_i m_i}\,, \tag{B.3}$$

in conjunction with equation B.1, we can express the electron density for $r < R$ as:

$$n_e = n_i(1 + Z_d(\frac{m_i}{m_d})(\frac{R_m}{R})^2)\,. \tag{B.4}$$

If we then assume that there exists a fully expelled diamagnetic cavity of radius R_c, where $\mathbf{B} = 0$, and the electrons are ideal MHD, where they are bound to the field lines, then we can assume that the electrons within the cavity are all from the laser debris expansion and have a density of:

$$n_{de} = \frac{N_{de}}{\pi R_c^2} = \frac{Z_d N_d}{\pi R_c^2}\,. \tag{B.5}$$

Now if we invoke quasi-neutrality within the diamagnetic cavity, using:

$$Z_d n_d + n_i = n_{de}\,. \tag{B.6}$$

We can expand and rearrange this after a bit of algebra to get to this dimensionless equation:

$$\frac{R_c}{R} = \left[1 + (\frac{m_d/m_i}{Z_d})(\frac{R}{R_m})^2\right]^{-1/2}\,. \tag{B.7}$$

If we assume $(R/R_m)^2 \ll 1$, or that the expansion is in its early phase, this can be written as the approximation for shell thickness $\Delta R = R - R_c$:

$$\frac{\Delta R}{R} \sim \frac{1}{2}\frac{m_d/m_i}{Z_d}(\frac{R}{R_m})^2\,. \tag{B.8}$$

This gives a width of the region where the magnetic field is compressed and the coupling electric field exists. It extends from the edge of the diamagnetic cavity to the edge of the

debris ion cloud. If we substitute in equation B.3, we can easily see that the shell width is proportional to the ambient ion density ($\Delta R/R \propto n_i$).

There were several approximations involved in describing the shell thickness, which gives us a boundary that can be used to self-consistently solve Maxwell's equations to get an electric and magnetic field within the shell. The first is quasi-neutrality. If we use the normalizations presented in Table A.1, we can write down Gauss' law in dimensionless form as:

$$\tilde{\rho} = \frac{\omega_{ci}}{\omega_{pi}}(\tilde{\nabla} \cdot \tilde{\mathbf{E}})\,. \tag{B.9}$$

If we take $\omega_{ci}/\omega_{pi} \ll 1$, then $\tilde{\rho} \sim 0$, which means that quasi-neutrality is appropriate to use. The next approximation that will be examined is the net-current free approximation. Ampere's law when recast in dimensionless form can be written as:

$$\tilde{\mathbf{J}} = \frac{\omega_{ci}}{\omega_{pi}}(\tilde{\nabla} \times \tilde{\mathbf{B}} - \frac{\partial \tilde{\mathbf{B}}}{\partial \tau})\,. \tag{B.10}$$

Again, if we take $\omega_{ci}/\omega_{pi} \ll 1$, then we can say that the system is net-current free, or $\tilde{\mathbf{J}} \sim 0$.

The final approximation used is that the electrons are in the ideal MHD limit. If we recast the electron momentum equation into dimensionless form, neglecting electron pressure and resistivity, we obtain:

$$\tilde{\mathbf{E}} + \tilde{\mathbf{v_e}} \times \tilde{\mathbf{B}} = -\frac{m_e}{m_i}\frac{\omega_{pi}}{\omega_{ci}}\frac{\mathrm{D}\tilde{\mathbf{v_e}}}{\mathrm{D}\tau}\,. \tag{B.11}$$

In the Wright paper, he states that ideal MHD is obtained when $|\frac{m_e}{m_i}\frac{\omega_{pi}}{\omega_{ci}}| \ll 1$. In our case, this can possibly be $|\frac{m_e}{m_i}\frac{\omega_{pi}}{\omega_{ci}}| \sim \mathcal{O}(1)$. Though this approximation is not exactly valid, we are not interested in the small scale stable plasma oscillations of zero temperature which do not propagate. If we take a characteristic time scale $\tau \sim \omega_{pi}/\omega_{ci}$ and replace the differential with τ, then the term scales like $m_e/m_p \ll 1$, so over hybrid time scales where the plasma oscillations are averaged over, the ideal MHD approximation is valid.

Now that the assumptions have been validated, we can now solve for the vector

potential $\mathbf{A}$. The vector potential outside of the debris cloud with radius R matched the initial conditions of $\mathbf{B} = B_0\hat{\mathbf{z}}$, or written in terms of the vector potential $\mathbf{A} = \nabla \times \mathbf{B}$, $\mathbf{A}(t = 0) = \frac{rB_0}{2}\hat{\phi}$. This means that only the $\hat{\phi}$ component of the vector potential is non-zero to be able to have continuity of $\mathbf{A}$ at all boundaries. In the magnetostatic limit, with zero net current, we need to solve the differential equation:

$$\nabla \times \mathbf{B} = 0\,. \tag{B.12}$$

If we solve this in terms of the magnetic potential in the Coulomb gauge ($\nabla \cdot \mathbf{A} = 0$), we end up needing to satisfy this homogeneous differential equation in cylindrical coordinates:

$$\frac{\partial^2 A_\phi}{\partial r^2} + \frac{1}{r}\frac{\partial A_\phi}{\partial r} - \frac{A_\phi}{r^2} = 0\,, \tag{B.13}$$

which has a solution of the form:

$$A_\phi(r) = C_1 r + \frac{C_2}{r}\,, \tag{B.14}$$

where C_1 and C_2 are constants that need to be solved for by matching the boundary conditions of:

$$A_\phi(R_c) = 0\,,\ A_\phi(R) = \frac{B_0 R}{2}\,. \tag{B.15}$$

This leads to the solution for the vector potential of:

$$A_\phi(r) = \frac{B_0 r}{2}\frac{1 - (\frac{R_c}{r})^2}{1 - (\frac{R_c}{R})^2}\,. \tag{B.16}$$

We can then compute the magnetic field of:

$$\frac{\mathbf{B}}{B_0} = (1 - (\frac{R_c}{R})^2)^{-1}\hat{\mathbf{z}}\,, \tag{B.17}$$

where is we substitute in our previously found relationship in equation B.7, we end up after a bit of algebra with:

$$\frac{\mathbf{B}}{B_0} = \big[1 + \frac{Z_d}{m_d/m_i}\big(\frac{R_m}{R}\big)^2\big]\hat{\mathbf{z}}\,, \tag{B.18}$$

which can be expressed as:

$$\frac{\Delta B}{B_0} = \frac{Z_d N_d}{\pi n_i R^2}\,, \tag{B.19}$$

where $\Delta B = B_z - B_0$. This means that the magnetic field compression is $\Delta B \propto n_i^{-1}$. We can also find the electric field within the shell by using $\mathbf{E} = -\frac{1}{c}\frac{\partial \mathbf{A}}{\partial t}$, where $R(t) = \mathcal{M}_A v_a t$. This leads to the equation for the electric field:

$$\frac{\mathbf{E}}{B_0} = (\frac{r}{ct})(\frac{Z_d}{m_d/m_i})(\frac{R_m}{R})^2\hat{\phi}\,, \tag{B.20}$$

which can also be expressed as:

$$\frac{\mathbf{E}}{B_0} = \frac{r}{ct}\frac{Z_d N_d}{\pi n_i R^2}\hat{\phi} = \mathcal{M}_A(\frac{\omega_{ci}}{\omega_{pi}})(\frac{r}{R})\frac{Z_d N_d}{\pi n_i R^2}\,. \tag{B.21}$$

The magnitude of the electric field is then $|\mathbf{E}| \propto n_i^{-3/2}$.

We can now extend the Wright model to include a density jump as discussed in Section 3.2. If we now consider the radius R_n, which denotes the radius of a density step up. The azimuthal electric field exists in the shell, denoted by the red region in Figure B.1, but the coupling field only depends on the density of the ambient plasma within the diamagnetic cavity (grey region). This means that if there is a lower density in the (grey) core, and the coupling fields interact with a higher density where the shell overlaps with a higher density region, then higher density region will feel the larger electric and magnetic fields generated by the lower density core. This in turn will couple more relative energy to the ambient ions that exist within the shell than if the ambient plasma density was uniform.

Appendix C

Proof of Concept of a Faraday Rotation Magnetic Field Probe

C.1 Introduction

Exploding laser-produced plasmas into a preformed magnetized plasma can simulate collisionless shocks of cosmic relevance [12] and create highly nonlinear Alfvén waves [19]. Key measurables are the structure (i.e. the magnetic field profile across the shock-ramp and its evolution) and the magnetohydrodynamic turbulence (i.e. the dissipation mechanism). Identifying turbulence in the lower hybrid range requires magnetic field probes with a bandwidth in excess of 1 GHz. Simultaneously, experiments on quasi-parallel shocks and nonlinear shear Alfvén waves require long measurements with durations of tens of microseconds.

Magnetic flux probes (Bdot probes) are widely used to measure magnetic fields in such plasmas [31]. These probes measure the change in magnetic field over time, which severely constrains these experiments; the signal must be integrated, which accumulates

error over time. In experiments on laser-driven magnetic pistons the magnetic field can vary on the order of kG over a time scale of $\sim$ 30 ns, creating very large signals on the order of a hundred volts in Bdot probes for short times[31]. The contrast is then not large enough to resolve slow variations of the field.

Faraday rotation is a well established plasma diagnostic that has been deployed previously in magnetic fusion devices and fast-pinches [56, 57, 58, 59, 60]. These diagnostics employ far-infrared lasers or microwaves to measure the line integrated rotation of the polarization due to the plasma birefringence across the entire width of the device. Faraday rotation has also been applied in small magneto-optical crystals [61] and waveguides [62] for experiments on high-current pinches measuring large magnetic fields of several Tesla.

We have designed a Faraday rotation diagnostic that resolves smaller magnetic fields ($\sim$10-5000 G) and will be applied in basic plasmas that are too tenuous for plasma-induced Faraday rotation but cold enough to allow insertion of probes without damaging them due to excessive heating[63]. Faraday rotation has not been extensively applied in such plasmas. One such Faraday probe has been designed for basic plasmas, however at limited bandwidth [64]. Faraday rotation probes have several advantages over Bdot probes; they are less susceptible to electromagnetic noise (e.g. from the laser), they can be operated at a higher bandwidth ($>$ GHz), and they measure the magnetic field directly.

In this paper we present results from a proof-of-principle experiment on a Faraday rotation probe that has been developed to study rapidly exploding plasmas in a large magnetized plasma. A pulsed magnetic field generator was used to benchmark the performance of the diagnostic. We present a direct comparison of the Faraday rotation data with simultaneous measurements from a magnetic flux probe. The development of the probe will then be discussed as well as the planned usage and potential improvements in the near future.

C.2 Faraday Rotator Probe

Faraday rotator glass (rare-earth doped borosilicate) rotates the incident plane polarized light in the presence of a magnetic field component collinear to the wave-vector of the light. The angle $\Delta\phi$ by which the plane of polarization is rotated is given by: $\Delta\phi = V(\lambda)\int B\cdot \mathrm{d}l$, where V(λ) is the Verdet constant and the integral expression represents the magnetic field integrated along the path of the laser beam through the crystal. The Verdet constant is a wavelength dependent quantity which quantifies the amount of rotation a linearly polarized beam of light undergoes for a given magnetic field and length. The length of the crystal is $L = 6$ mm and the width of the crystal and holder is ~ 8 mm, which is smaller than the ion Larmor radius ($r_L \sim 1$ cm) of the plasma in the LAPD, so perturbation of the plasma should be minimal. We used terbium, dysprosium, and europium doped borosilicate glass due to its large Verdet constant. In this experiment we measured a Verdet constant of V $\sim$ -650 rad/T·m at $\lambda = 532$ nm, by comparing the measured $\Delta\phi$ to the calculated magnetic field at the center of a coil. A magnetic field strength of B = 50 G directed along the axis of the laser beam will then rotate the plane of polarization by $\Delta\phi = -1.1°$.

Figure C.1 shows the experimental setup. The main elements of the apparatus are the light source, which is a frequency-doubled (532 nm) 5 mW Nd:YAG laser and a Glan-Thompson polarizer with an extinction ratio of $\epsilon \sim 10^{-5}$. The linearly polarized light is passed through the Faraday rotator glass before the beam is split in two using a polarization insensitive beam splitter(PIBS). The polarization of the two beams is analyzed using two Glan-Thompson prisms oriented at angles $\pm\chi$, where χ is the half shadow angle. Like earlier work [65, 66], the current setup uses $\chi = \pm 45°$ to maximize the signal on the detectors. The intensity in each beam is then measured using biased silicon photodiodes (Thorlabs DET10A) connected to an 8 bit oscilloscope through fast (x100 gain) operational amplifiers. The photodiodes are operated at 50 Ω impedance to maximize the time response ($\sim$ 1 ns rise time). The custom built amplifiers have a bandwidth of 150

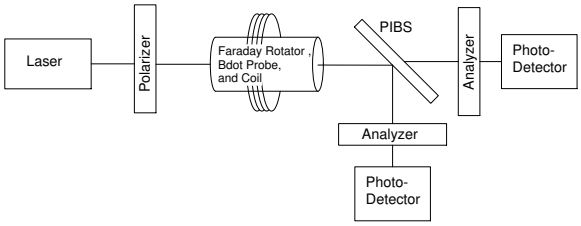

Figure C.1: Shows a diagram of the the experimental setup.

MHz, and currently limit the temporal response of the system to $\sim$ 7 ns.

To benchmark the diagnostic an oscillating magnetic test-field of up to 100 G was created by a pulsed coil, with the crystal positioned in its center. A magnetic flux probe adjacent to the magneto-optic crystal provided simultaneous measurements of dB/dt, while a fast current-transformer was used to monitor the current in the coil. The accuracy of the measurement was limited by the spatial positioning of the probes relative to the center of the coil. The Faraday and Bdot probes could not be colocated exactly at the center of the coil. Using a position difference of $\sim$ 5 mm, the variation of the magnetic field between the devices and the nominal magnetic field is $\sim$10%. All waveforms were recorded on an 8-bit oscilloscope sampling at 2.5 GSamples/s. These three measurements are compared in the experimental results, which are presented later in this section.

The intensity of the laser beam transmitted through the analyzer is given by $I = I_0(\sin^2(\chi + \Delta\phi) + \mathcal{O}(\epsilon))$, where $\Delta\phi$ is the rotation angle from the initial polarization, χ is the angle of the analyzing polarizer relative to the initial polarization of the laser beam, and ϵ is the extinction ratio of the polarizers.

It is usually desirable to determine the rotation angle $\Delta\phi$ from a measurement which does not depend on the initial intensity I_0 of the light. Then fluctuations in the output intensity of the light source, as well as the spectral throughput of the optical system and the sensitivity of the detector, will not affect the measurement of the rotation angle. This can be accomplished by comparing the signals of two analyzers and photo-

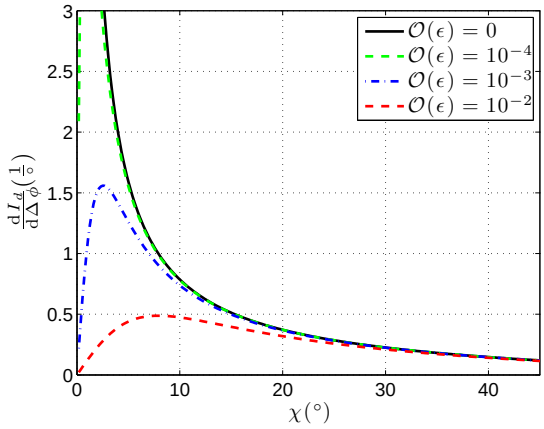

Figure C.2: Contrast as a function of half-shadow angle χ, at $\Delta\phi = 0$ for various extinction ratios.

detectors, with each polarizer oriented at angles $\pm\chi$. This so called half-shadow principle has been used numerous times in the past with half-shadow angle of χ=45°[65, 66]. The normalized intensity I_d is then given by:

$$I_d = \frac{I_1 - I_2}{I_1 + I_2} = \frac{\sin(2\chi)\sin(2\Delta\phi) + \mathcal{O}(\epsilon)}{1 - \cos(2\chi)\cos(2\Delta\phi) + \mathcal{O}(\epsilon)}\,. \tag{C.1}$$

The polarization angle $\Delta\phi$ can then be found by solving for the roots of Eq. C.1 for a measured value of I_d, where I_1 and I_2 are the intensity measurements from the two photo-detectors. If high gain photo-detectors (e.g. photo-multiplier tubes) are used, the half shadow angle can be reduced from 45° to allow for a higher contrast, which is defined to be the relative change in intensity due to a change in polarization angle. The contrast can be shown to be:

$$\frac{\mathrm{d}I_d}{\mathrm{d}\Delta\phi} \simeq \frac{2\sin(2\chi)\cos(2\Delta\phi)}{1 - \cos(2\chi)\cos(2\Delta\phi) + \mathcal{O}(\epsilon)} \tag{C.2}$$

for small $\Delta\phi$. Figure C.2 shows how the contrast increases as χ decreases for $\Delta\phi \ll 1$ rad. While the contrast increases infinitely for an ideal system ($\epsilon = 0$), the contrast peaks at an angle $\chi_{peak} < 45°$ that depends on ϵ for systems with finite extinction ratio. The ideal half-shadow angle is thus between χ_{peak} and 45°, depending on the available laser-power and detector sensitivity.

The Glan-Thompson polarizers used in the present setup have an excellent extinction ratio ($\epsilon < 10^{-5}$), but there are other factors that contribute to coupling power between the dominant linear polarization and the orthogonal polarization. For example, the smoothness of the optics has an effect on the polarization of the light, so the system as a whole can have a higher extinction ratio than that of the polarizers[67]. In general, when χ is decreased there is a corresponding decrease in overall light falling onto the detector, so high gain photo-detectors and a high powered laser are needed to compensate for the decrease in light. If χ were set to 10° instead of 45°, a given rotation angle would yield a factor of five higher I_d for a system with an extinction ratio of $\mathcal{O}(\epsilon) \sim 10^{-3}$, which would result in a higher angular resolution. In our experiment the photodiodes output a low signal when operated at low impedance, so an angle of $\chi = 45°$ was chosen to maximize the dynamic range of the signal output from the photodiodes.

The diagnostic was benchmarked with a pulsed magnetic field coil that generates a well-known and quasi-homogeneous magnetic field of magnitude and frequency comparable to those expected in a laser-plasma experiment. Figure C.3 shows a comparison of the Faraday rotation data with the Bdot signal and the magnetic field from the current transformer, which was calculated using the equation for an ideal current loop. Figure C.3 shows that the Faraday probe data matches well with the calculated magnetic field. Since the signal strength in the present setup was limited by the sensitivity of the photodiodes, the rotation signal is quite noisy and on the order of ±5 G. From the Bdot probe data, the magnetic field was calculated based on previously measured calibration data (probe area and frequency response[31]). The raw Bdot data was shifted to have zero mean when no magnetic field was present so that the noise in the signal would not integrate to a linearly increasing signal. While all three measurements agree well during the first few microseconds, the Bdot data drifts by more than 15 G at later times due to integration error, even though the amplitude of the Bdot signal was several orders of magnitude larger (and thus the noise several orders of magnitude smaller) than the Faraday probe data.

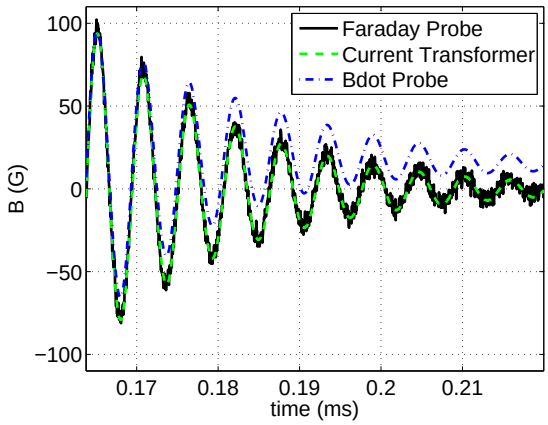

Figure C.3: Faraday (solid line) and Bdot (dot-dashed line) probe measurements compared to the calculated magnetic field from current transformer (dashed line).

C.3 Conclusion

In summary, we have presented a direct comparison of simultaneous Faraday probe and magnetic flux-probe (Bdot) measurements in the center of a pulsed magnetic test-coil. It was shown that the Faraday probe could measure a rapidly varying signal with a resolution of $\sim$5 G, which is superior to the Bdot probe at late times. In the future the resolution of the system will be increased by several orders of magnitude by using more sensitive detectors (photo-multiplier tubes) in combination with a reduced half-shadow angle of a few degrees, which will significantly increase the contrast and allow us to resolve much smaller rotation angles (below 0.01°), corresponding to magnetic fields below 1 G, with a bandwidth in excess of 1 GHz. The sensitivity could be further increased by employing a two-pass scheme, which will double the rotation angle since Faraday rotation is non-reciprocal. In future implementations of the diagnostic we plan to measure multiple dimensions of the magnetic field by passing separate laser beams through different faces of a cube of Faraday rotator glass. We also plan to reduce the physical size of the probe to improve spatial and temporal resolution. The diagnostic will be used to study laser-driven collisionless shocks in the Large Plasma Device[12].

Bibliography

[1] V. P. Bashurin, A. I. Golubev, and V. A. Terekhin *J. Appl. Mech. Tech. Phys.*, vol. 24, p. 614, 1983.

[2] C. Niemann, W. Gekelman, C. G. Constantin, E. T. Everson, D. B. Schaeffer, A. S. Bondarenko, S. E. Clark, D. Winske, S. Vincena, B. V. Compernolle, and P. Pribyl *Geophys. Res. Lett.*, vol. 41, pp. 7413–7418, 2014.

[3] M. J. Martin, J. Bonde, W. Gekelman, and P. Pribyl *Rev. Sci. Instrum.*, vol. 86, p. 053507, 2015.

[4] D. S. Spicer, R. W. Clark, and S. P. Maran *Astrophys. J.*, vol. 356, pp. 549–571, 1990.

[5] P. Dyal *J. Geophys. Res.*, vol. 111, p. A12211, 2006.

[6] N. Omidi and D. Winske *J. Geophys. Res.*, vol. 92, no. A12, pp. 13409–13426, 1987.

[7] C. T. Russell and E. W. Greenstadt *Space Science Reviews*, vol. 23, pp. 3–37, 1979.

[8] C. P. Escoubet, M. Fehringer, and M. Goldstein *Annales Geophysicae*, vol. 19, pp. 1197–1200, 2001.

[9] M. Keilhacker, M. Kornherr, and K.-H. Steuer *Z. Physik*, vol. 223, pp. 385–396, 1969.

[10] E. C. Merritt, A. L. Moser, S. C. Hsu, C. S. Adams, J. P. Dunn, A. M. Holgado, and M. A. Gilmore *Phys. Plasmas*, vol. 21, p. 055703, 2014.

[11] H.-S. Park, D. D. Ryutov, J. S. Ross, N. L. Kugland, S. H. Glenzer, C. Plechaty, S. M. Pollaine, B. A. Remington, A. Spitkovsky, L. Gargate, G. Gregori, A. Bell, C. Murphy, Y. Sakawa, Y. Kuramitsu, T. Morita, H. Takabe, D. H. Froula, G. Fiksel, F. Miniati, M. Koenig, A. Ravasio, A. Pelka, E. Liang, N. Woolsey, C. C. Kuranz, R. P. Drake, and M. J. Grosskopf *High Energy Density Physics*, vol. 8, pp. 38–45, 2012.

[12] C. Niemann, C. G. Constantin, D. B. Schaeffer, A. Tauschwitz, T. Weiland, Z. Lucky, W. Gekelman, E. T. Everson, and D. Winske *Journal of Instrumentation*, vol. 7, p. P03010, 2012.

[13] W. Gekelman, H. Pfister, Z. Lucky, J. Bamber, D. Leneman, and J. Maggs *Rev. Sci. Instrum.*, vol. 62, p. 2875, 1991.

[14] C. Niemann, W. Gekelman, C. G. Constantin, E. T. Everson, D. B. Schaeffer, S. E. Clark, D. Winske, A. B. Zylstra, P. Probyl, S. K. P. Tripathi, D. Larson, S. H. Glenzer, and A. S. Bondarenko *Phys. Plasmas*, vol. 20, p. 012108, 2013.

[15] B. Ripin, E. McLean, C. Manka, C. Pawley, J. Stamper, T. Peyser, A. Mostovych, J. Grun, A. Assam, and J. Huba *Phys. Rev. Lett*, vol. 59, p. 2299, 1987.

[16] J. E. Borovsky, M. B. Pongatz, R. A. Roussel-Dupre, and T. H. Tan *Astrophys. J.*, vol. 280, p. 802, 1984.

[17] Y. P. Zakharov *IEEE Trans. Plasma Sci.*, vol. 31, p. 1243, 2003.

[18] R. P. Drake *Phys. Plasmas*, vol. 7, p. 4690, 2000.

[19] C. Constantin, W. Gekelman, P. Pribyl, E. Everson, D. Schaeffer, N. Kugland, R. Presura, S. Neff, C. Plechaty, S. Vincena, A. Collette, S. Tripathi, M. V. Muniz, and C. Niemann *Astrophys. Space Sci.*, vol. 322, p. 155, 2009.

[20] A. Collette and W. Gekelman *Phys. Rev. Lett.*, vol. 105, p. 195003, 2010.

[21] V. A. Thomas and S. H. Brecht *Phys. Fluids*, vol. 29, p. 2444, 1986.

[22] D. Winske and S. Gary *J. Geophys. Res.*, vol. 112, p. A10303, 2007.

[23] S. H. Brecht, D. W. Hewett, and D. J. Larson *Geophys. Res. Lett.*, vol. 36, p. 15, 2009.

[24] D. W. Hewett, S. H. Brecht, and D. J. Larson *J. Geophys. Res.*, vol. 116, p. A11310, 2011.

[25] M. M. Leroy, D. Winske, C. C. Goodrich, C. S. Wu, and K. Papadopoulos *J. Geophys. Res.*, vol. 87, p. 5081, 1982.

[26] B. Lembege, J. Giacalone, M. Scholer, T. Hada, M. Hoshino, V. Krasnoselskikh, H. Kucharek, P. Savioni, and T. Terasawa *Space Sci. Rev.*, vol. 110, p. 161, 2004.

[27] A. G. Sgro and C. W. Nielson *Phys. Fluids*, vol. 19, p. 126, 1976.

[28] N. T. Gladd and S. H. Brecht *IEEE Trans. Plasma Sci.*, vol. 20, p. 678, 1992.

[29] X. Blanco-Cano, N. Omidi, and C. T. Russell *J. Geophys. Res.*, vol. 108, p. 1216, 2003.

[30] J. Towns, T. Cockerill, M. Dahan, I. Foster, K. Gaither, A. Grimshaw, V. Hazlewood, S. Lathrop, D. Lifka, G. D. Peterson, R. Roskies, J. R. Scott, and N. Wilkins-Diehr *Comput. Sci. Eng.*, vol. 16, no. 5, pp. 62–74, 2014.

[31] E. T. Everson, P. Pribyl, C. G. Constantin, A. Zylstra, D. Schaeffer, N. L. Kugland, and C. Niemann *Rev. Sci. Instrum.*, vol. 80, p. 113505, 2009.

[32] D. Winske and K. B. Quest *J. Geophys. Res.*, vol. 93, no. A9, p. 9681, 1988.

[33] N. L. Kugland, D. D. Ryutov, P.-Y. Chang, R. P. Drake, G. Fiksel, D. H. Froula, S. H. Glenzer, G. Gregori, M. Grosskopf, M. Koenig, Y. Kuramitsu, C. Kuranz, M. C. Levy, E. Liang, J. Meinecke, F. Miniati, T. Morita, A. Pelka, C. Plechaty, R. Presura,

A. Ravasio, B. A. Remington, B. Reville, J. S. Ross, Y. Sakawa, A. Spitkovsky, H. Takabe, and H.-S. Park *Nature Physics*, vol. 8, p. 809, 2012.

[34] D. Burgess, "Collisionless shocks," in *Introduction to Space Physics* (M. G. Kivelson and C. T. Russell, eds.), ch. 5, pp. 129–163, Cambridge University Press, 1995.

[35] G. Dimonte and L. Wiley *Phys. Rev. Lett.*, vol. 67, p. 1755, 1991.

[36] A. I. Golubev, A. A. Solov'ev, and V. A. Terekhin *J. Appl. Mech. Tech. Phys.*, vol. 19, p. 602, 1979.

[37] R. A. Treumann *Astron. Astrophys. Rev.*, vol. 17, pp. 409–535, 2009.

[38] B. Lembege and F. Simonet *Phys. Plasmas*, vol. 8, p. 3967, 2001.

[39] D. A. Tidman and N. A. Krall, *Shock Waves in Collisionless Plasmas*. Wiley-Interscience, New York, 1971.

[40] D. B. Schaeffer, E. T. Everson, D. Winske, C. G. Constantin, A. S. Bondarenko, L. A. Morton, K. A. Flippo, D. S. Montgomery, S. A. Gaillard, and C. Niemann *Phys. Plasmas*, vol. 19, p. 070702, 2012.

[41] G. Paschmann, N. Sckopke, I. Papamastorakis, J. R. Asbridge, S. J. Bame, and J. T. Gosling *J. Geophys. Res.*, vol. 86, p. 4355, 1981.

[42] M. H. Key, W. T. Toner, T. J. Goldsach, J. D. Kilhenny, S. A. Veats, P. F. Cunningham, and C. L. S. Lewis *Phys. Fluids*, vol. 26, no. 7, p. 2011, 1983.

[43] B. Meyer and G. Thiell *Phys. Fluids*, vol. 27, no. 1, p. 302, 1984.

[44] A. S. Bondarenko, D. B. Schaeffer, E. T. Everson, C. G. Constantin, S. E. Clark, and C. Niemann *Rev. Sci. Instrum.*, vol. 83, p. 10E515, 2012.

[45] B. C. Boland, F. E. Irons, and R. W. P. McWhirter *J. Phys. B*, vol. 1, no. 6, p. 1180, 1968.

[46] T. P. Wright *Phys. Fluids*, vol. 14, no. 9, p. 1905, 1971.

[47] S. E. Clark, D. Winske, D. B. Schaeffer, E. T. Everson, A. S. Bondarenko, C. G. Constantin, and C. Niemann *Phys. Plasmas*, vol. 20, p. 082129, 2013.

[48] D. B. Schaeffer, *Generation of Quasi-Perpendicular Collisionless Shocks by a Laser-Driven Magnetic Piston.* PhD thesis, University of California, Los Angeles, 2014.

[49] A. S. Bondarenko, D. B. Schaeffer, E. T. Everson, S. E. Clark, C. G. Constantin, and C. Niemann *Phys. Plasmas*, vol. 21, p. 122112, 2014.

[50] T. A. Peyser, C. K. Manka, B. H. Ripin, and G. Ganguli *Phys. Fluids B*, vol. 4, p. 2448, 1992.

[51] C. L. S. Lewis, P. F. Cunningham, L. Pina, A. K. Roy, and J. M. Ward *J. Phys. D: Appl. Phys.*, vol. 15, pp. 69–75, 1982.

[52] D. B. Schaeffer, A. S. Bondarenko, E. T. Everson, S. E. Clark, C. G. Constantin, and C. Niemann *J. Appl. Phys.*, vol. 120, p. 043301, 2016.

[53] J. Bonde, S. Vincena, and W. Gekelman *Phys. Rev. E*, vol. 92, p. 051102(R), 2015.

[54] D. W. Forslund *Space Sci. Rev.*, vol. 42, pp. 3–16, 1985.

[55] D. S. Harned *J. Comp. Phys.*, vol. 47, pp. 452–462, 1982.

[56] H. Soltwisch *Rev. Sci. Instrum.*, vol. 57, no. 8, p. 1939, 1986.

[57] B. W. Rice *Rev. Sci. Instrum.*, vol. 63, no. 10, p. 5002, 1992.

[58] W. Kunz *Nucl. Fus.*, vol. 18, no. 12, p. 1729, 1978.

[59] F. C. Jobes and D. K. Mansfield *Rev. Sci. Instrum.*, vol. 63, no. 10, p. 5154, 1992.

[60] C. H. Ma, D. P. Hutchinson, and K. L. V. Sluis *Appl. Phys. Lett.*, vol. 34, no. 3, p. 218, 1979.

[61] T. Intrator, B. Marshall, D. Clark, T. McCuistan, B. Anderson, B. Broste, K. Forman, and M. Taccetti *Rev. Sci. Instrum.*, vol. 73, p. 141, 2002.

[62] W. Syed, D. A. Hammer, and M. Lipson *Optics Letters*, vol. 73, no. 7, p. 1009, 2009.

[63] W. Gekelman, S. Vincena, B. V. Compernolle, G. J. Morales, J. E. Maggs, P. Pribyl, and T. A. Carter *Phys. Plasmas*, vol. 18, p. 055501, 2011.

[64] W. S. Przybysz, J. Ellis, S. C. Thakur, A. Hansen, and R. A. Hardin *Rev. Sci. Instrum.*, vol. 80, p. 103502, 2009.

[65] I. S. Falconer and S. A. Ramsden *J. Appl. Phys.*, vol. 39, p. 3449, 1968.

[66] R. F. Gribble, E. M. Little, R. L. Morse, and W. E. Quinn *Phys. Fluids*, vol. 11, p. 1221, 1968.

[67] C. A. Balanis, *Advanced Engineering Electromagnetics*. John Wiley & Sons, Inc., 1989.